Stony Brook University

To Study Crystal Cracking and Melt Inclusion during Laser Crystal Growth by Czochralski Method

A Dissertation Presented

by

Haisheng Fang

to

The Graduate School

in Partial Fulfillment of the

Requirements

for the Degree of

Doctor of Philosophy

in

Mechanical Engineering

Stony Brook University

August 2008

Stony Brook University

The Graduate School

Haisheng Fang

We, the dissertation committee for the above candidate for the
Doctor of Philosophy degree,
hereby recommend acceptance of the dissertation.

Professor Hui Zhang, Advisor
Department of Mechanical Engineering

Professor Lili Zheng, Chair
Department of Mechanical Engineering

Professor Chad S. Korach, Member
Department of Mechanical Engineering

Professor Xiaolin Li, Outside Member
Department of Applied Mathematics and Statistics

This dissertation is accepted by the Graduate School

Lawrence Martin
Dean of the Graduate School

Abstract of the Dissertation

To Study Crystal Cracking and Melt Inclusion during Laser Crystal Growth by Czochralski Method

By

Haisheng Fang

Doctor of Philosophy

In

Mechanical Engineering

Stony Brook University

2008

Synthesis and processing of novel materials have attracted much attention for the past thirty years due to the development of semiconductor, aviation, laser operation, etc. Many advanced materials display a number of exceptional properties. For example, Yb:S-FAP [Yb^{3+}:$Sr_5(PO_4)_3F$] crystal has emerged for laser applications due to its many attractive properties, such as the relaxed diode brightness requirements, long lifetime of 1.1ms, and a suitable gain cross-section for ns pulse extraction.

The objective of this work is to study and optimize the growth process of Yb:S-FAP crystal, and to obtain large diameter crystals with high optical qualities. Two important issues of cracking and melt inclusion that significantly affect optical qualities of crystals have been studied. To suppress cracking during cool down, the critical radial temperature difference, above which the crystal cracks, has been determined by benchmarking the simulation results against experimental observations. Based on this comparison, an optimal three-stage ramp-down profile was implemented and produced crack-free Yb:S-FAP crystals. Efforts are further conducted to reduce cooling time by improving growth furnace or redesigning the cooling process. To control melt inclusion, two types of mechanisms possibly responsible for inclusion are presented. Both of them show the prerequisite of melt inclusion is solute pileup. Solute pileup could be determined by flow patterns in the melt. Consequently, a technique of submerged baffle/heater is introduced

to control melt inclusion. An optimized design of submerged heater is determined through numerical simulation.

In order to conveniently model free surface flow in the melt, a meshless method called Smoothed Particle Hydrodynamics (SPH) is introduced. The traditional SPH method was improved by a new pressure-correction equation that is proposed to efficiently transport the local pressure to the neighboring area during the impact of incompressible fluid and to reduce the disorder of particle distribution. The new treatment of surface tension and solidification is also proposed to manipulate the SPH particles near free surface and solidification interface. Using the improved SPH method, droplet impact, spreading, and solidification are simulated. These simulations have proved that SPH is a powerful tool to simulate free surface problems, and is a highly potential method to predict distribution of melt inclusion in the grown crystals.

To my family

Table of Contents

List of Symbols

A	area, m^2
$\boldsymbol{A}$	magnetic vector potential, Wb/m
$\boldsymbol{A_0}$	amplitude of magnetic vector potential ($\boldsymbol{A} = \boldsymbol{A}_0 e^{i\omega t}$), Wb/m
Bi	Biot number
α_R	Rosseland mean absorption coefficient
c	specific heat per unit volume, J/(Kg K), or sound speed, m/s
c_p	heat capacity, J/(Kg K)
D	solute diffusion coefficient, or crucible diameter, m
	parameter in Lennard-Jones form
d	spatial dimension
F	view factor
G	temperature gradient, K/m
Gr	Gr number
$\boldsymbol{g}$	gravitational acceleration vector
H	the latent heat, J/kg, or depth of submerged heater, m
	artificial heat, J/(kg s)
H_1	height of the melt
h	effective heat transfer coefficient, W/(m^2 K)
	smoothing length, m
J	Bessel function
$\boldsymbol{J_0}$	amplitude of the AC current
k	thermal conductivity, W/(m K)
m	mass, kg
n	refractive index
$\boldsymbol{n}$	the unit vector of normal direction at the interface
N	number of turns, or the total number of particles
P	power of the RF induction heater, W
	Pressure, kg/(m s^2)
Pr	Prandtl number
q	heat source, W/m^3
R	crystal radius, m
Re	Reynolds number
r	radial position, m
Sc	Sc number

T	temperature, K
T_f	average system temperature, K
T_∞	environment temperature, K
T_{mp}	melting point temperature
T_w	the highest crucible temperature
t	time, s
$\boldsymbol{u}$	velocity vector, m/s
u	internal energy, J/kg
u_p	pulling rate, m/s
V	crystal growth rate, m/s
$\vec{v}$	particle velocity vector, m/s
W	smoothing function, m^{-3}
w	crystal rotation rate, rad/s
x	particle position, m

Greek symbols

α	thermal diffusivity, m/s
α_d	spatial coefficient
β	thermal expansion coefficient, K^{-1}
β_m	positive roots of Bessel equation
ρ_c	electrical resistivity of coil
ρ	density, kg/m^3
κ	a scale factor
ε_b	critical strain
ε	emissivity
δ	boundary layer thickness, m
σ	Stefan-Boltzmann constant
σ_c	electrical conductivity
μ	viscosity, kg/(m s)
μ_m	constant magnetic permeability
v	Dynamical viscosity, m^2/s
ω	angular frequency of applied AC current
τ	viscous stress tensor, kg/m s^2
Δ	difference of two values
∇	gradient

Subscript

c	coil, or crucible
f	furnace
eff	effective value
i, j	particle index, or parts in furnace

L	liquid
P	particle
R	values along radial direction
r	radiation value, or radial position
S	solid
sur	surrounding environment value
0	reference value

List of Figures

List of Tables

Chapter 1 Introduction

1.1 Yb:S-FAP Crystal

The importance of single crystals of oxides for technological applications was recognized after the discovery of pulsed laser action of ruby in 1960[1] and both pulsed and continuous wave laser emission in Neodymium-doped Calcium Tungstate in the following two years [2]. Since then, oxides have been widely used in lasers, substrates, shock-proof, transparent windows, small-diameter crystal fibers, and have found new applications in the ferroelectric, pyroelectric, piezoelectric, acoustic, magnetic, and opto-magnetic devices. The widespread use of oxide crystals is attributed from their special optical, fluorescent, electrical, and mechanical properties. As a kind of oxide material, Yb:S-FAP crystals have been used for the gain medium of high power, diode-pumped laser system. Yb:S-FAP crystals have been extensively studied by Deloach et al. [3] for a variety of laser applications. Because of their many attractive properties shown in Table 1 [3-6], Yb:S-FAP crystals are well suited for diode pumping in moderate thermal load applications. The large emission and absorption cross sections for nsec pulse extraction shown in the Table 1, makes diode pumping more cost-feasible for larger laser systems due to the reduced requirement on the diode brightness and allows for efficient extraction at moderate fluence. The long fluorescence lifetime of 1.14ms allows for greater energy storage in the material with reduced requirement for diode packages. The mercury laser, at Lawrence Livermore National Laboratory (LLNL), is the most prominent system (Figure 1) [7] which requires a minimum of 14 slabs with dimensions of 4×6×0.75cm in thickness. Figure 2 shows a schematic of the multi-pass side-pumped Yb:S-FAP amplifier designed by Q-Peak, Inc[8]. A three-level continuous-wave Yb:S-FAP laser operating at 985 nm and pumped by a Ti:Sapphire laser has been reported by Laboratoire Charles Fabry del'Institut d'Optique in France[9]. Yb:S-FAP is also being utilized in a diode-pumped high-energy regenerative amplifier targeted as a 1J, 50-100 Hz, and ≤ 1ps[10]. Recently, a diode-pumped, chirped-pulse Yb:S-FAP regenerative amplifier was presented by Shinji Ito et al.[11], which was developed as a first amplifier in an all-solid-state Yb:S-FAP laser system for laser-Compton X-ray generation.

Due to these important applications, it is desirable to grow large Yb:S-FAP crystals with high optical quality. A growth process based on Czochralski method has been developed to routinely produce high quality 3.5cm diameter crystals, and a

process for producing 7.0cm diameter crystals has also been developed due to our efforts. A detail discussion of this process will be presented in the following sections.

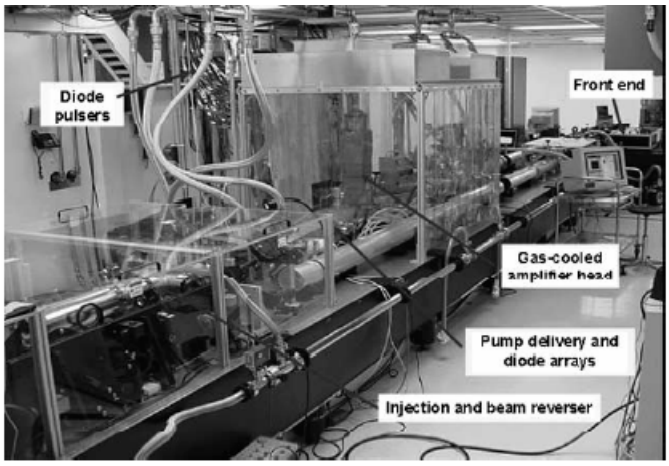

Figure 1 The mercury laser architecture in LLNL

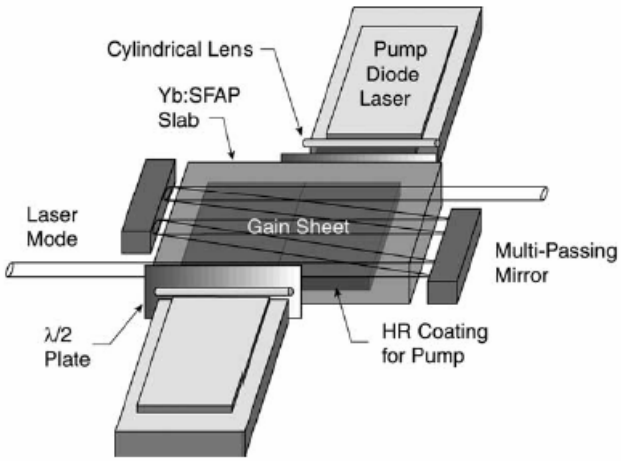

Figure 2 Schematic of multi-pass side-pumped Yb:S-FAP amplifier designed by Q-Peak, Inc

Table 1 Comparison of Yb-doped materials for the fundamental properties

	Yb:S-FAP	Yb:YAG	Yb:SiO_2	Yb:KGW
Pump wavelength (nm)	900	941	915	981
Laser wavelength (nm)	1047	1030	1039-1062	1025-1045
Fluorescence lifetime (ms)	1.14	0.95	0.94	0.6
Absorption cross section(10^{-20} cm^2)	9.0	0.7	0.4	12
Emission cross section (10^{-20} cm^2)	6.0	1.9	0.4	2.8
Saturation fluence (J/cm^2)	3.1	9.6	44	6.9
Pump saturation intensity (kW/cm^2)	2.9	28	47	12
Spectral bandwidth (nm)	5	10	200	20
Thermal conductivity (W/mK)	2	10	0.6	2.6-2.8
Laser geometry	Slabs/rods	Thin disk/rods	Fibers	Thin disk/rods

1.2 Yb:S-FAP Crystal Growth

1.2.1 History of Yb:S-FAP Crystal Growth

The development of the apatite crystal and the strontium fluorophosphates derivative has been ongoing for the last thirty years. Initial research was focused on characterizing the calcium fluorapatite for neodymium lasers[12]. More recently, Yb^{3+}-doped materials have attracted a great interest in relation to the development of diode-pumped all-solid-state lasers. There are three major superiorities of Yb^{3+}-doped materials. The small quantum defects result in lower thermal loading and reduce thermal problems; the long fluorescence lifetime (1-2ms) offers the advantages of greater energy storage in a gain medium in high-energy ultra-short amplification; and the broad gain bandwidth make it possible to generate and amplify ultra-short laser pulses. The wide applications of Yb^{3+}-doped fluorapatite($Ca_5(PO_4)_3F$, or FAP) as the pump source in laser system are due to these advantages[4]. By completely replacing the calcium II sites in FAP with strontium, the analogue S-FAP ($Sr_5(PO_4)_3F$) is realized and serves as a suitable host for the Yb^{3+} ion.

High optical quality crystals of Yb:S-FAP are grown using Czochralski method in a high temperature oxide-type furnace. The research conducted in Lawrence Livermore National Laboratory provided excellent experience on growth of high quality Yb:S-FAP crystals [7, 13, 14]. They developed a growth process for crystals with a diameter of 3.5cm to simultaneously eliminate or diminish growth issues, such as cloudiness, bubble core defects, anomalous absorption, low-angle grain boundaries, cracking, and crystal inclusions.

1.2.2 Czochralski Method for Yb:S-FAP Crystal Growth

The Czochralski method [15] is a method of crystal growth used to obtain single crystals of semiconductors (e.g. silicon, germanium and gallium arsenide), metals (e.g. palladium, platinum, silver, gold), salts and some man-made gemstones. It has virtually dominated the entire production of single crystals for the microelectronics industry [16, 17]. The popularity of this method comes from its ability to meet stringent requirements for purity, doping, electrical and mechanical properties, and crystallographic perfection. It is also popular in growing single crystals of oxides (optical crystals). A comprehensive list of oxides grown by the Cz method can be found in Pressley [18], and Cockayne [19]. Hurle and cockayne [17] have presented an excellent review of the conditions for Cz growth of oxides, quality of the oxide crystals grown so far, and major difficulties in growing these materials. Recently, many researchers spent their efforts on studying new optical crystals grown by Cz method [10, 20-26].

Fundamentally, the Cz process consists of freezing material from a molten pool contained in a crucible, onto the end of a single-crystal seed of the same material. A schematic of the conventional Cz process is given in Figure 3 illustrating the various steps of crucible charging, seeding, crowning, growing, tailing and crystal removal. Figure 4 presents a growing single crystal by the Cz method.

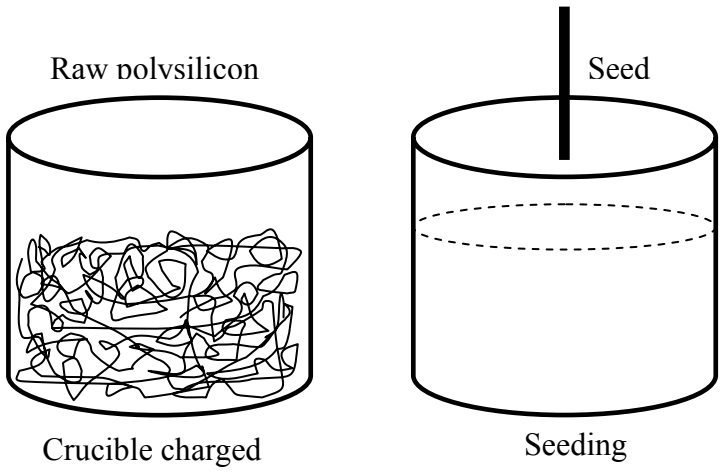

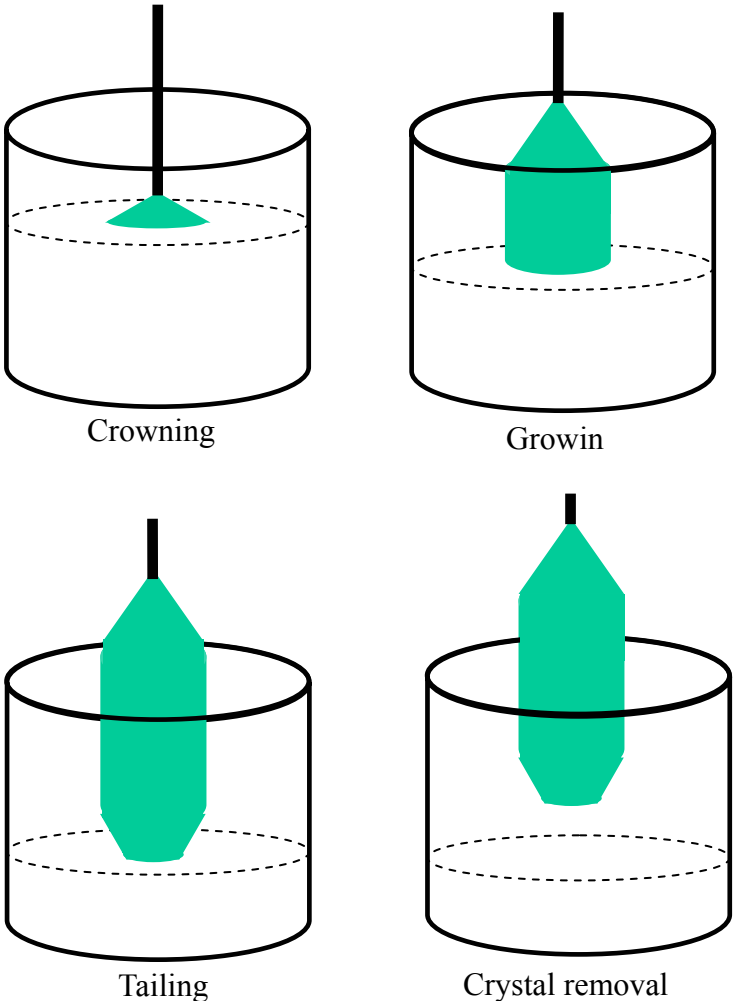

Figure 3 Various steps in a conventional Cz process

Figure 4 A growing single crystal by the Cz method (originated from ICMCB-CNRS)

1.2.3 Defects in Czochralski-grown Crystals

Generally, the Cz-grown optical crystals suffer a few defects which severely affect their use in laser application. Defects in oxide crystals can be categorized into two groups: stress and chemical related defects. It is believed that thermal conditions during growth are the major factors behind these chemical and stress-related defects.

There exist six main defects in the grown optical crystals including cloudiness [6, 27, 28], bubble core [27], anomalous absorption [29], grain boundaries [12], cracking and scattering inclusions. Some of the defects are shown in Figure 5. Cloudiness has been attributed to second phase precipitation on line defects in the crystal lattice. The precipitate could be caused by slight incongruent melting in addition to significant evaporation of some volatile components from the melt surface at the melting temperature. Cloudiness can be annealed away by suspending the boule over the melt directly following growth. The anomalous absorption is caused by to the dopant ion (Yb^{3+} in Yb:S-FAP crystals) on a second site in the crystal lattice, based on excitation and emission spectra. Grain boundaries appear as slight shifts in the refractive index or waves running through the crystal in sheets orientated perpendicular to the *c*-axis. It has been eliminated by growing "seed extensions" and choosing a small cone angle to maintain a stable growth interface. During crystal cooling, cracking happens especially in the large diameter crystals. Thermal stresses induced in the cooling process have been considered as the major cause, which causes crystal to deform elastically up to certain limit and then deform plastically with dislocation formation. However, there are a large number of materials which cannot be deformed plastically. For these if the induced stress or strain exceeds to a certain critical limit, they will crack [30]

Cloudiness

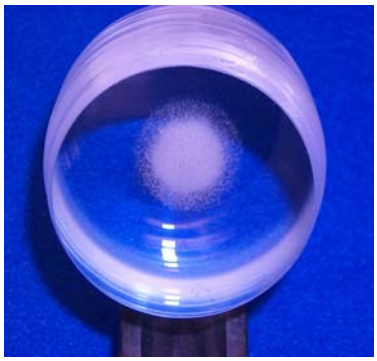

Bubble core

Cracking

Figure 5 Several defects in the Yb:S-FAP crystals(originated from LLNL)

The mechanism of melt inclusion in growing single crystals, however, is not very clear. Components and phases of melt inclusion are hard to determine which make the understanding of melt inclusion mechanism very difficult. Fortunately, people have long experience on the research of solidification phenomena which provides us useful information for the effects of the solute on solidification. The understanding of the mechanism of melt inclusion for optical laser crystals becomes a object of this thesis.

1.3 Technological Challenges

1.3.1 Transport Phenomena in Czochralski Crystal Growth Process

The growth process of optical crystals is highly dominated by all kind of transport phenomena. Figure 6 shows briefly a schematic of heat transfer in a Cz system. Since buoyancy and surface tension forces are strong, they produce convective rolls of complex nature that may be oscillatory, turbulent, or both in the case of large melt volumes. Crystal rotation or crucible rotation in some cases superimposes forced convection in the melt. The convective flow is combined with temperature fields both of which depend on each other as well as on the melt level which varies by time.

The recirculating flow in the melt is caused by a combination of several basic modes of convection [17, 31-33]. Complex thermal boundaries, such as side wall heating, free surface cooling by radiation, phase transformation in the S/L interface,

and buoyancy; The variation in surface tension causes the Marangoni convection; Crystal rotation or crucible rotation in some cases generates forced convection near the interface region; Also crystal pulling the melt height dropping also cause weaker forced convection. During the process of crowning and tailing, convection due to crystal pulling may be appreciable, but in other cases it is very small and is therefore neglected in theoretical studies and simulation experiments. Convective transport in the melt is closely coupled with radiation in the system. For example, the melt surface for Yb:S-FAP crystal growth is maintained at a temperature about 1786℃, while the walls of the growth furnace are cooled by recirculating water at around room temperature. Also internal radiation of optical crystal becomes complex due to the length change of the crystal, and it is significant for the formation of the interface shape which also affects the flow pattern near the meniscus region.

Transport of impurities and dopants [34-36] in the growth process is well known as an important factor affecting electrical, mechanical, and optical properties of the crystals. During crystal growth, the pulling crystal has a tendency to entrap some solutes or bubbles from the melt due to segregation. This causes the inhomogeneities of species distribution. For example, during the growth of Yb:S-FAP, an excess of SrF_2 is added to the melt to minimize cloudiness, and also an excess of Yb_2O_3 is used to compensate the segregation coefficient about 0.12. However, convection in the melt produces mixing and alters the characteristic of the diffusion layer especially adjacent to the interface, and causes the concentrations to accumulate or decrease locally. This results in melt inclusion or bubble core formation, and the local cloudiness in the grown crystals. The dopant is added in the beginning of the process, and its concentration changes continuously with the growth. Dopant distribution thus cannot be treated as quasi-static like flow and temperature fields. The calculations for dopant and impurity distribution therefore need to be carried out from the beginning to the end of crystal growth using a very small timestep which makes the problem very challenging.

Crystal cooling process is also a complex procedure combined of conduction, convection, and radiation. During the cooling power is ramped down slowly, and heat generation rate of the Iridium crucible decreases gradually which results in reducing of the system temperature in the furnace. At the different cooling time, the predominating heat transfer modes are different. At the starting of cooling, conduction and radiation is dominant when system temperature is high, while convection becomes very important at the middle or end of the process as system temperature decreases. For some cooling system, the RF coils and gas flow rate for cooling may be modified according to the system temperature to avoid crystal cracking. The numerical study of cracking issue is, thus, a big challenge.

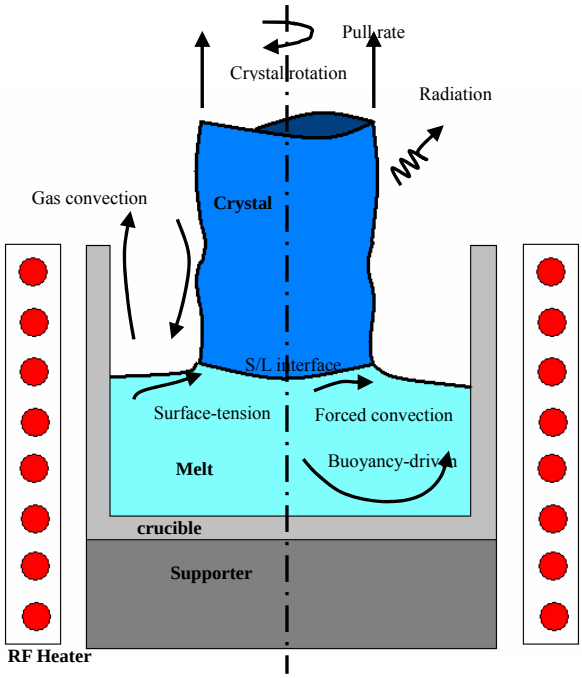

Figure 6 A schematic of the modes of heat transfer in a conventional Cz system

1.3.2 Modeling Issues

High optical quality crystals of Yb:S-FAP are grown by the Czochralski method in a high temperature oxide-type furnace at a melting temperature of approximately 1786℃. The melt is prepared for growth by decomposing $SrHPO_4$, $SrCO_3$, and Yb_2O_3 starting materials to yield a Yb-doped $Sr_3(PO4)_2$ melt, and SrF_2 is added to yield the appropriate composition [13, 14]. The chemical reaction equations can be written as following,

$$3[2SrHPO_4+SrCO_3+xYb_2O_3 \rightarrow Sr_3(PO)_2:Yb+H_2O(g)+CO_2(g)], \quad \textbf{(1.1)}$$

$$3Sr_3(PO)_2:Yb+SrF_2 \rightarrow 2Yb:Sr_5(PO)_3F. \quad \textbf{(1.2)}$$

The appropriate ratios of $SrHPO_4$, $SrCO_3$, and Yb_2O_3 powers are well mixed and then melted in the Iridium crucible. The composition after reaction of Eq.(1.1) is kept molten for approximately 18h to fully decompose the orthophosphate and the carbonate. SrF_2 is then added to the decomposed melt to form the appropriate melt stoichiometry for growth in Eq.(1.2). The final melt is allowed to react and equilibrate

for approximately 5h before initiating the growth of a crystal. Since the solid-to-liquid composition ratio (C_s/C_l) of Yb^{3+} in the S-FAP crystal lattice is approximately 0.12, an excess of Yb_2O_3 is be added to the melt. To control or eliminate the cloudiness defect, a SrF_2-rich melt has been used that also helps to compensate for evaporation losses over the several week growth periods.

As discussed before, the growth of optical crystals has been proven very challenging due to a number of defects. To grow a larger diameter and high optical quality Yb:S-FAP crystal is especially difficult. It has been found that the amount of excess SrF_2 is significant since compositions within 20mole% excess of the stoichiometric composition yield crystals that are cloudiness and large excesses above 33mole% lead to the formation of elongated bubble defects that propagate along the *c* axis in the core region of the grown-boule. These inhomogeneities in crystals are primarily a result of non-steady nature of the growth kinetics due to the initial size of melt volume, and its change from the start to finish [16] resulting in the composition and thermal conditions change in the melt. The reference [13] presented their efforts to grow Yb:S-FAP boules of approximate 3.5cm diameter by 12cm length with defects well controlled (Table 2). Fig.8 shows high optical quality Yb:S-FAP boules at a diameter of 3.5cm [13].

For the large diameter (7cm) Yb:S-FAP crystals, the resolutions in Table 2 have been proven not effective to eliminate all the defects. For example, crystals usually crack using the same cooling procedure as 3.5cm diameter crystals. Bubble core formation is difficult to control using the same crystal rotation rate as 3.5cm diameter crystals. These difficulties result from the change of crystal diameter and crucible size as well as system scales. In this paper, the efforts are being taken to examine the fundamental causes of these defects and to provide good resolutions for the growth of the large diameter crystals. Some progresses have been made. Crack-free 7cm Yb:S-FAP crystals by a length of 28cm have been grown successfully.

Table 2 A summary of the main defects in Yb:S-FAP crystals as well as their possible cause and resolution

Issue	Possibly fundamental cause	Resolution
Cloudiness	Precipitation on line defects	Excess SrF_2 in the melt; annealing over melt
Anomalous absorption	Yb^{3+} in a different site	c-axis along growth direction; axial thermal <60℃/cm
Grain boundaries	Dislocations from the seed or growth instabilities	Seed extensions to grow out boundaries
Bubble core	Constitutional supercooling	Growth stability; maximize thermal gradients
Cracking	Internal stresses	Cool crystals attached to melt; reduce defects
Second phase inclusions	Limited Yb solubility in melt	Yb-doping of <0.75at% in melt; increase thermal gradients

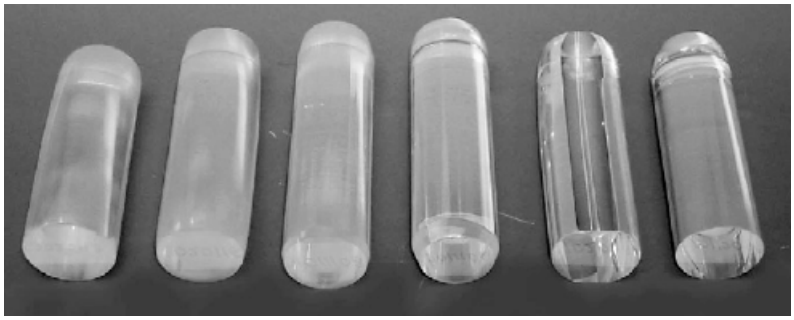

Fig.8. High optical quality Yb:S-FAP boules of 3.5cm in diameter

The complete modeling issues include radiation, convection, induction heating, bubble core, cracking, interface shape, etc. They are usually coupled together, so a coupled model should be present to simulate the crystal growth and cooling process. Since 1975, numerical simulation of Cz crystal growth have been performed by many research groups. These simulations vary from bulk flow approximations that only simulate 2D cavity flows to models that use the global models and incorporate crystal, melt, heater, shield, and many other characteristics. Both finite difference methods (FDM) and finite-element methods (FEM) have been used to simulate the 2D axisymmetric or 3D melt flows. Excellent discussions on modeling and simulation are presented in the reviews written by Chan et al. [37], Brown [38], Müller [39], and more recently, by Hurle [17], and Prasad and Zhang [40]. Since the melt patterns and temperature fields are quite sensitive to the boundary conditions, many different kinds of conditions on the walls of the crucible, crystal-melt interface, and free-surface have been considered.

The primary difficulty in the modeling Cz flows arises from the fact that the positions of the crystal-melt interface and melt-gas meniscus are neither known a priori nor planar. The crystal-melt interface coincides with the freezing point isotherm in the system, and the melt meniscus results a force balance between the surface tension, pressure forces, and viscosity stresses. Earlier studies in the area of FEM were performed by Brown et al. [41-44]. They developed an integrated hydrodynamics thermocapillary model, which allowed for the calculation of both the interface and the meniscus shapes. Heat transfer was simulated by conduction, diffuse gray radiation between all components within the Cz apparatus, and axisymmetric steady-state laminar convection in the melt. Crystal radius is computed simultaneously and self-consistently with the heat transfer throughout the system. Other important studies were performed by Crowley et al. [45]. They treated all the interfaces, the solidification front, the meniscus, and crystal walls, as unknown in the problem in order to perform time-dependent simulations and to analyze the dynamics of the system. Efforts also have been made to consider convective flows in the melt to interact between the global heat transfer and melt convection and to update the S/L interface based on this interaction [46].

In the area of the FDM and FVM, the applicability of these methods for complex geometrical domains has been greatly enhanced by numerical grid generation with

body-fitted coordinate system. Most recently, a multizone adaptive grid generation combined with a curvilinear coordinate FVM developed by Zhang et al. [47-49] has been implemented to simulate the low- and high-pressure crystal growth processes [50, 51]. These authors also have shown the importance of grid adaptivity and grid resolution, particularly with respect to the dynamics of the crystal-melt interface, free surfaces, and melt meniscus. Several studies also have been conducted to examine the effect of magnetic field on Cz growth system by applying the MHD equations [50]. The turbulent flow in the melt phase was first studies by Ristorcelli and Lumley [52], and later by Ono et al. [53], Kinney [54, 55], Brown [38], and Zhang et al. [56].

1.4 Literature Review

1.4.1 Study of Yb:S-FAP Crystal Growth

Experimental studies have been conducted in Lawrence Livermore National Laboratory for a long period[13, 14]. The Czochralski growth system for Yb:S-FAP crystal growth is shown in Figure 7. Crystals are grown from an iridium crucible used to accommodate a melting temperature of approximately 1786℃. The crucible is supported by zirconia ceramic disks. Zirconia tubes and grog are used as the insulation for the furnace walls. Nitrogen flows into create an inert environment for the crystal growth, preventing the melt components and iridium crucible from oxidation. The Nitrogen flows into the furnace from the bottom and the top through special holes, so the flow structure in the furnace is three dimensional. The crystals are grown from seeds attached to an iridium coupler and held by an alumina rod. It is rotating at a rate of 15rpm to reduce some defects when being pulled by the alumina tube at a speed of 0.5mm/h. The crucible is inductively heated by copper coils with AC current at a frequency of 25 kHZ. The input power is 50KW with a use of 40~50 percent. The growth furnace is also used for crystal cooling. Due to their efforts, 3.5cm diameter crystals have been produced routinely. These achievements are mainly contributed to experimental studies. When 7cm diameter crystals were to be grown, defects that have been resolved rose again. Therefore, they found us for numerical study of Yb:S-FAP crystal growth. Due to our efforts[57-63], the risen defects have been resolved, which makes it possible to growth large diameter crystals routinely. It shows both numerical study and experimental study are necessary for the

growth of high quality crystals.

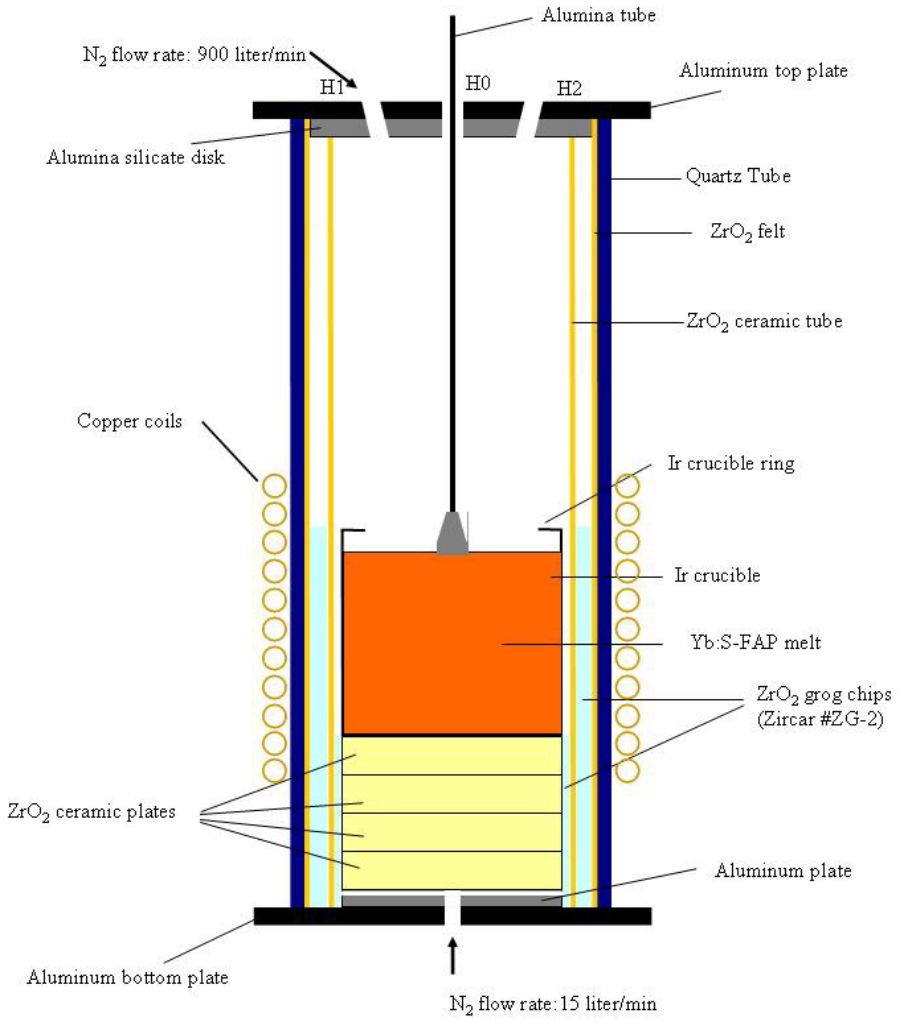

Figure 7 Schematic of Yb:S-FAP crystal growth system (originated from LLNL)

1.4.2 Study of Cracking

Crystal cracking during cool down is directly related to the buildup of thermal stresses and associated strains. Brice has examined thermal strain in the crystal during growth and cooling [30]. He suggests that crystal cracks as the result of tensile stress and provides an approximate analysis of thermal strain. In his analysis, it is assumed that crystal bottom is attached to melt and other potion of the crystal is exposed to a constant temperature ambient and loses heat through convection. The Biot number is assumed to be much less than unity so that the analytical solution can be approximate

using the first term, the maximum cooling rate can be written as [30]

$$[dT/dt]_{\max} = 2\sqrt{2}k\varepsilon_b / (c\beta R^2) \tag{1.3}$$

where k is the thermal conductivity, c is the specific heat per unit volume, β is the expansion coefficient, R is the crystal radius, and ε_b is the critical strain. Related to the maximum cooling rate, there exists a critical radial temperature difference,

$$\left(\triangle T_R\right)_b = \left(\frac{R^2 c}{4k}\right)\left(\frac{dT}{dt}\right)_{\max} = \frac{\varepsilon_b}{\sqrt{2}\beta} \sim \frac{\varepsilon_b}{\beta} \tag{1.4}$$

Recently, Metzger and Backofen [64] simulated the annealing process for GaAs crystal growth. They showed that the evolution of the maximum stress was strongly correlated to the radial temperature difference between the center and the edge of the crystal. This provides us an important idea to simplify our problem in the following analysis.

1.4.3 Study of Melt Inclusion

The study of the effect of gases on the solidification process can be dated back over 160 years ago, and the subject has received more attention since the early 1900s [65]. Theoretically study of the gas bubble nucleation during the crystallization of a muti-component gas solution was presented by Wilcox and Kuo [66]. They observed that heterogeneous nucleation on the crystal interface is the mechanism for the bubble formation. They also provided a theory to demonstrate that the tendency to form gas bubbles increases with increasing growth rate and ambient pressure, and decreasing stirring and height of liquid over solid. The development of blowholes of carbon dioxide in water were experimentally studied by Vasconcellos and Beech [67]. It was concluded that the form of bowholes was related to the solute profile. Nucleation and evolution of gas bubbles ahead of a solidification front were theoretically and experimentally studied for magnetoelectric composite materials contaminated with a volatile components (*P* in *Si*, for instant) [68]. They found that the way of avoiding high contamination, setting either a very lower interface velocity, or setting an extreme high solidification rate can be used to prevent the formation of gas bubbles ahead of a solidification front. Recently, quantification of gas segregation due to the moving solid-liquid front was studied by Marcus, et al [69]. In the study, an analysis had been carried out to predict the gas concentration in the melt for different solidification rates.

In order to understand the process of gas bubble formation in the solidified material, water is usually used for a direct observation for easy visualization [70]. The

generation and trapping of gas bubbles in freezing water are well-known [71]. Chalmers interpreted that air rejected by the solidification front accumulates in water near the interface until concentration is high enough for bubbles to nucleate [72]. Whether it continues to exist or disappear depends on its radius. If the radius reaches the critical radius for the bubble to exist in equilibrium with the surrounding liquid, it will grow due to air diffusion into it. If the interface continues to move forward, the bubble cannot grow laterally but forward to form a cylindrical pore, known as 'ice worm' [73]. The ice worm looks like a string of pearls due to the fluctuation of solidification rate (see Figure 8). When freezing is slow, the bubbles grow larger; during fast growth, the formation of ice worms is suppressed and replaced by a large number of very small and round bubbles. Extremely slow freezing provides enough time for air to diffuse away from interface, so that neither bubbles nor ice worm can be observed. Ice grown in flowing water is usually free of bubbles and ice worms, which results from the fact that the continuous movement of water prevents the precipitation of air near the growing interface. Murakami and Nakajima [74] measured the radii and periodic distances between columnar pores for different growth rates and supersaturations of water-carbon dioxide solution. In situ observation and interpretation of the shapes of the bubbles generated and trapped in the solid as pores have been presented by Wei et al recently [75].

In summary, melt inclusion/bubble core formation can be divided into seven steps: (1) pileup of gas or solute near the S/L interface by gas segregation from the solid; (2) nucleation on the solidification front; (3) growth of the bubbles/particles; (4) disappearance of the bubbles/particles; (5) entrapment of bubbles/particles; (6) solidification rate-controlled elongation; and (7) formation of melt inclusion/bubble core in the solidified zone. The schematic for these steps are shown in Figure 9.

Figure 8 Bubbles in freezing water

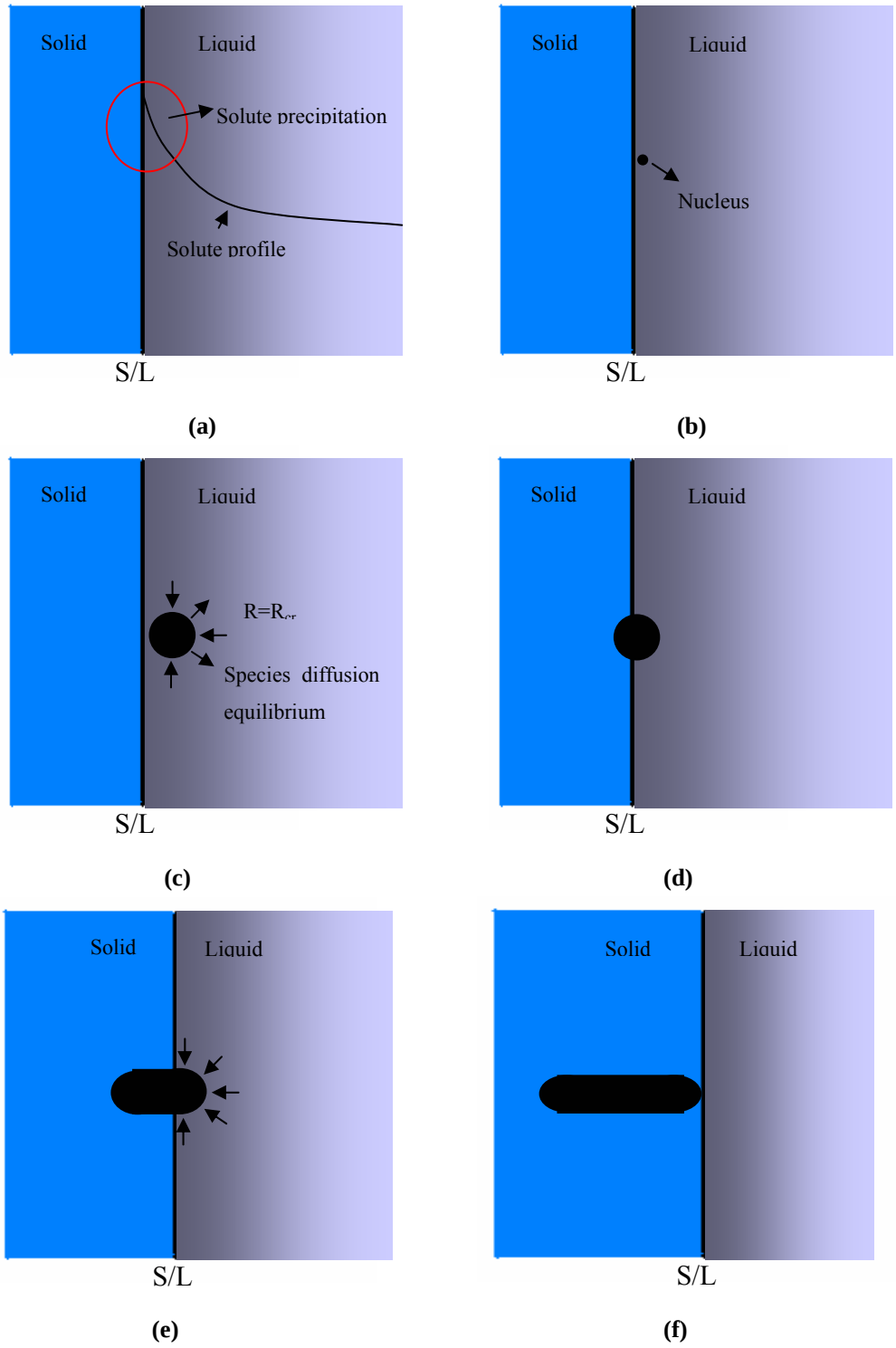

Figure 9 Steps of melt inclusion/bubble core formation, (a) Solute precipitation near S/L interface, (b) Nucleation in the solidification front, (c) Growth of the particle, (d) Entrapment of the particle, (e) Elongation of entrapped particle, and (f) Final formation of melt inclusion

1.5 Research Objective and Approach

In this thesis, the aims will focus on model development and validation, determination of control parameters for melt inclusion, interface shape and dopant distribution control, gas partition/gas channel design, cooling profile optimization for crystal cracking. The topics of radiation, inductive heating, heat transfer, melt inclusion, cracking will be studied.

1.5.1 Model Development and Validation

Using the in-house developed induction RF heating and Czochralski crystal growth codes and a commercial CFD-ACE+ (from the ESI group, formerly CFDRC) code, the computational models for Yb:S-FAP Czochralski growth system will be developed. All important elements will be included in the models, and modeling results will be compared with experiments at each stage of the development. The required features for modeling the growth system include inductively RF heated system, strong gas convection, melt flow and heat transfer due to buoyancy, crystal rotation, radiation in the laser material crystal, and solidification shape and dynamics. The following preliminary results are available currently: (1) temperature distribution in the entire furnace for coil geometry/position (Figure 10); (2) gas flow and temperature distribution in the furnace (Figure 11); and (3) interface shape as a function of pulling and crystal rotation rates (Figure 12). The primary work in this task will be validating the computational model for Yb:S-FAP crystal growth. Simulation will be conducted for the same geometry configuration and operational conditions in the experiments.

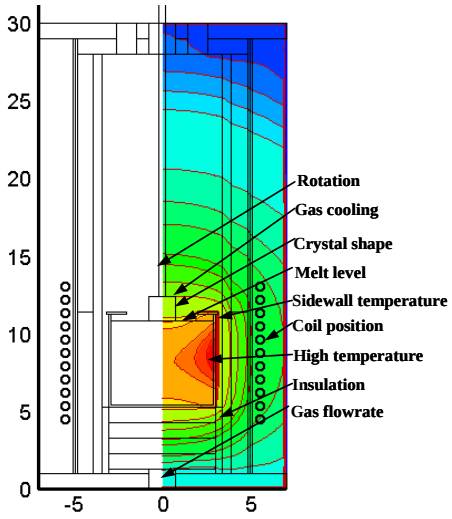

Figure 10 Temperature distribution in the furnace

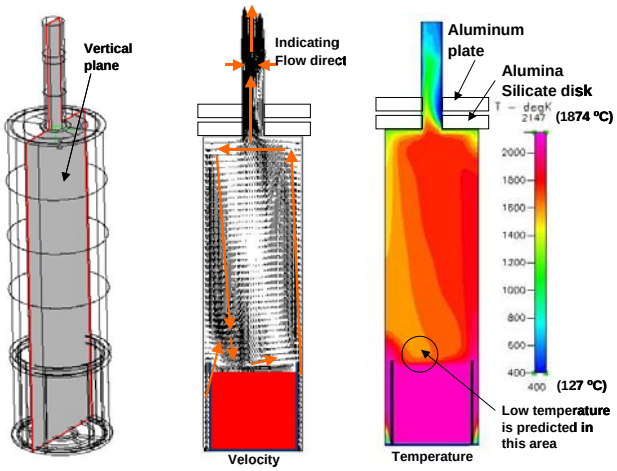

Figure 11 The predicted gas flow and temperature distribution

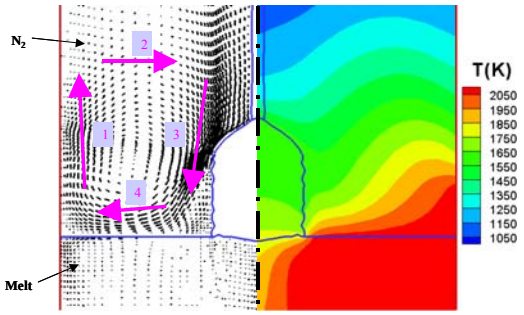

Figure 12 The predicted interface shape for a prescribed crystal shape

1.5.2 Optimization of Growth Furnace Design

Furnace geometries are significant for the successful growth and cooling of crystals. Different furnace designs, such as Ir ring, will be proposed and modeled. The optimal design will be suggested for implementation in the actual growth system, and then improved by feedback from experiments.

1.5.3 Cooling Profile Optimization for Crystal Cracking

A constant cooling slope is used in the current experiments for large diameter crystal. The crystal is usually cracked during the second day. It is believed that cracking occurs at the lower temperature region. Song et al. [76] has measured thermal expansion coefficient of Yb:FAP crystal as a function of temperature. Based on the available information, a slow cooling rate would be preferable at cracking temperature to avoid high stress and minimize cracking. Thus, a cooling profile is necessary for the materials with such behavior. The existing data of Yb:FAP will be used in the modeling to simulate the cooling process. A cooling profile will be determined to ensure no large stress presented in the entire cooling process. The achieved optimized power ramp-down profile will be approximated by a tri-linear power ramp-down profile so that it can be used practically.

At first step, 1D model will be presented. The results from this simulation will be approved by experiments. 2D or 3D simulation also will be conducted to improve the cooling theory. The cooling profile will be verified and developed according to new experimental data. After getting some crack-free crystals, furnace or cooling process will be improved in design to reduce the cooling time.

1.5.4 Interface Shape and Melt Inclusion Control

Melt inclusion is correlated to the solidification rate (pulling rate and crystal shape), rotation rate and gas convection. Different crystal rotation rates will be tested during the constant diameter growth, and information of interface shape and flow

patterns in the melt will be achieved. Such information will allow us to understand how melt inclusion is formed and to determine the sensitivity rotation rate on melt inclusion. The simulation results will be compared to the experimental results. This comparison will allow the further validation of the computational code with crystal growth. Modeling effort will be tied to the actual growth experiments for effective elimination of solute pileup and melt inclusion.

It is a common practice for Czochralski growth to optimize the pulling and rotation rates to sweep off defects from the growth interface, as shown in Figure 13. A flat interface (or convex to the melt) is favorable for reducing crack and grain boundaries. It may also benefit to the melt inclusion control. A concave interface may be the reason for species moving towards the center of the crystal and a convex interface for causing melt inclusion spreading because a convex interface may push the dopant away from the growth interface. To eliminate melt inclusion, it is important to make G_l/V high and keep the interface shape unchanged for the entire growth process. It is possible to determine the optimal pulling and rotation rates under certain gas convection. More accurate relationship should be found from process modeling. Specific activities are proposed as follows.

Theoretical/analytical study will be performed to correlate melt inclusion with crystal rotation rate. We can control the interface shape to concentrate melt inclusion in a narrow region. With the current understanding, it may not be feasible to eliminate melt inclusion fully due to the requirement for certain species with sufficient amount so as to be incorporated into the crystal.

The following methods can be used to make the interface less concave or more convex for the current system: (a) lowering crystal rotation rate; (b) cooling the crucible base; (c) using a large crucible; (d) increasing the sidewall temperature through moving coil position upward; (e) using a shallow melt; (f) reducing the pulling rate; and (g) using the radiation shield [77]. From the interface shape, solidification rate, and dopant distribution, the conditions at which the interface breaks down may be determined. Numerical model can further help us find a way to push melt inclusion at a narrow central area or peripheral area.

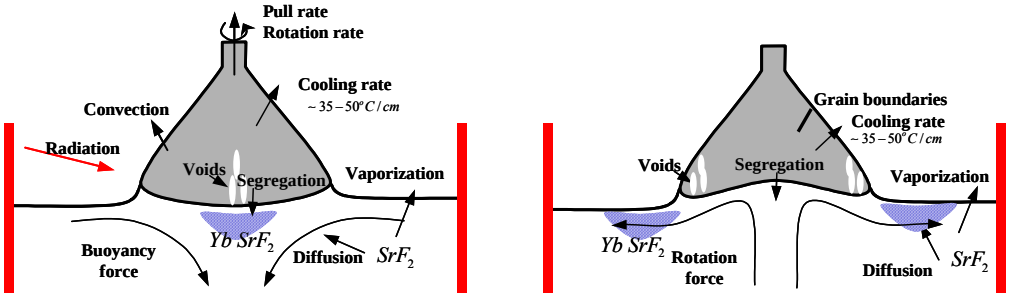

(a) low rotation rate (b) high rotation rate

Figure 13 Dopant distribution variation due to crystal rotation.

1.5.5 Modeling of free surface flows

It is significant to model melt convection. Our former simulation is based on grids. However, the grid resolution should be increased to get accurate results. In some cases, in which free surface have large distortion, grid-based method results in some significant scheme defects, such as large numerical diffusion. Efforts are conducted to model free surface problems accurately and conveniently. First of all, a numerical method should be found for this aim. This problem involves free surface flows and droplet dynamics. A meshless method called Smoothed Particle Hydrodynamics has been introduced. Before doing simulation for our problems, the SPH method should be developed and a SPH code should be improved. At last stage, a method combined SPH and FVM should be developed to fulfill our objects. The data transfer between meshless method and grid-based method should be studied carefully. Due to time limit, this thesis only includes development and testing of SPH method. Pressure-correction equation, surface tension, and solidification model have been developed. Single droplet behaviors with or without gravity have been simulated as testing cases. Free surface flows in the melt will be conducted in the future.

1.6 Preview of the Thesis

Chapter 2 presents mathematical models and experimental results for studying crystal cracking. In section 2.2, the important assumed value of critical temperature difference is discussed. Section 2.3 and 2.4 provides mathematical model and experimental cases, respectively. In section 2.5, some additional methods to reduce cool time will be studied.

Chapter 3 reviews the mechanisms for melt inclusion (section 3.2), presents a method to control melt inclusion (section 3.3), and discusses mathematical model (section 3.4). Simulation results and experimental cases are presented in section 3.5.

In chapter 4, a meshless method called Smoothed Particle Hydrodynamics (SPH) is introduced to explain melt inclusion. Traditional SPH method is presented in section 4.1, and improved SPH method is presented in section 4.2. In section 4.3, the applications of improved SPH on droplet impact and solidification are studied.

Chapter 5 summarizes the work done in this thesis and comments on the future work are presented.

Chapter 2 Optimization of Cooling Profile

2.1 Review of Crystal Cracking

A long upper lasing lifetime (1 ms), moderate saturation fluence (3 J/cm^2), and low energy defect (pump 980 nm, extract 1047 nm) makes Yb-S-FAP crystal an attractive laser host for diode pumping in moderate thermal load applications [7]. Currently, 7.0 cm diameter Yb:S-FAP crystals are being grown by using the Czochralski method from a SrF_2-rich melt [13, 14]. The growth of these crystals offers several challenges, which were resolved for 3.5 cm diameter. Specifically relating to this research, cracking was eliminated by reducing defects, cooling crystals using mono-linear cool-down power profile and leaving the crystal in contact with the melt during cooling. However, in scaling to 7.0 cm diameter, modifications to this procedure are required to prevent cracking.

Crystal cracking during cool down is directly related to the buildup of thermal stress and associated strains. Since Yb:S-FAP crystals have cylindrical symmetry, for simplicity of modeling, the total thermal stress within the crystal boule can be characterized by the radial and axial components. There are critical thermal stresses along both directions, above which, the crystal will be subject to cracking and it is believed that these critical values are temperature dependent. For example, at the beginning of the cool down when the temperature of the furnace is high, the crystal can usually sustain a large temperature difference in the radial direction without cracking. It should be noted that defects such as bubble core may significantly affect the critical values and cause them to be lower than modeled. Thus, depending on the level and distribution of thermal stress during the cool down, cracks can happen within the crystal along axial, radial or both directions.

In situ measurements of the temperature distribution within the crystal and its surroundings during growth and cool-down are not practical in this case and significantly disturb the system thermodynamics. Therefore, numerical simulations of the growth and post-growth cool down are an ideal alternative to understanding the fundamental causes for issues related to crystal quality. In addition, numerical simulation of the growth furnace makes it possible to predict the temperature distribution within the crystal and its surroundings, temperature gradients within the

furnace, and the relationship of these components with the power applied during the growth and cool down processes. Simulation results can be benchmarked against experimental observations to optimize growth and cool down parameters for growing high quality crystals with suppressed cracking.

Brice [30] examined thermal strain in the crystal during growth and cooling, and obtained the analytical solution for the maximum allowed cooling rate. Related to the maximum cooling rate, there exists a critical radial temperature difference between the center and the edge of the crystal above which the crystal will crack. This analysis was acceptable for crystals with a small value of ratio of diameter to length and weak radiation heat losses [78]. Recently, Metzger and Backofen [64] simulated the annealing process for GaAs crystal growth. They showed that the evolution of the maximum stress was strongly correlated to the radial temperature difference between the center and the edge of the crystal. The predicted radial temperature differences across the crystal by one- and two-dimensional models displayed similar behavior. Furthermore, a one-dimensional model was employed to optimize the cooling process in which the radial temperature difference was required to be limited by a critical value. The above analysis established the relationship between radial temperature difference and thermal strain induced in the cylindrical crystal. Although this paper concentrated on modeling the growth of GaAs, a similar approach may be applicable to the current study for Yb:S-FAP crystals.

2.2 Assumed Critical Values

In order to determine the optimal cooling profile that prevents the crystal from cracking during cool down, the simulation model must be validated. First, the value of the critical radial temperature above which cracking will occur is required. Since this value is not readily available for Yb:S-FAP crystals, it is estimated through simulations and verified by experiments bearing mono-linear and bi-linear cooling profiles, respectively. The assumed critical radial temperature difference in the simulation is shown in Figure 14. The characteristics of the assumed values are based on the belief that the critical values are temperature dependent and are small at lower temperatures and large at higher temperatures.

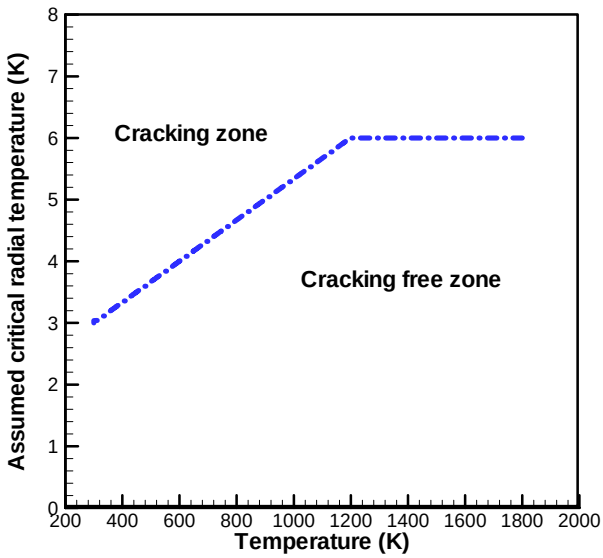

Figure 14 The critical radial temperature difference used in the simulations.

2.3 Mathematical Models

A numerical model has been developed to simulate the temperature profile of the Yb:S-FAP crystal grown in the CZ furnace shown in Figure 15. The radio-frequency (RF) induction heating method is used [79-82] for a standard oxide-type furnace. Figure 16 shows the configuration of the crucible and crystal position during cool down. In this Figure, R is the radius of the crystal, $T(0)$ and $T(R)$ are temperatures at the center and surface of the crystal, respectively, T_c is the crucible temperature, and *Tsur* is the crystal surrounding temperature that is measured at the center between the crystal surface and the inner diameter of the Iridium ring as shown.

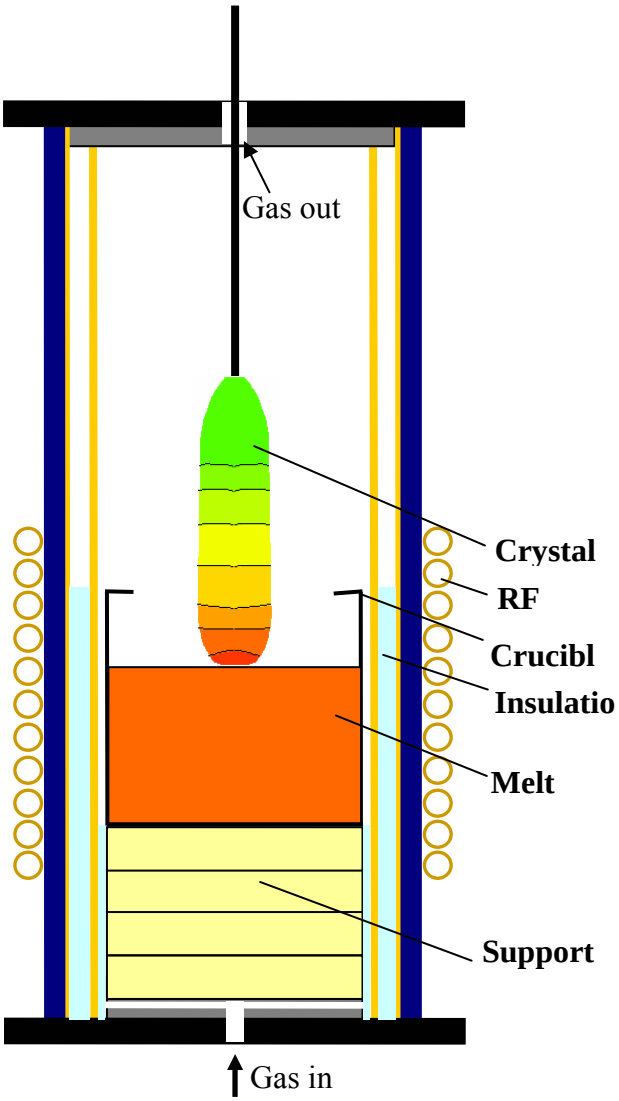

Figure 15 Schematic of the growth furnace

Simulations were performed first to examine the effect of internal radiation from the crystal during cool down to determine the conditions under which the crystal cracks. The numerical model is then used to optimize the cooling profile by ensuring that the thermal stresses in the crystal are maintained within a critical value throughout cooling. While both radial and axial temperature gradients may contribute to cracking, for simplicity, the current study considers that cracks only originate from the radial temperature gradient. Simulation results from the one dimensional model suggest that the crystal can be cooled faster at high temperature but must be cooled at a slower rate at lower temperatures.

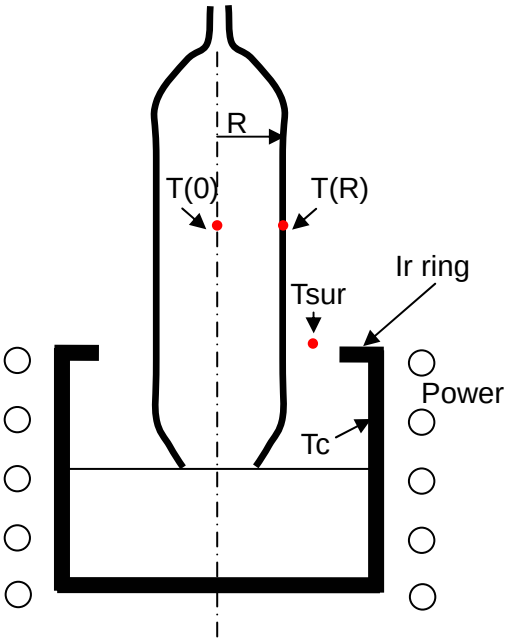

Figure 16 Schematic of the simplified crystal cooling process. Tc: Crucible temperature, Tsur: Crystal surrounding temperature, T(0): Crystal center temperature, and T(R): Crystal surface temperature

2.3.1 The Outer Model

To determine the optimal cool-down profile, the proper relationship between the heating power and temperature distribution within the crystal growth furnace needed to be derived. A simplified cooling model has been built based on dynamic models and process control discussed in references [64, 83-86]. Although this analysis method does not consider all parameters, it effectively reflects the major characteristics of the growth system. Process control for the experimental growth system is treated as a simple dynamic system with the system energy as the input and the average system temperature T_f, as the output. The system energy is provided by RF induction heating and the heat loss is restricted to the environment (with temperature T_∞) only. Thus the following equation can be used to describe the energy balance of the system,

$$mc_p \frac{dT_f}{dt} = P - h_{eff,f} A_f \left(T_f - T_\infty\right), \tag{2.1}$$

where P is the power of the RF induction heater, m is the mass of the furnace, c_p is the heat capacity of the furnace, $h_{eff,f}$ is the effective heat transfer coefficient between the furnace and environment around the furnace, and A_f is the total surface area of

furnace. Because T_f is hard to define, it is replaced by the gas temperature surrounding the crystal, T_{sur}, by approximation without missing major characteristics. Therefore, Equation (2.1) can be rewritten as

$$\left(mc_p\right)' \frac{dT_{sur}}{dt} = P - \left(h_{eff,f} A_f\right)' \left(T_{sur} - T_\infty\right), \tag{2.2}$$

where $\left(mc_p\right)'$ and $\left(h_{eff,f} A_f\right)'$ having different values from that of mcp and $h_{eff,f} A_f$. For a steady state, dT_{sur}/dt, is zero, and $\left(h_{eff,f} A_f\right)'$ can be obtained from $\left(h_{eff,f} A_f\right)' = \frac{P}{T_{sur} - T_\infty}$ for any given power. A thermocouple assembled in the system for control purpose can measure the temperature near the heater for different heating powers. This allows us to determine $\left(h_{eff,f} A_f\right)'$. However, the location of thermocouple for temperature measurement is not at the exact location as model assumed, e.g., a place near the crystal, T_{sur}. The afore-determined $\left(h_{eff,f} A_f\right)'$ is therefore needed to be modified. In this paper, $\left(h_{eff,f} A_f\right)'$ is assumed to be constant for simplification. Furthermore, by monitoring T_{sur} as a function of time and power, the value of $\left(mc_p\right)'$ can also be determined by equation (2.2). They can be improved by describing them as a time-dependent function for more detailed analysis.

As the cooling is initiated, the power level is turned down slowly. The power ramp-down rate is represented as $\Delta P/\Delta t_0$, where Δt_0 is a constant for experiments. In the model optimization, ΔP must be determined at every step so as to control the induced temperature difference. Since the effective thermal conductivity, k_{eff}, is a strong function of temperature, and the crystal surrounding temperature, T_{sur}, is a function of the power level, no analysis solution is therefore possible. Within each time step, Δt_0, the power level, P, can be treated as a constant; Equation (2.2) can be rewritten as follows

$$\frac{d\theta}{dt} = -\chi\theta, \qquad \text{at each time step} \tag{2.3}$$

where $\theta = P/\left(h_{eff,f} A_f\right)' - (T_{sur} - T_\infty)$ and $\chi = \left(h_{eff,f} A_f\right)' / \left(mc_p\right)'$. From Equation (2.3) with initial condition, the relationship between P and Tsur can be established. At the end, the following relationship can be obtained,

$$\Delta P = \left(h_{eff,f} A_f\right)' \left[\Delta T_{sur} + \int_t^{t+\Delta t_o} \lambda(t) dt\right], \qquad \text{for each time step} \tag{2.4}$$

where $\lambda(t) = \theta_0 \chi e^{-\chi t}$. It is apparent from the equation that as heating power is

ramped down, the system temperature as well as the surrounding temperature is reduced. To make the optimization procedure simpler, we further approximate the relationship between ΔP and ΔT_{sur} as

$$\Delta P = \left(h_{eff,f} A_f\right)' \Delta T_{sur} \quad (2.5)$$

Equation (2.3) can also be used in the optimization. However, more data such as $\left(mc_p\right)'$ is required. The effective convection heat transfer coefficient, $h_{eff,f}$, in Eq. (2.5) is defined as $h_1 + 4\varepsilon\sigma T_{sur}^3(R)$ where h_1 is the convection heat transfer coefficient. Since the growth system is complex, some simplifications as discussed above have been made to get Eq.(2.5). Further improvement of the analysis can be made through data gained by both experiment and simulation.

2.4.3 The Boundary Treatment

For CZ crystal growth, several radiation models are available [87] to relate crystal temperature to ramp-down power. For simplification, the effective convection heat transfer coefficient is used to take into account of convection, radiation effects. Thus the energy balance equation on the crystal surface can be written as

$$\begin{aligned} P_l(t) &\approx h_2\left[T(R,t) - T_{sur}(t)\right] + \varepsilon F_{cf}\sigma\left[T^4(R,t) - T_{sur}^4(t)\right] \\ &\approx \left[h_2 + 4\varepsilon F_{cf}\sigma T^3(R)\right]\left[T(R,t) - T_{sur}(t)\right] = h_{2,eff}\left[T(R,t) - T_{sur}(t)\right] \end{aligned} \quad (2.6)$$

where P_l is the heat loss from the crystal surface to the surrounding gas, F_{cf} is the view factor from the crystal to its surrounding, h_2 is the convection heat transfer coefficient, and ε is the emissivity of the crystal surface. Equation (2.6) will be used to determine the boundary conditions for the crystal for crystal temperature calculations.

2.4.3 The Inner Model

Experimental results show that crystal cracking normally occurs at the Iridium ring where the temperature gradients in the crystal are the largest. Thus we assume this area along the length of the crystal dominates the cooling process and the radial temperature difference can be chosen as the control parameter. During cooling, the power level is reduced in time duration, Δt_0. In the current study, Δt_0 is chosen as five minutes, indicating the induction heating power is adjusted every five minutes. A one-dimensional energy equation together with boundary and initial conditions can be written as,

$$\frac{1}{r}\left[\frac{\partial}{\partial r}\left(rk\frac{\partial T}{\partial r}\right)\right]=\frac{\partial(\rho c_p T)}{\partial t},\quad 0\le r\le R,\quad t_0<t\le t_0+\triangle t_0 \tag{2.7}$$

$$\frac{\partial T}{\partial r}+\frac{h_{2,eff}}{k_{eff}}(T-T_{sur})=0,\quad r=R,\quad t_0<t\le t_0+\triangle t \tag{2.8}$$

$$T=T(t_0,r),\quad 0\le r\le R,\quad t=t_0 \tag{2.9}$$

where $h_{2,eff}$ is the effective convection heat transfer coefficient of the gas surrounding the crystal and k_{eff} is the effective thermal conductivity of the crystal. In the boundary conditions for Eq.(2.8) the crystal surface heat loss from Eq.(2.6) is applied. Since Yb:S-FAP is a transparent optical material, inner radiation is high, particularly when the crystal temperature is high. The internal radiation can be approximated by the simplest Rosseland model [88] using the effective thermal conductivity.

$$k_{eff}=k_s+k_r,\ k_r=\frac{16n^2\sigma T^3}{3a_R} \tag{2.10}$$

where k_s is the thermal conductivity of the crystal, k_r is the portion of thermal conductivity from radiation, n is the refractive index of the surrounding gas which is approximate to unit for nitrogen, σ is the Stefan-Boltzmann constant, and α_R is the Rosseland mean absorption coefficient. The value of effective thermal conductivity depends strongly on the crystal temperature as shown in Figure 17. In our simulation, α_R is set to 100.

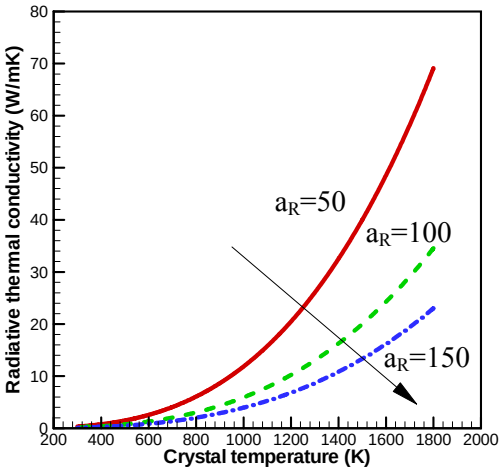

Figure 17 Effect of radiation heat transfer on effective thermal conductivity

Assume thermal properties may not change within every power control interval, e.g., five minutes, the analytical solution of Eq. (2.9) is obtained as [89]

$$T(r,t)=\frac{2}{R^2}\sum_{m=1}^{\infty}e^{-\alpha\beta_m^2 t}\frac{\beta_m^2 J_0\left(\beta_m r\right)}{\left[\beta_m^2+\left(h_{2,eff}/k_{eff}\right)^2\right]J_0^2\left(\beta_m R\right)}\int_0^R r' J_0\left(\beta_m r'\right)T(t_0,r')dr' \tag{2.11}$$

where α is the thermal diffusivity, $J_0(x)$ is the Bessel function, and β_m represents the positive roots of

$$\beta_m J_0'\left(\beta_m R\right)+\left(h_{2,eff}/k_{eff}\right)J_0\left(\beta_m R\right)=0 \tag{2.12}$$

Since Eq.(2.12) is an infinite series, it is necessary to keep the first several terms as an approximation, which is accurate when the Biot number is not large. Based on the analytical solution of the temperature distribution, the relationship between the radial temperature difference and power ramp down rate can be established.

2.4 The Procedure to Achieved Optimized Cooling Profile

An initial power change is assumed to perform the optimization. The crystal temperature distribution is then simulated by applying Eqs. (2.1)-(2.12), where the crystal radial temperature differences are calculated and compared with the critical values. If the predicted crystal radial temperature difference is larger than that of the critical differences, the power change used in the current time step has to be reduced in order to limit the thermal stress in the radial direction within the crack free regime. This procedure is reiterated until a proper power ramp down profile is obtained such

that the achieved radial temperature difference equals the critical value. The optimizing procedures are summarized in Figure 18. It is noted that the radial temperature difference in crystal should be maintained at a level smaller than the critical radial temperature difference to avoid cracking. The mathematical formula for this constraint is described as follows,

$$\Delta T_R = T(0) - T(R) \le \Delta T_{R,cri} . \tag{2.13}$$

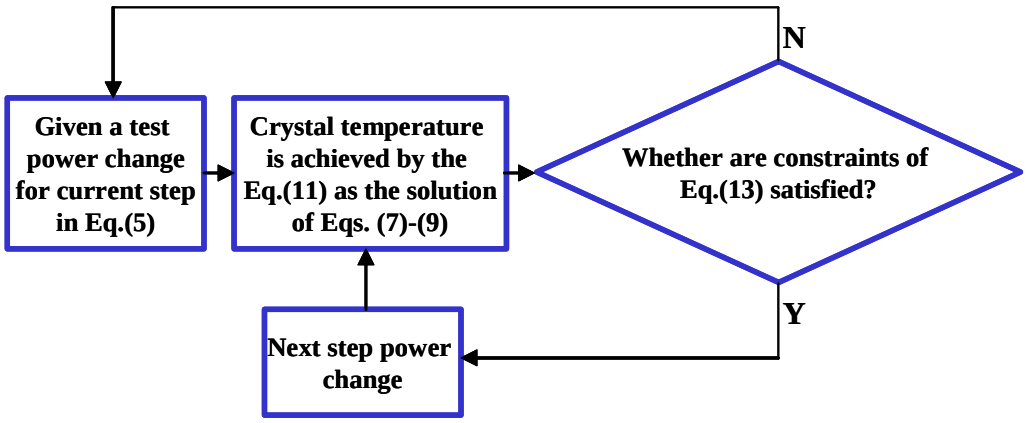

Figure 18 Flowchart of the optimizing procedure

Table 3 lists the material properties that were used in this simulation [13]. The assumed critical radial temperature difference is shown in Figure 14. The furnace surface area A_f is approximated to be 0.67 m^2. The convection heat transfer coefficient $h_{2,eff}$ is set to a value of 40 W/m^2K. The effective heat transfer coefficient $h_{eff,f}$ is given as 20 W/m^2K. The initial crystal temperature is chosen to be 1800K, lower than the melt temperature of 2059K, based on the fact that the average crystal temperature is lower than the melt temperature at the start of the cool down.

Table 3 Thermophysical properties of Yb:S-FAP crystal used in the simulation

Property	Value
Density, ρ (g/cm^3)	4.14
Heat capacity, C_p (J/gK) @ 298 K	0.5
Thermal diffusivity, α (m^2/s)	9.8×10^{-7}
Thermal conductivity, k_s (W/mK)	2.0

2.4.3 One-linear Power Ramp-down Profile

Actual temperature and temperature differences along the radial directions were simulated for a system that was cooled under a mono-linear forty-eight-hour cooling profile. The power level during the cooling period and its corresponding crystal surrounding temperatures are shown in Figure 6 (a). The dashed-dotted line in Figure 6 (b) shows the assumed critical radial temperature difference. The solid line represents the radial temperature differences during cool down. It is seen that the temperature difference along the radial direction increases with time. The solid curve intercepts the critical value at 37 hours suggesting that, under the current assumption, after 37 hours, the crystal is susceptible to cracking. Note that the radial temperature could reach 50K when the power level is decreased to 0%. The predicted crack zone is marked by the hatched solid lines.

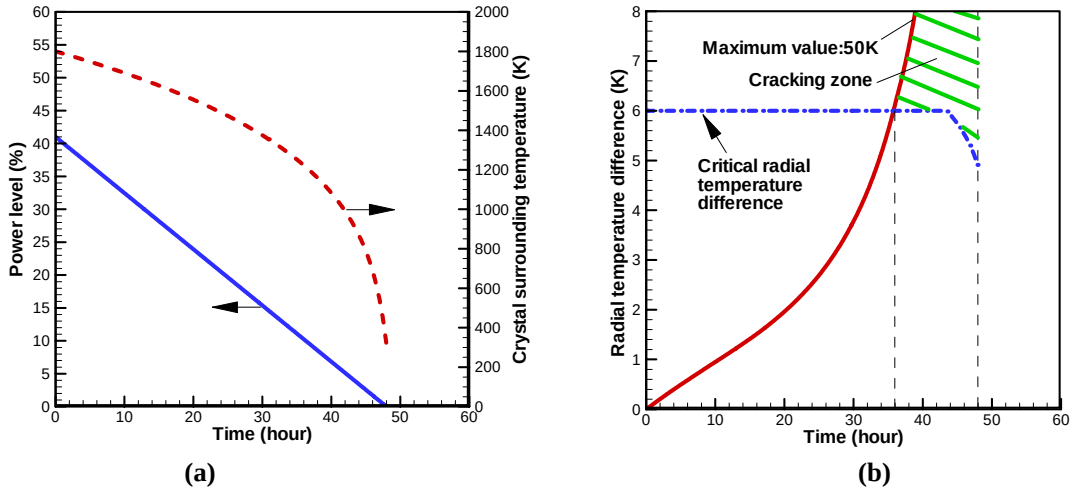

Figure 19 (a) Linear power ramp-down profile and surrounding gas temperature change profile, and (b) radial temperature difference induced in the crystal.

2.4.3 Bi-linear Power Ramp-down Profile

Similar calculations were done with a system that is cooled under a ninety-six hour bi-linear cooling profile. The calculated results are plotted in Figure 20(a) and

(b). In Figure 20(b), the crystal is predicted to crack after 78 hours of cooling. Note that the radial temperature could reach 36K when the power level is decreased to 0%. The crack zone is marked with the green solid lines.

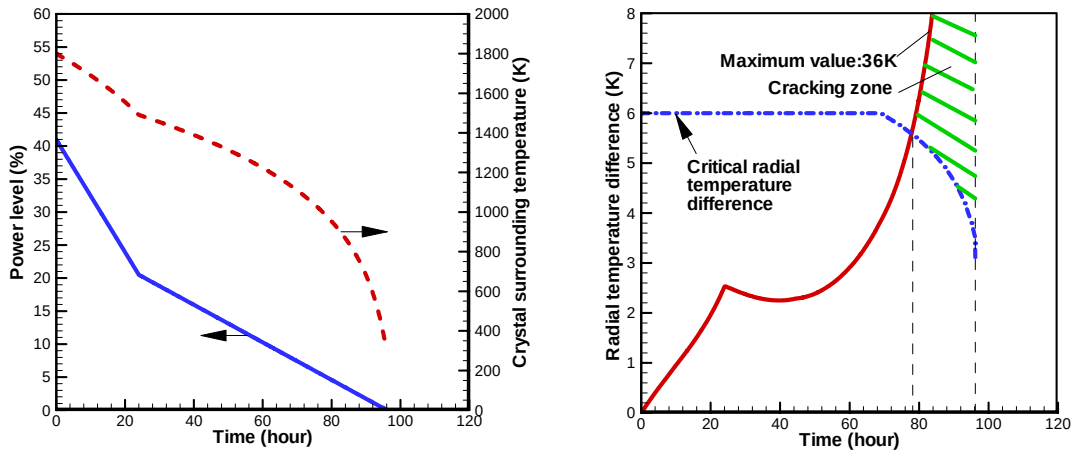

Figure 20 (a) Bi-linear power ramp-down profile and surrounding gas temperature change profile, and (b) radial temperature difference induced in the crystal

Under both cooling profiles, the temperature difference between the center and the edge of the crystal is small at the beginning, but reaches very high values at lower temperatures. This phenomenon can be attributed to the fact that the effective thermal conductivity within the crystal is significantly reduced at lower temperatures (Figure 17). Therefore, while the surface temperature is reduced due to the heat loss from convection and radiation, the temperature at the center can still be very high suggesting that it is necessary to reduce the cooling rate at low temperatures to allow for better temperature equilibration between the center and outside of the crystal to suppress cracking.

In the experiment, the cracking time period is consistent with the simulation results of Figure 19 and Figure 20, but the exact cracking time was not documented. In the experiments, we can observe the crystal growth from an observation window, and catch a time period during which the crystal cracked. Also, we can find the cracking from some sensor readings. For example, we can find cracking from weight sensor. However, there will be a time delay from the cracking to the change of crystal weight. The cooling procedure usually takes several days. We can therefore conclude that the simulation results agree with the experiments. The crystals harvested under the two cooling profiles discussed above are shown in Figure 23(a) and (b). These agreements between the model and experiment ensure that the assumed values and characteristics of the critical radial temperature difference are valid. It further verifies that the analytical approaches, and other selected parameters in the model are reasonable. Moreover, the apparent improvement of crystal cracking under the bi-linear cooling profile suggests that a multi-linear cooling profile is ideal.

2.4.3 Optimized Power Ramp-down Profile

The optimized multi-linear power ramp-down profile is shown in Figure 21 (a) along with the crystal surrounding temperature. It is apparent that the power drops at a much faster rate when the surrounding temperature is high and slows down as the surrounding temperature decreases. Such behavior is caused by the significant reduction in the effective thermal conductivity with decreasing temperature (see Figure 17). The calculated radial temperature difference in the crystal during cooling is shown in Figure 21(b) and due to the optimized power ramp-down profile; the values are nearly identical to that of the critical temperature difference. Importantly, from the data in Table 4, it is evident that as the temperature of the crystal decreases, the radial temperature difference also decreases due to the slower cooling rate at the lower temperatures.

Table 4 Important results for the simulation in Figure 21

Time (hour)	T (K)	Power (%)	ΔT (K)
24	1276	11.86	5.70
75	877	3.54	4.72
150	720	2.01	1.04

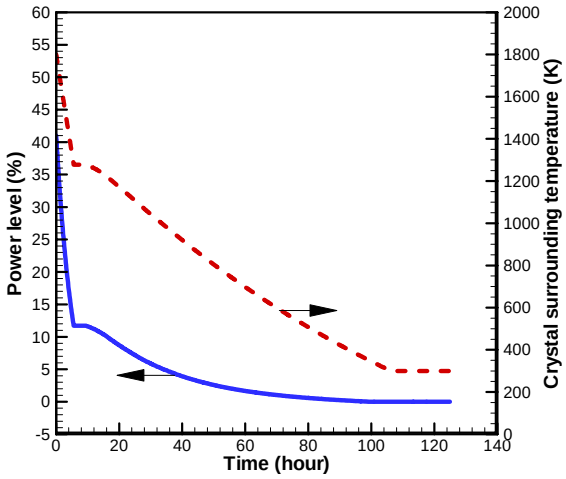

(a)

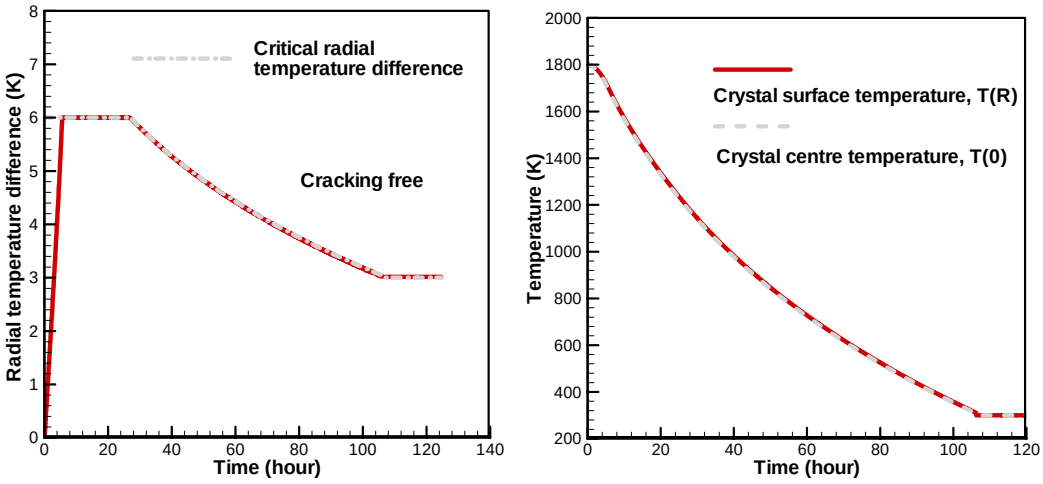

(b) (c)

Figure 21 (a) Optimized power ramp-down profile and surrounding gas temperature change profile, (b) radial temperature difference induced in the crystal, and (c) crystal surface and center temperature profiles

For the purpose of practical furnace programming, a tri-linear power ramp-down profile is preferred over the calculated profile for cooling the crystal. Utilizing the same procedures that produced in Figure 18, an optimized tri-linear ramp-down profile is obtained as shown in Figure 22(a). The crystal surrounding temperature and radial temperature difference are also shown in Figure 22. To satisfy the critical temperature difference constraint, an extended cool down time of 150 hours is required in comparison to that of around 100 hours for the continuous ramp-down profile. At 150 hours, the power level is 2% and the temperature difference is about 1 degree, however, the crystal temperature is still relatively high at 720K. If the power is shut down at this time the crystal cooling rate will be high and a spike will occur in the temperature difference as shown in Figure 22 (b). It has been experimentally observed that the crystals will occasionally crack if the power is turned off at the 150 hour cool down point, making it necessary to wait for a period of time before shutting off the power at the end of the ramp down so that the temperature difference can reach its minimum. In the growth experiment, the power control system can only be adjusted down to within 2.5% of the full power level and the power supply is then turned off. This parameter has also been implemented in the simulation resulting in a spike for the radial temperature difference at power of 2.5% (Figure 22(b)). The crystal surrounding temperature is still rather high at 2.5% in comparison to room temperature, Figure 22(a), when the power is turned off and the surrounding temperature will change to room temperature rapidly through normal thermal dissipation. When it exceeds the critical temperature gradient value, cracks may develop at the end of the cool down, which have been observed.

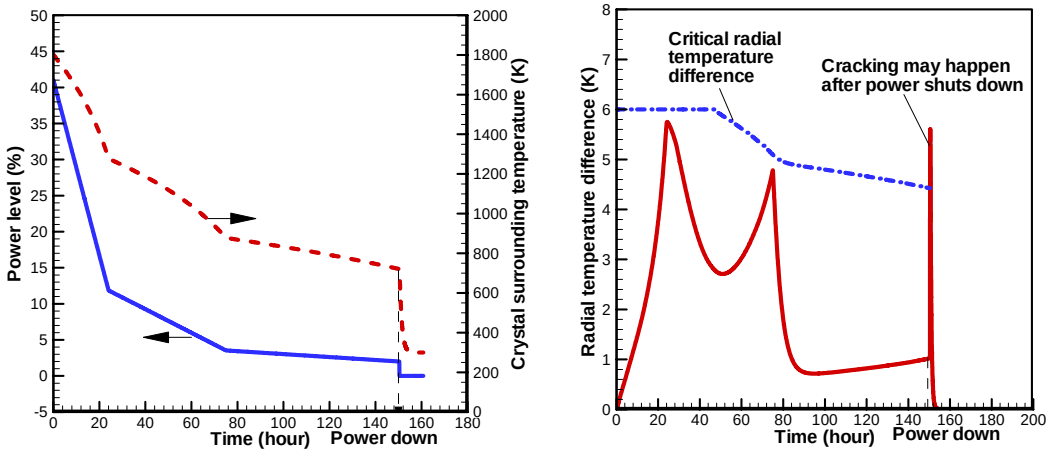

(a) (b)

Figure 22 (a) Tri-linear power ramp-down profile and surrounding gas temperature change profile, and (b) radial temperature difference induced in the crystal

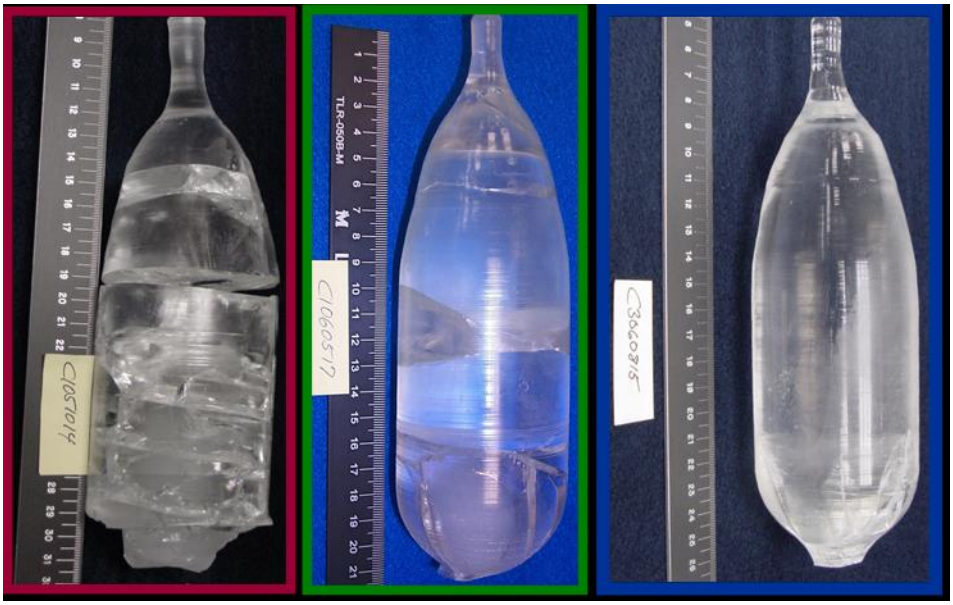

(a) (b) (c)

Figure 23 The grown crystals based on the power ramp-down profiles in (a)Figure 19, (b) Figure 20, and (c) Figure 22.

In conclusion, a tri-linear power ramp-down profile has been utilized to routinely harvest 7.0 cm diameter Yb:S-FAP crystals without cracking in the upper useful portion of the crystal (Figure 23 (c)). The cracking has been significantly reduced in comparison to the boules with alternate cool down profiles as shown in Figure 23 (a-b). Cracks seen at the bottom of the crystal result from a strong thermal perturbation caused by solidification and cracking initiated within the solidified melt. Further study is underway to eliminate this cracking as well.

2.5 Study of Fast Cooling

The successful cooling process for 7.0cm diameter crystal discussed above sections lasts almost one week. Therefore, further studies are conducted to reduce the cooling time. It shows that cracking at the tail portion of the crystal results from strong thermal perturbation, cracking at the middle portion of the crystal is mainly caused by high stresses from radiation heating of crucible Iridium ring, and cracking at the top shoulder is mainly affected by high temperature gradient due to the cold top of the furnace. The cooling crystal could be divided into hot zone and warm zone according temperature distribution in the analysis. Temperature gradients in the crystal can be reduced by redesigning the hot zone. A technique to reduce cooling time by pulling crystal out of the hot zone during cooling, therefore, has been presented and studied numerically.

2.5.1 Analysis of Experiments

Figure 24 shows experiments of large diameter Yb:S-FAP crystals conducted by LLNL. The crystals mainly cracked into two pieces from the middle. The top parts look better than the lower part. The surfaces at cracking position have regular convex and concave shapes. By analyzing the experiments, useful information can be achieved according the cracking positions and patterns.

In experiments, a linear power ramp-down profile was used to achieve 3.5 cm diameter crack-free crystals. Where it was used in the cooling of 7cm diameter crystal, the crystal cracked into many pieces (see Figure 24a) due to massive cracks. It requests slow cooling rate. Cracking was improved (See Figure 24b) by using a bi-linear power ramp-down profile. By further reducing cooling rate with an optimized tri-linear power ramp-down profile, a crystal without cracks in the main body was achieved shown in Figure 24(c). The tri-linear power ramp-down profile was, then, applied to cool a longer crystal. The crystal cracked as shown in Figure 24 (d). By further slow down the 2nd ramp of the cooling profile, cracks were obviously improved (see Figure 24e). Cracks may be minimized by further reducing cooling rate, such as a 4^{th}-linear power ramp-down profile, but the cooling time will increase significantly. For economic consideration, it is not recommended. The cracks should be improved by other methods. This is a goal in this section. During the above

experiments, crystals were attached to the melt during cooling from the experience of 3.5cm diameter crystal cooling. An experiment has been conducted to see what happens if the bottom is detached from the melt during cooling. The achieved crystal is shown in Figure 24 (f). The bottom part was cracked badly.

(a)

(b)

(c)

(d)

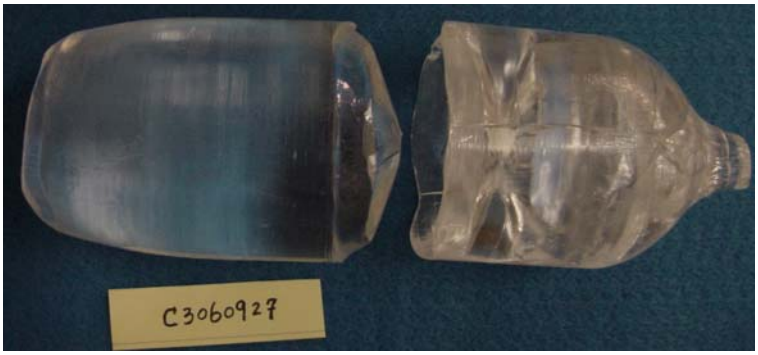

(e)

(f)

Figure 24 Crystals achieved in the experiments conducted by LLNL, (a) short crystal cooled by a linear power ramp-down profile, (b) short crystal cooled by a bi-linear power ramp-down profile, (c) short crystal cooled by an optimized tri-linear power ramp-down profile, (d) long crystal cooled by the optimized tri-linear power ramp-down profile, (e) long crystal cooled by the optimized tri-linear power ramp-down profile with a slow 2nd ramp, and (f) short crystal with bottom unattached to the melt during cooling

2.5.2 Analysis of Cracks

The presented experiments in show Figure 24 that there are three easily-cracked regions in the crystals: bottom(D1), middle(D2) and top(D3) (see Figure 25). The causing factors at these regions are different. During cooling, the furnace top is cold and the crucible is hot. The inductive heating power is reduced slowly accompanied by a reducing temperature of the crucible. The averaged crystal temperature also decreases until room temperature when cooling process is finished. The temperature distribution in the furnace is significant for crystal cracking. Figure 26(a) shows experiment and simulation results when no crystal appears in the furnace. The curvature tells that there exist hot zone and warm zone in the furnace. The zones exist

in the crystal when crystal appears in the furnace since crystal is in heat balance with its environment. The schematic of hot zone and warm zone are shown in Figure 26 (b). Cracks are highly related to the zones distributed in the crystal.

Cracking at the top portion of the crystal including seed broken was observed as Figure 25 shows. The top portion of the crystal is directly affected by the cold furnace top. Heat flux along axial direction from the lower part of the crystal (hot zone) to the top of the crystal (warm zone) is stuck by the small cross area of crystal neck resulting in large thermal stresses and causing it cracking. The actual gas flow in the furnace is not symmetrical. The three-dimensional flow causes an asymmetric temperature distribution especially at the top portion of the crystal, which increases the possibility of cracking. Middle portion cracking is critical since it determines the maximum useful portion of the crystal. There are two mainly causes of the cracks. At the crystal middle part, hot zone changes to warm zones, so the longitudinal temperature gradient is locally large which results in large thermal stresses. The middle portion of the crystal is close to the crucible ring. The crucible absorbs energy from magnetic field and keeps the highest temperature in the system. Radiation heat transfer from the crucible ring to the cooling crystal causes a high temperature gradients zone in the crystal and makes it cracking. The cracks are convex and concave that may result from the fighting of axial and radial temperature gradients. The bottom portion cracking is inevitable due to growth controlling. Fortunately, it does not have significant effects on the useful portion of the crystal. To minimize these cracks, however, is beneficial for growth of high quality crystals. Several issues are related to them. During cooling the bottom of the crystal is attached to the melt. It will cause thermal shock from the solidifying melt to the crystal through the attached section. Also cracking in the melt pool may propagate into the crystal and cause the bottom cracking. In seed broken cases, the bottom portion of the dropped crystals usually crack badly resulting from the impact of the solidified melt. There may be existed of other portion cracks in the cooled crystal. The cracking mechanisms are dependent whether it locates in hot zone or warm zone. In the warm zone, crystal temperature is relatively low, and during cooling axial temperature difference is important. In the hot zone, radial temperature difference, however, is the main factor of cracking.

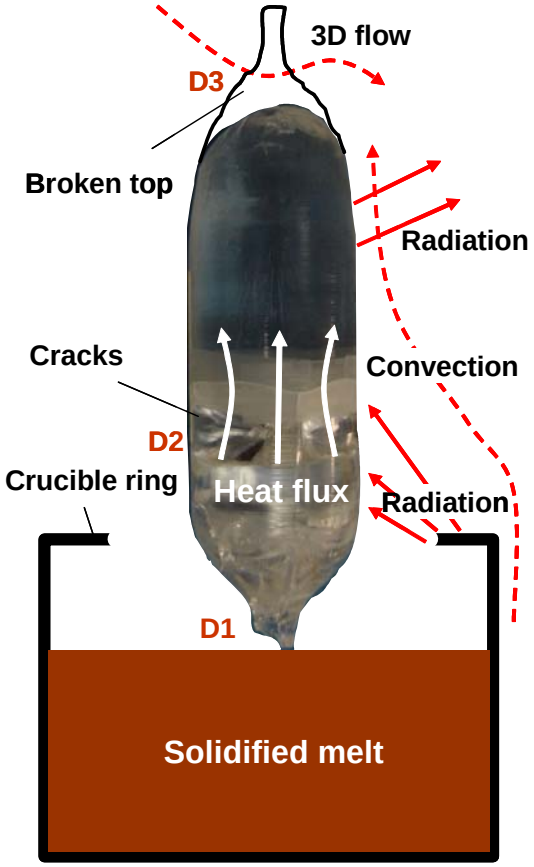

Figure 25 Three easiest cracking regions in the crystal

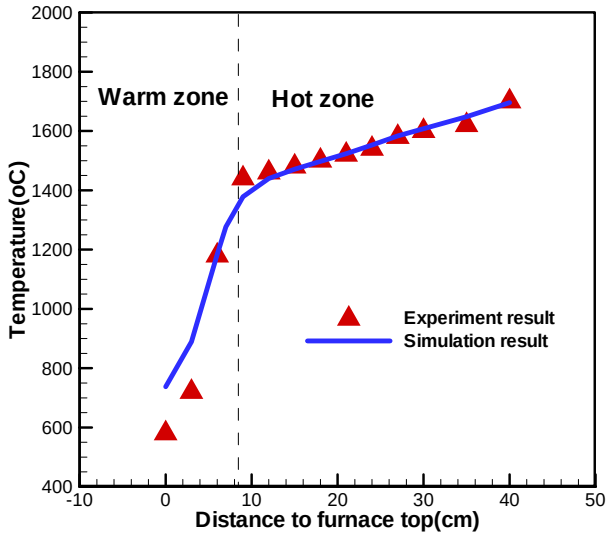

(a)

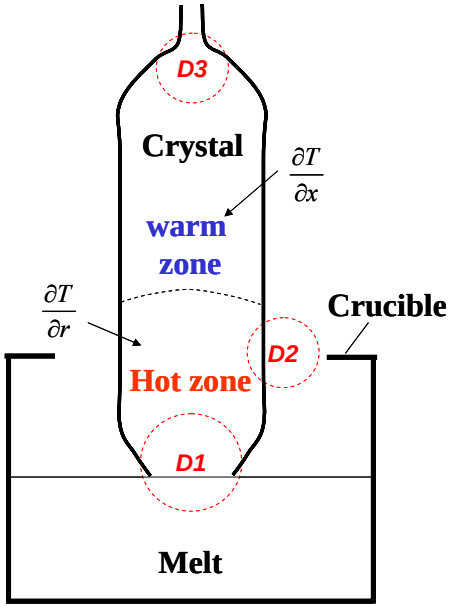

(b)

Figure 26 Hot and warm zones in the cooling crystal by experiment and simulation

In the experiments it has been shown that longer crystal is more difficult than shorter crystal to be cooled safely. The reason can also be related to the distribution of hot zone and warm zone in the crystal. Figure 27 and Figure 28 show the temperature and stream function distribution of shorter and longer crystal, respectively. When crystal is longer, the average temperature of warm zone is lower due to the fact that the top of crystal is closer to the cold furnace top and has lower temperature. The heat flux, therefore, from hot zone to warm zone increases significantly which increases the possibility of cracking at the top portion of the crystal. The flow structures around crystal also are different for longer and shorter crystal. For the short crystal the stream function has not changed much from the beginning to the end of the cooling procedure; the stream function of long crystals, however, has a significant variance, moving from the middle of the crystal to the top, in the cooling procedure. The movement of flow vortex centre results from the change of the heat transfer characteristic which, on the reverse, results in the change of heat transfer in the system. Thus, longer crystal has more unstable temperature distribution and easier to crack during cooling.

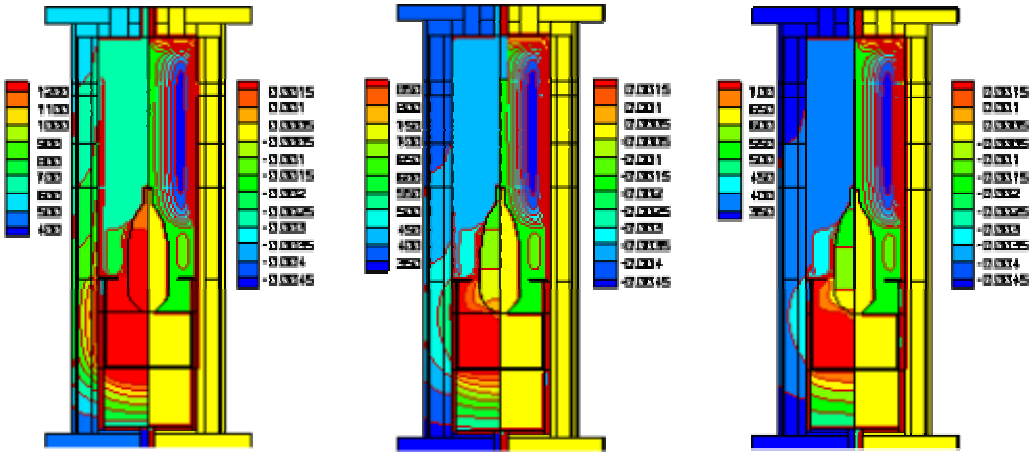

(a) (b) (c)

Figure 27 Stream function and temperature distributions of short crystal at (a) 24 hour, (b) 75 hour, and (c) 150 hour

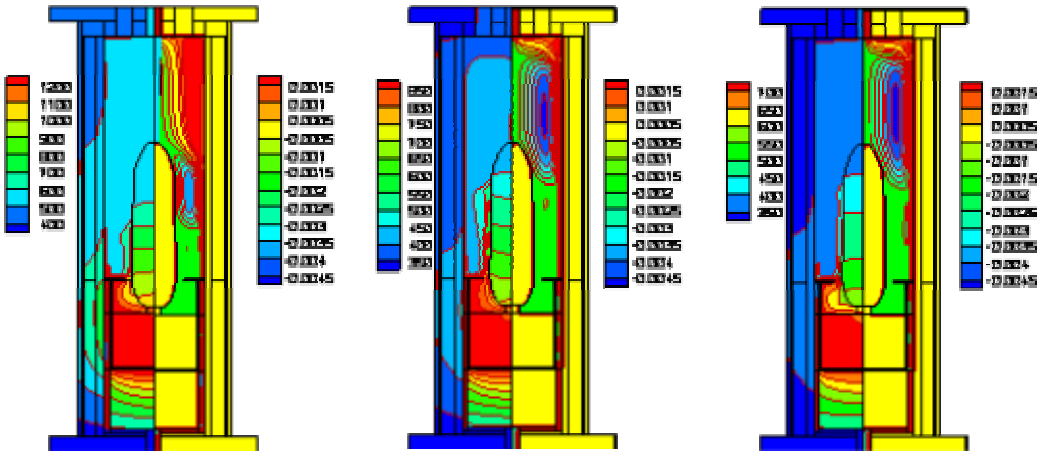

(a) (b) (c)

Figure 28 Stream function and temperature distributions of long crystals at (a) 24 hour, (b) 75 hour, and (c) 150 hour

2.5.3 Methods to Mitigate Cracking

To mitigate crystal cracking two aspects could be conducted. The first is to improve growth furnace, and the second is to improve cooling process. Our efforts are concentrated on mitigate the three regions cracks, especially the middle portion of the crystal.

Top portion cracks are able to improve by increasing insulation of the furnace. It

will increase temperature of the upper portion crystal and reduce longitudinal heat flux in the crystal which will reduce cracks. To avoid seed broken, large seed is recommended so as to increase the cross section area, reduce induced temperature gradients and cracks. To avoid cracks in the middle portion of crystal the most important is to weaken the effects of the crucible ring on the crystal. One way is to reduce the crucible ring temperature, and the other is to redesign the ring. Low RF coil position is a good way to reduce temperature of the crucible ring by heating the ring less. New ring designs are available to minimize the middle cracks (see Figure 29). It will be discussed later. The possible solution for bottom portion cracks is to improve tailing process.

Numerical simulations are conducted to disclose the feasibility of new ring design and new cooling process to mitigate cracks. The gas flow rate from the bottom of the furnace is set to 13.95L/min.

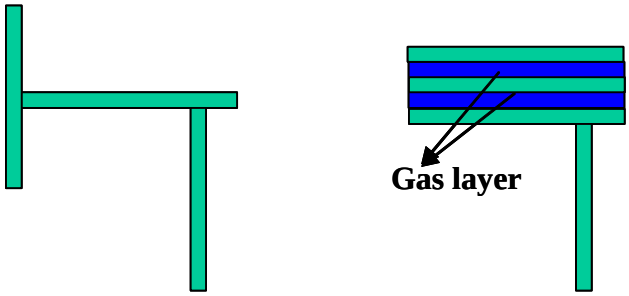

Figure 29 Two kinds of new ring designs to improve cracking

2.5.4 Effects of New Ring Designs

There are several ring designs available as shown in Figure 29. These rings are used to reduce their effects on the crystal middle portion. Their function is to weaken the ring radiation to the crystal by reducing ring temperature or blocking direct heat transfer from ring to crystal. Numerical simulation was conducted to prove effective of a new kind of ring design. This ring design uses a multi-layer ring, between which is filled with gas, which not only reduce the portion of magnetic energy absorbed by the ring, but also make temperature in the ring uniform due to convection. Since gas in the outer side of the ring comes from the cooling bottom of the furnace, its temperature is relatively low. The gas in the ring increases heat transfer of gas surrounding it, so the ring temperature reduces significantly. Figure 30 shows numerical simulation results. In simulation the new ring design is modeled by setting its temperature 100K lower. One can see that the radial temperature gradient in the middle portion of the crystal is much lower when the new ring design is used. It

proves good ring design is important for safe cooling, and is necessary to growth high quality crack-free crystals.

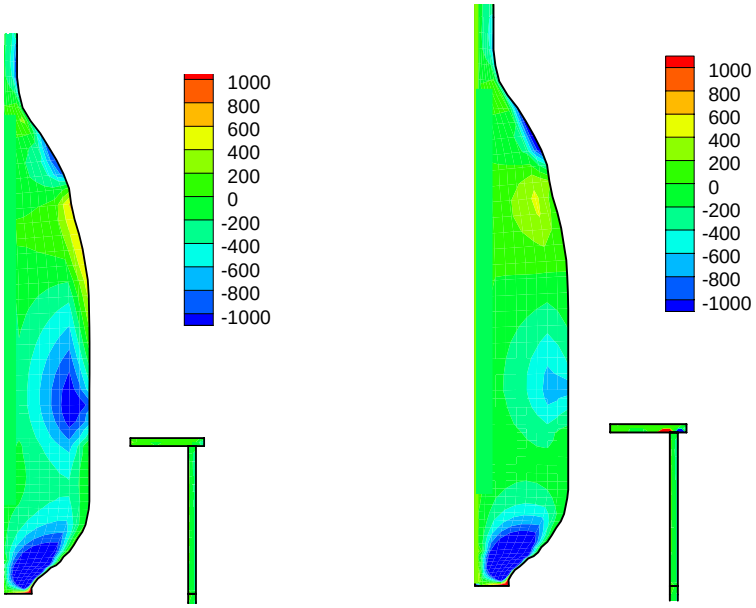

Figure 30 Radial temperature gradient in the crystal, (a) general crucible ring design, and (b) multi-layer new ring design.

2.5.5 A New Cooling Processing

It is well believed that crystal cracking resulting from thermal stresses induced during cooling process. The cooling rate at a location in the crystal is represented by

$$\frac{dT}{dt} = \frac{\partial T}{\partial t} + V\frac{\partial T}{\partial x}. \tag{2.14}$$

Crystal usually cracks when a high temperature difference exists across the crystal due to large $\partial T/\partial x$, or it is suddenly exposed to a cold environment due to large $\partial T/\partial t$. Preventing crystal from cracking requires dT/dt at any location of the crystal smaller than the critical value that means the cooling rate should be slow.

During growth, Eq.(2.14) becomes

$$\frac{dT}{dt} \approx V\frac{\partial T}{\partial x} \tag{2.15}$$

For a steady growth, V is constant. $\partial T/\partial x$ will determine dT/dt and cracking location. During cooling Eq.(2.14) becomes

$$\frac{dT}{dt} \approx \frac{\partial T}{\partial t}. \tag{2.16}$$

To avoid crystal cracking, the first step is to slow cooling rate. But in economic consideration, cooling rate cannot be too slow. A safe cooling process without significant increase of cooling time should be worked out. The Eq.(2.16) is the traditional equation for crystal cooling. If V is not equal to zero, that is, to pull the crystal during cooling procedure at a certain pulling rate, what will happen to the being cooled crystal? Physically the pulling makes the crystal move from hot zone to warm zone. If the whole crystal can be put in the warm zone during cooling, it is expected to mitigate the cracking. Thus, the new idea is to pull the crystal out of hot zone during cooling to minimize cracking and reduce cooling time.

Supposed when crystal is pulled upward to the location up the crucible ring, the system temperature is around 850K due to the fact that crystal usually cracks when its temperature is around 850K. By pulling it into the warm zone, it is absolutely beneficial for the crystal to survive from the dangerous temperature condition. To prove the feasibility of this method, we should examine the temperature distribution and make sure that temperature gradients will not be larger than the attached case. Stream function and temperature distribution of both cases are shown in Figure 31. By comparing the temperature distributions of Figure 31 (a) and (b), one can find that vertical temperature gradient reduces significantly by pulling the crystal out the crucible during cooling as we expect. The reason is that the temperature difference of the top and bottom of the crystal reduces due to pulling the crystal to the warm zone. It is also obvious that the radial temperature gradient reduces significantly since the crystal lies in the surrounding with more uniform temperature. The crucible ring affects the bottom of the crystal now, so the middle portion cracking is able to be avoided and the upper useful portion of crystal can be maximized.

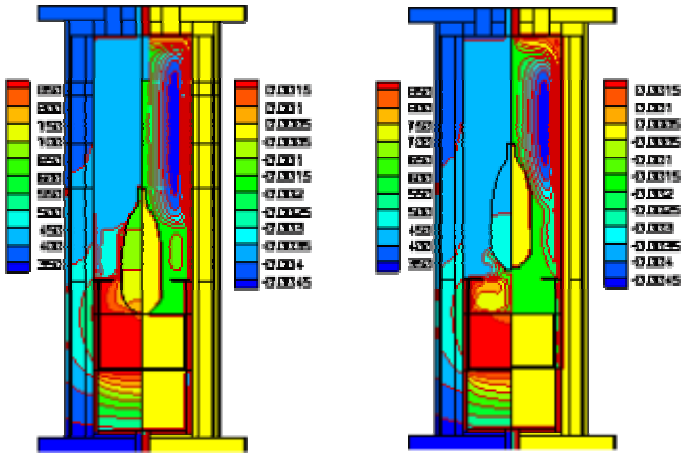

(a) (b)

Figure 31 Stream function and temperature distributions of the crystals after 75 hours cooling, (a) crystal is attached to the melt during cooling, and (b) crystal is pulled out of the crucible during cooling

Figure 32 The grown crystal by the method that pulling crystal out of the crucible ring during cooling

The grown crystal by the method that pulling crystal out of crucible during cooling is shown in Figure 32. Although seed was broken during cooling, the upper portion of the crystal looks still good. By comparing the cracking patterns at the bottom of the crystals with seed broken(See Figure 24d, e, and f) to those without seed broken (See Figure 24b and c), one can see the crystal bottom crack in the Figure 32 is very similar to those with seed broken. So we have the reason to believe that cracks at the bottom of the crystal resulted from the impact when the crystal was dropped to the solidified melt. The solution is to use large seed or to improve seeding procedure.

Chapter 3 Controlling of Melt Inclusion

3.1 Review of Melt Inclusion

Melt inclusion can markedly degrade optical qualities of the crystalline material. In order to improve the crystal quality it is important to understand the mechanism of melt inclusion. Nassau and Broyer [90] and Cockayne et al.[91] discussed this extensively for the Czochralski growth of $CaWO_4$ crystals. They attributed the formation of voids/bubbles to constitutional supercooling combined with the segregation of dopant impurities, gaseous impurities and basic constituents. Further study by Cockayne [92] showed that the predominating factors are the entrapment of an impurity-rich liquid or solute trail. Miyazawa conducted the experimental study of $Pb_5Ge_3O_{11}$ and TeO_2 single crystals grown by the Czochralski method [93] and found that such materials with low melting temperature are apt to entrap the bubbles during growth. They also studied the effects of crystal rotation rate and crystal diameter on the interface shape and found that the entrapment of bubbles in the crystal is related to the interface shape. Recently Nicoara et al. investigated voids engulfment in shaped sapphire crystals and concluded that the void/bubble distribution strongly depends on pulling rate and shaper design [94]. Besides optical and laser crystals, tremendous work has been performed on the generation and entrapment of air bubble in ice formation[71, 72]. It is believed that air rejected by the solidification can be accumulated in front of the interface to a level causing nucleation. However, bubble free ice can be grown in flowing water due to the fact that the flow of water hinders pileup of air in front of the interface. Also, it has been commonly known that last freezing water contains much more bubbles than the first frozen portion. A comprehensive review has been conducted by Wilcox and Kuo[66] and conditions favorable for bubble formation have been identified such as increasing growth rate and ambient gas pressure, decreasing stirring and reducing the height of liquid. They also concluded that surface and solubility are more important parameters in controlling bubble formation and constitutional supercooling and interface breakdown are not necessarily present for bubble formation.

In this chapter, two types of inclusion mechanism are examined, especially, how to prevent species from piling up near the growth interface through controlling the

melt flow. Designs of submerged baffle and heater for Cz growth is proposed. Numerical simulations are performed to examine the effect of crystal rotation on the shape of the growth interface and flow structure of the melt under the crystal, as well as the effects of submerged baffle and heater on melt flow structure and interface shape. Optimal location of submerged baffle and temperature of submerged heater will be determined.

Czochralski growth system with Radio Frequency (RF) Induction heating (see Figure 15) has been widely used for the growth of many optical crystals. An exemplary material being discussed here is Nd^{3+}: $Gd_3Ga_5O_{12}$(Nd^{3+}:GGG) due to its easy availability of properties that can be used in high average power solid-state heat-capacity laser (SSHCL)[95]. Nd^{3+}: $Gd_3Ga_5O_{12}$(Nd^{3+}:GGG) is grown from an excess of Ga_2O_3 in the initial oxide mixture with a rotating seed [96]. An iridium crucible is used to accommodate a high melting temperature. Crystals, in most cases, are grown in an inert environment for preventing the melt components and iridium crucible from oxidation. The Iridium crucible is inductively heated by copper coils with AC current. It is well known that melt inclusion is the major defect affecting optical properties. Melt inclusion is generally related to super-saturation of species either from raw materials or from reactions.

3.2 Mechanisms of Melt Inclusion

Melt inclusion is often present in optical crystal, as seen in Figure 33 of a $LaBr_3$ crystal. The most challenging issue in yielding high-quality optical crystals is at reducing or controlling melt inclusion. To fulfill this goal, it is important to know how the precipitation/bubble forms, grows, and is entrapped in the solid. Two prevailing theories for melt inclusion are discussed here. One is the well-known constitutional supercooling theory, and the other is the solute super-saturation theory that has been used to describe ice formation.

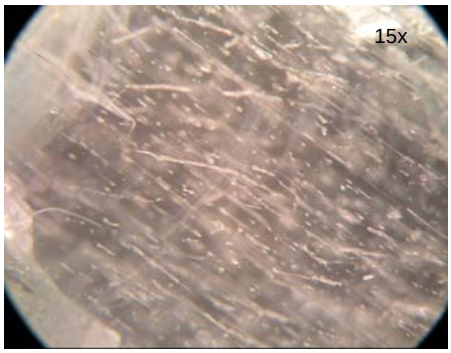

Figure 33 Inclusion in a $LaBr_3$ crystal.

The first theory for melt inclusion mechanism is related to the instability of the growth interface. The instability of the growth interface resulting from constitutional supercooling is widely accepted as the cause of the inclusion in crystal growth society [97-100]. During solidification, solute concentration is piled up in front of the solidification interface due to segregation. The pileup of a solute-rich boundary layer leads to the formation of a constitutionally supercooled region, causing instability of the planar growth front. Solute redistribution by convection was formulated by Burton, Prim, and Slichter [101], and Wagner [102] as well as many others. Papapetrou [103] studied qualitatively how such a solute buildup could make the plane front instable. Morphological stability and its relationship to constitutional supercooling was studied by Tiller et al.[104], and further advanced by Mullins and Sekerka [105].

The general compositional supercooling criterion [106-108] shows that the ratio of temperature gradient on the liquid side to the interface velocity, G_L/v, must be larger than a critical value in order to maintain a stable plane front. Jackson and Hunt [70] confirmed that as the value of G_L/v decreases the interface becomes rippled, and undergoes the transition to cellular. The grooves associated with these boundaries act as built-in distortions of the plane front, and the breakdown of the interface begins, and spreads outward to other portion of the crystal. The first protrusion causes solute to pileup at the roots of the protrusion that further cause recesses to form, subsequently trigger the formation of other protrusions. The grown particles are easy to be entrapped by the broken interface as the interface moves forward.

In summary, the first mechanism considers the melt inclusion resulting from constitutional supercooling and interface breakdown. The formation of the inclusion can thus be suppressed by increasing the temperature gradient in the solid and suppressing the species pileup in front of the solidification interface.

The second mechanism is not related to the interface breakdown. It has been widely used to explain the void formation in ice. The mechanism can be summarized into the following steps. Firstly, solute rejected from the solidified crystal piles up at the growth interface, and precipitates after it reaches super-saturation followed by nucleation. When dissolved gas pressure exceeds a minimum pressure at the rotation axis, nucleation of bubble/particle from dissolved gases may occur [93, 109]. Secondly, the size of bubble/particle increases until reaching the equilibrium when its radius, R, is larger than a critical value, R_{cr}. The value of R_{cr} depends on solute

boundary layer thickness and diffusivity of the solute in the melt. When solute concentration surrounding the bubble/particle is greater, solute will diffuse into the bubble/particle, resulting in an increase of bubble/particle volume. The equilibrium condition can be achieved if the amount of solute diffusing into the bubble/particle equals that diffusing out of it. This might be confirmed from the development of blowholes in the ice, which is proved to be related to steady state solute profile [67]. Thirdly, when the size of bubble/particle exceeds a certain value, inclusion will occur. Fast growth rate and large size of bubbles are favorable for trapping. Small bubbles will be pushed away from the growth interface. The critical size of bubble/particle for entrapping in the solid depends on the surface energies between crystal, melt and particle/bubble. In the experiments, bubble inclusion does not require high cooling rate nor interface breakdown. Lastly, if the amount of solute diffuses into the bubble core, the size of bubble will be enlarged. Surface energies, boundary layer thickness, solubility, and growth rate are the most important controlling parameters. The shape of defects by bubble core formed in Cz-grown Yb:S-FAP crystals can be found in the reference [13] and it looks like 'ice worms' [67].

To summarize, melt inclusion in this mechanism is related to growth rate and solute supersaturation in front of the growth interface. Supercooling and interface breakdown may not be necessary. To reduce inclusion, it requires a slow growth rate or other methods to prevent solute from piling up.

3.3 The Method to Control Melt Inclusion

The aforementioned two melt inclusion mechanisms have the common feature: solute pileup is the prerequisite of inclusion. Since the flow structure determines the solute pileup location, it is possible to suppress/limit the formation of melt inclusion in a certain region in the grown crystal so that the maximum area/volume of bubble-free crystal can be obtained.

Transport phenomena in a Czochralski growth system is shown in Figure 34. Solute distribution, subsequent inclusion is affected by heat and mass transfer in the growth system, which in turns strongly depends on melt convection. Also, melt convection pattern is associated with crystal rotation. Thus the determining factors of inclusion will be the strength of natural convection in the melt and forced convection due to crystal and crucible rotations. It is also believed that inclusion is related to solute boundary layer thickness, pulling rate and the shape of growth interface. As the growth interface becomes convex and pulling rate increases, the amount of inclusion increases.

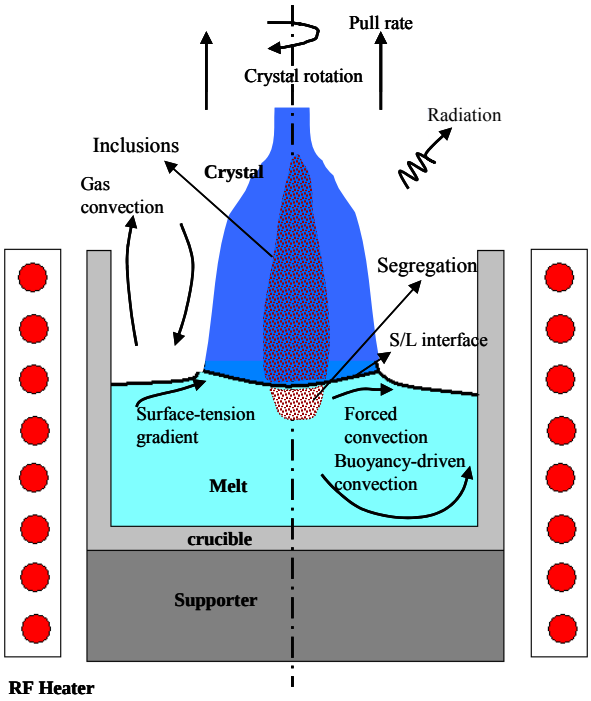

Figure 34 . Transport phenomena and inclusion formation in a Cz growth system.

Figure 35 displays the effects of flow pattern on inclusion formation. When the crystal rotation rate is relatively low and natural convection is strong, the solute rejected from crystal or brought by fluid flow goes down along the axis of rotation and will be piled up near the central part of the melt. As the solute concentration exceeds a critical value, it precipitates around and is trapped in the growth interface to form inclusion due to either the interface instability or surface energy difference. When the crystal rotation rate is increased, the precipitated composition spreads over the growing interface (see Figure 35b). Note that the interface shape is slightly convex compared with Figure 35(a) and this can be attributed to the increase of the rotation rate. Further increase in the rotation rate will cause the interface flat firstly, and then concave [94]. The precipitated composition is easy to be taken away from the interface by increasing the forced convection through crystal rotation. Thus, inclusion-free crystal can be obtained as shown in Figure 35(c). The interface shape and melt inclusion can therefore be controlled through changing the balance of natural and forced convection in the melt.

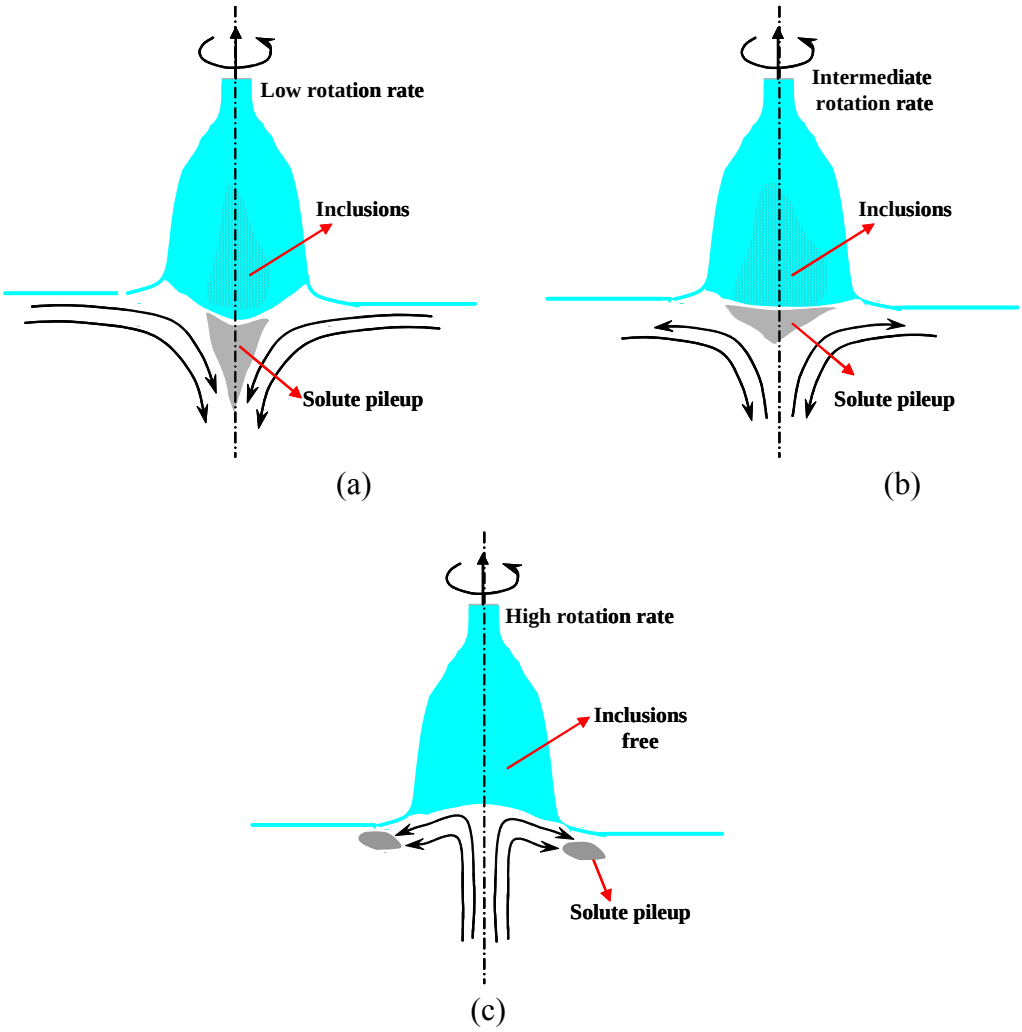

Figure 35 . Effects of crystal rotation on the interface shape (a) large convex interface resulting from a low crystal rotation rate, (b) small convex interface resulting from an intermediate crystal rotation rate, and (c) concave interface resulting from a high crystal rotation rate.

3.4 Mathematical Models

The Czochralski growth system heated by induction heating is simulated. Inductive heating is generated by eddy currents induced in electrically conductive material (e.g., Ir crucible in this study) through applying a time varying magnetic field. Assuming the "gauge condition", $\nabla \cdot \boldsymbol{A} = 0$, and constant magnetic permeability, μ_m, the relationship between the current density and magnetic vector potential, $\boldsymbol{A}$, is expressed as follows [110]

$$\frac{1}{\mu_m}\nabla^2 \boldsymbol{A}_0 = i\omega\sigma_c \boldsymbol{A}_0 - \boldsymbol{J}_0 . \tag{3.1}$$

where $\boldsymbol{A_0}$ is the amplitude of magnetic vector potential ($\boldsymbol{A} = \boldsymbol{A}_0 e^{i\omega t}$), μ_m is the magnetic permeability, ω is the angular frequency of applied AC current, σ_c is the electrical conductivity, and $\boldsymbol{J_0}$ is the amplitude of the AC current that can be calculated from the power input in the coil, $\boldsymbol{P}_i$, via the relation

$$\left|\boldsymbol{J}_0\right| = \left(\frac{P_i}{R_c}\right)^{1/2} \frac{1}{A_c} . \tag{3.2}$$

In Eq. (3.2), R_c is the resistance of the coil and A_c is the cross section area of the coil turn. R_c is calculated from

$$R_c = \frac{2\pi r_c N \rho_c}{A_{eff}}, \tag{3.3}$$

where r_c is the coil radius, N is the number of turns and ρ_c is the electrical resistivity of coil, and A_{eff} is the effective cross section area through which the current flows. The induced power per unit volume is given via

$$q'''_{ed} = \frac{1}{2}\sigma_c \omega^2 \left|\boldsymbol{A}_0\right|^2 . \tag{3.4}$$

To predict the temperature distribution in the entire growth system, a computational domain has been selected to include crystal, crucible and other components that are contained in the cylindrical enclosure. Gases in the system are considered totally transparent, and all the surfaces are assumed to be grey, opaque and diffusive. The grid-to-grid gray-diffusive method is used. The radiation surfaces are divided into rings, each with uniform properties. The rings coincide with the grids used in the temperature calculation. In addition, the view factor between each pair of rings is calculated [111]. The total exchange factor method (total exchange factors between grids) is used to relate temperature to the heat flux or the divergence of the heat flux. The radiation heat flux is calculated by solving the radiative integral equation for grey and diffuse surfaces

$$\frac{q''_{r,i}}{\varepsilon_i} - \sum_{j=1}^{N} F_{ij} \frac{1-\varepsilon_j}{\varepsilon_j} q''_{r,j} = -\sigma_s T_i^4 + \sum_{j=1}^{N} F_{ij} \sigma_s T_j^4 , \tag{3.5}$$

where F_{ij} is the view factor from ring i to ring j, ε_i is the emissivity of the radiative surface, and σ_s is the Stefan-Boltzmann constant. The electromagnetic and energy equations are solved iteratively using an in-house developed code [79].

For simplicity, a two dimensional model is proposed to simulate fluid flow in the melt. Consider that the system is quasi-steady, the melt fluid is Newtonian, and gas and melt flows are laminar. The governing equations in the melt are

$$\frac{\partial \rho_l}{\partial t} + \nabla \cdot \left(\rho_l \boldsymbol{u}\right) = 0 , \tag{3.6}$$

$$\frac{\partial \left(\rho_l \boldsymbol{u}\right)}{\partial t} + \nabla \cdot \left(\rho_l \boldsymbol{u}\boldsymbol{u}\right) = \nabla\left(\mu_l \nabla \cdot \boldsymbol{u}\right) - \nabla p - \rho_0 \boldsymbol{g} \beta_T \left(T - T_{mp}\right), \tag{3.7}$$

where $\boldsymbol{u}$ is the velocity vector, ρ_l and μ_l are the density and viscosity of the melt, respectively, $\boldsymbol{g}$ is the gravitational acceleration vector, β_T is the thermal expansion

coefficient, T is the temperature of the melt, T_{mp} is the melting point temperature, and ρ_0 is the density of melt at melting point. The heat transfer in the entire growth furnace is described as

$$\frac{\partial\left(\rho_i C_{p,i} T\right)}{\partial t} + \nabla \cdot \left(\rho_i C_{p,i} T \boldsymbol{u}\right) = \nabla \cdot \left(k_i \nabla T\right) + q'''_{ed,i} + \nabla \cdot q''_{r,i}, \tag{3.8}$$

where the subscript i indicates melt, crystal, crucible, and other parts of the furnace respectively, and k_i and $C_{p,i}$ represent the thermal conductivity and specific heat of ith domain material respectively, $q'''_{ed,i}$ is the heat source of induction heating that only has a value in the crucible as shown in Eq.(3.4), and $q''_{r,i}$ is radiative heat flux and it is calculated by Eq.(3.5).

Note that the crystal thermal conductivity in Eq.(3.8) is replaced by an effective one. The crystal growth interface is influenced significantly by the internal radiation of the crystal. The Rosseland approximation is used to consider radiation through an effective thermal conductivity,

$$k_{s,eff} = k_s + \frac{16 n^2 \sigma_s T^3}{3 a_R}, \tag{3.9}$$

where k_s is the thermal conductivity of the crystal, k_r is the portion of thermal conductivity from radiation, n is the refractive index of the surrounding gas, σ is the Stefan-Boltzmann constant, and α_R is the Rosseland mean absorption coefficient. The melt is assumed to be opaque to the internal radiation.

The velocity in the melt is obtained by Eqs. (3.6) and (3.7), and its values are set to zero in the rest of domain. The effect of gas convection on heat transfer around the crystal is considered by increasing its thermal conductivity to several times of its original value. Since temperature in the growth system is usually very high, beyond 1500K, radiative heat transfer is dominant. Aforementioned approximation to the convection heat transfer calculation in the crystal surrounding gas will not cause large error. The thermal condition at the melt/solid interface is set through the total heat flux balance as follow,

$$-\boldsymbol{n} \cdot k_s \nabla T\big|_s - q''_{r,in} + \boldsymbol{n} \cdot k_l \nabla T\big|_l = \rho_s \Delta H \boldsymbol{u}_{int} \cdot \boldsymbol{n}, \tag{3.10}$$

where $\boldsymbol{n}$ is the unit vector of normal direction at the interface pointing to the melt, k_s and ρ_s are thermal conductivity and density of the crystal, respectively, ΔH is the latent heat release due to solidification, and $q''_{r,in}$ is the radiative heat loss across the melt/solid interface. $\boldsymbol{u}_{int}$ is the interface velocity, and is defined as $\boldsymbol{u}_{int} = \left[\partial H_1 / \partial t - u_p(t)\right] \boldsymbol{e}_z$, where H_1 is the height of the melt and $u_p(t)$ is the pull rate. In numerical simulation we calculated the solidification rate at the interface and assumed that the triple point, e.g., contact point between meniscus and solidification

interface, is fixed. The speed of the solidification interface at this point will be the pull rate.

At the interface of crucible and crystal where no phase change occur, there exists,

$$-\boldsymbol{n}\cdot k_c \nabla T\big|_c - q''_{r,c} + \boldsymbol{n}\cdot k_{sur}\nabla T\big|_{sur} = 0, \tag{3.11}$$

where $q''_{r,c}$ is the radiative heat loss across the crystal or crucible interface, and the subscript *sur* represents the radiation surrounding for the crystal or crucible.

3.5 Techniques to control Melt Inclusion

3.5.1 The Technique of Flat Submerged Heater

Inductive heating, heat transfer and melt flow in the growth system have been simulated. Melt flow is generated by natural convection induced by temperature difference in the system and crystal rotation. The solidification interface shape critical to the grown crystal is determined by the energy balance at the growth interface considering the latent heat. It is, therefore, important to achieve correct temperature distribution. The in-house built MASTRAPP program [48, 79] has been modified and used to simulate fluid flow field and the solidification interface shape. To obtain accurate result of the magnetic field, it is necessary to select a large simulation zone so that the boundary condition for magnetic solution can be set as the far field. For the study of crystal growth and defects formation, however, one only needs to simulate the growth furnace zone. To improve the efficiency and accuracy of numerical simulation, two sets of grid systems are applied to simulate magnetic field and fluid flow, respectively. An interpolation scheme is used for data transfer between two sets of grid systems. The achieved magnetic field shown on the left in Figure 36 is transferred to the grid system for heat transfer and melt flow calculation, and used as a source term of the energy equation. The obtained temperature field is shown on the right in Figure 36.

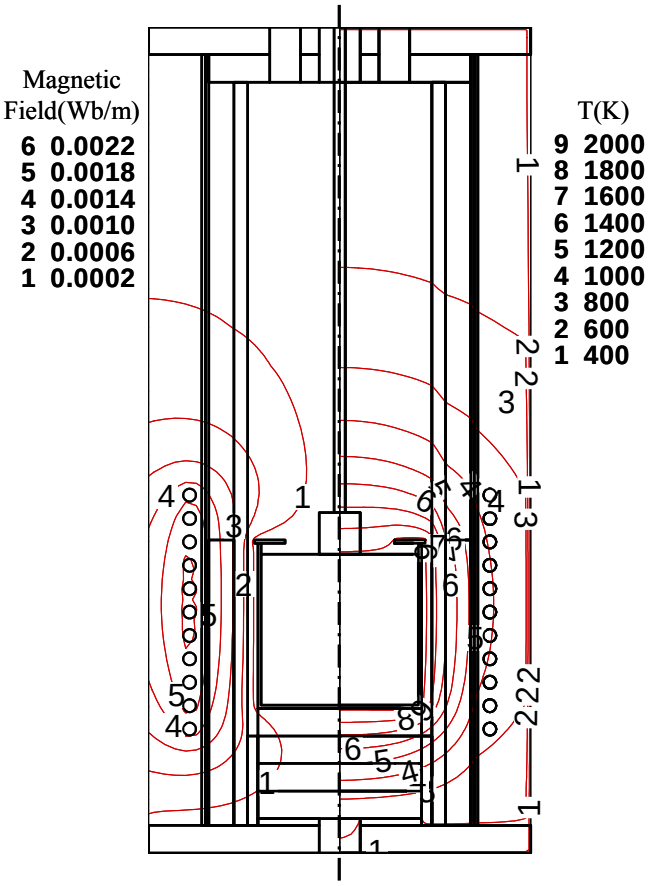

Figure 36 The achieved real part of magnetic vector potential and temperature in the furnace

$Gd_3Ga_5O_{12}$ (GGG) crystal growth is studied to demonstrate the method for the control of melt convection and solidification interface as its properties are available. The properties of GGG crystals are shown in Table 5 [112].

Table 5 Material properties of GGG near melting point

Properties	Value
Density, ρ_s (g/cm^3)	7.2
ρ_l (g/cm^3)	5.7
Heat capacity, C_s (J/g K)	0.586
C_l (J/g K)	0.586
Thermal diffusivity, α_s (m^2/s)	4.7×10^{-6}
α_l (m^2/s)	1.5×10^{-6}
Thermal conductivity, k_s (W/mK)	20.0

k_l (W/mK)	5.0
Emissivity, ε_s	0.3
ε_l	0.3
Thermal expansion coefficient, β_l	2.7×10^{-5}
Latent heat, L (J/kg)	455
Viscosity, μ (kg/ms)	4.0×10^{-2}
Melt temperature, T_m (K)	2023K

Figure 37 shows the simulation results corresponding to crystal rotation from 40 to 70 rpm. It can be seen that the interface shape changes from convex at the low rotation rate (<50 rpm) to concave at the high rotation rate (>60 rpm). When the rotation rate is about 50 ~ 60 rpm, the interface shape is almost flat. In terms of the proposed melt inclusion mechanism, inclusion-free crystal may be obtained when crystal rotation rate is larger than 50rpm. To explain the influence of crystal rotation on melt inclusion, the quantitative relationships of Gr/Re^2, h/R and R_s/R are discussed in the following. The expressions of Gr and Re numbers are given as

$$Gr = \frac{g\beta_T \triangle T D_c^3}{v_l^2}, \text{ and } \quad Re = \frac{\rho_l w_{cr} R^2}{\mu_l},$$

where D_c is the crucible diameter which is the same as the crucible height in this study, v_l is the dynamic viscosity, w_{cr} is the crystal rotation rate, and R is the crystal radius. Two length scales characterizing the interface shape, h, and the forced melt convection regime, R_s, are shown in Figure 38. It should be noted that a small h indicates a less curved interface; and large R_s corresponds to high forced convection intensity. When maintaining Gr constant while changing Re via w_{cr}, the simulation results in Figure 39 reveal that h/R increases with Gr/Re^2; and R_s/R decreases with Gr/Re^2. When forced convection is increased (corresponding to the increase in R_s/R), Gr/Re^2 is reduced, so does h/R. Thus the interface shape changes from convex to flat by increasing forced convection through rotating the crystal.

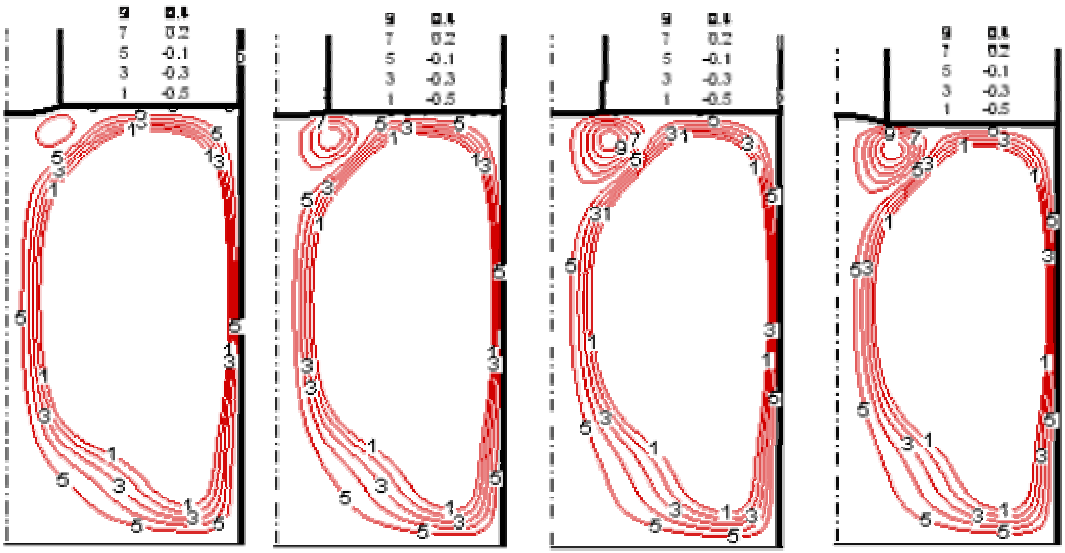

(a) (b) (c) (d)

Figure 37 Stream function distributions in the melt with crystal rotation rates of (a) 40 rpm, (b) 50 rpm, (c) 60 rpm, and (d) 70 rpm, respectively.

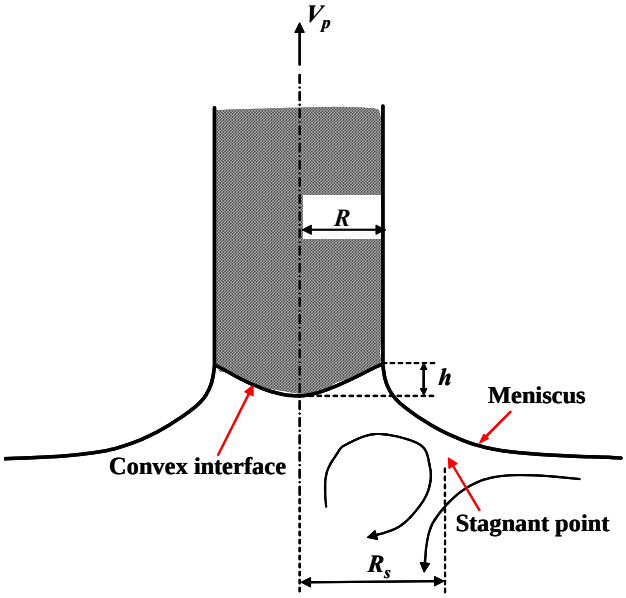

Figure 38 Schematic of melt flow and solidification interface shape.

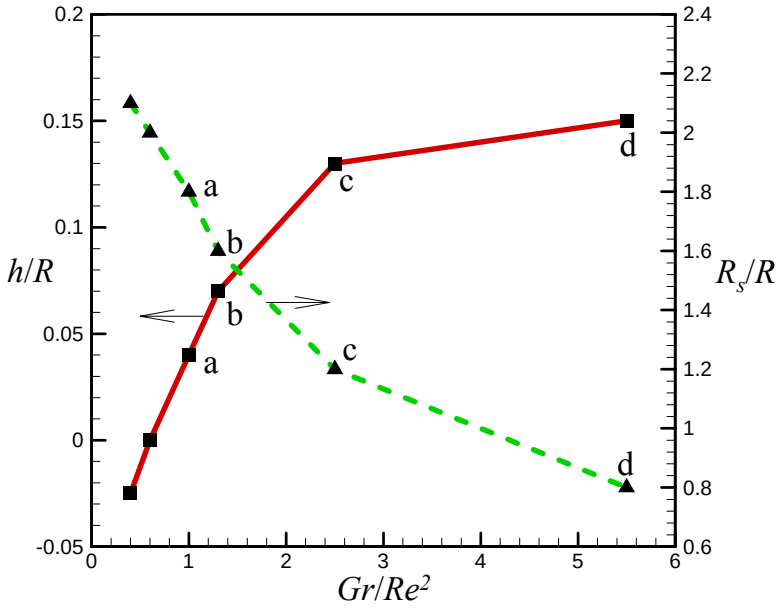

Figure 39 Effect of crystal rotation rate on stagnation point location and the interface shape.

In the growth experiments, increasing rotation rate to a high level may induce other defects. To avoid other defects, we have, therefore, proposed to repartition melt flow zone by placing an Iridium disk in the melt with the support of either three legs or three horizontal pins to center the disk (see Figure 40). The melt in the top portion of the crucible can still communicate the bottom half through the gap between disk and crucible. It is also feasible to add some holes in the disk to allow communication between the top and bottom melt. The effect of new partition on thermal and fluid transport during growth has been simulated and shown in Figure 41. In simulation, a crystal rotation rate of 50 rpm is applied to capture the interface shape transition from convex to flat, and then to concave. It can be seen that the forced convection from crystal rotation is much stronger after adding the disk. The distance between the disk and free surface, H, is an important parameter that controls natural convection strength of the melt near the solidification front. Reducing H will strength forced convection. This proves the effectiveness of repartitioning melt zone to control flow structure in the melt, ultimately to minimize inclusion or control inclusion distribution. The quantitative relationships among Gr_H/Re^2, h/R and R_s/R are shown in Figure 42. Gr_H is defined as $Gr_H = g\beta\Delta T H^3\rho^2/\mu^2$ and H is the depth of disk in the crucible. Results show that h/R increases with Gr_H/Re^2, and R_s/R decreases with Gr_H/Re^2.

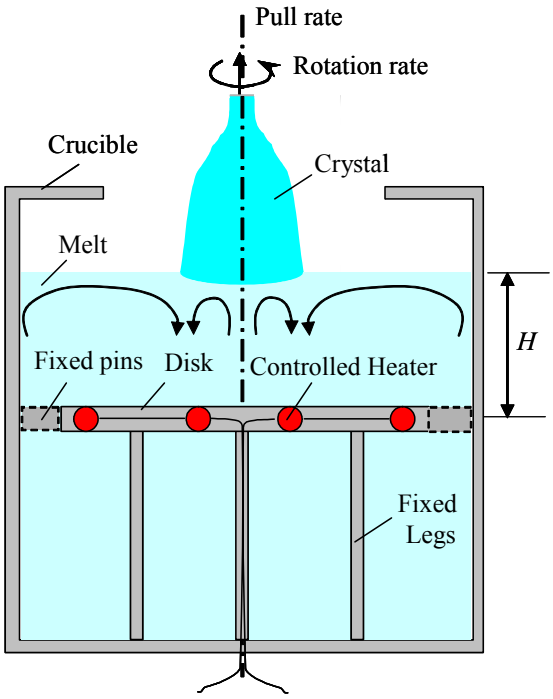

Figure 40 The proposed design to control melt flow structure in the growth system. A disk is inserted into the melt and its distance to the melt free surface is *H*.

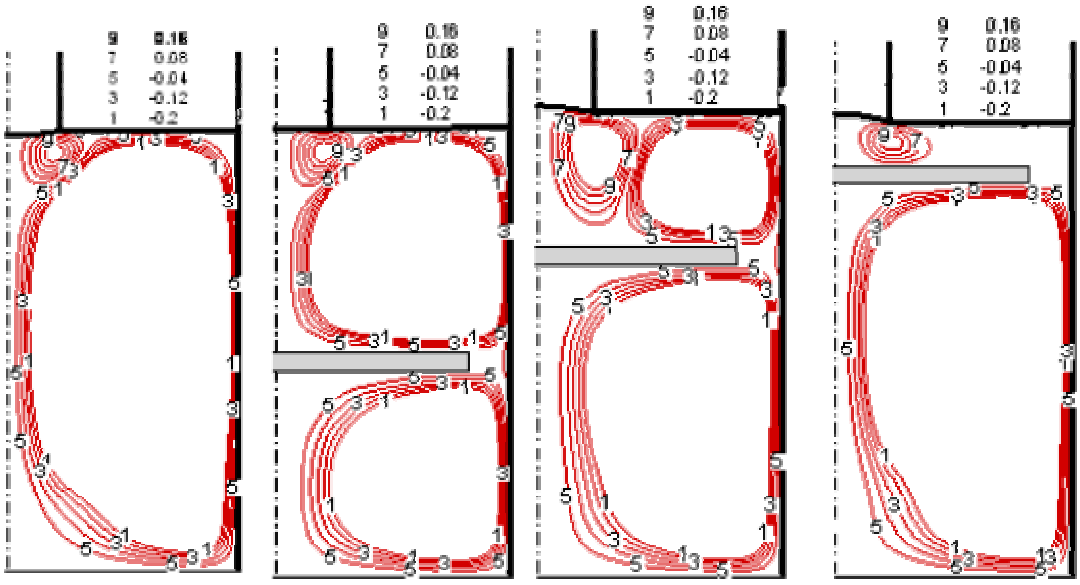

(a) (b) (c) (d)

Figure 41 Streamlines at the crystal rotation rate of 50rpm with (a) no disk, H/D_c=1, (b) H/D_c=0.5, (c) H/D_c=0.3, and (d) H/D_c=0.125.

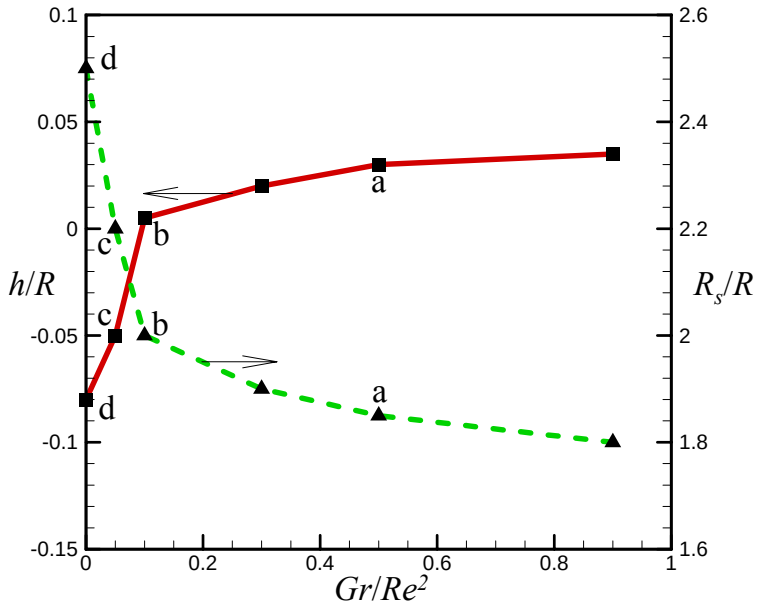

Figure 42 Effects of adding disk on meniscus fluid structure and interface shape.

The disk introduced in the growth system acts as a submerged baffle. Simulation results in Figure 41 are obtained by neglecting direct RF heating to the disk. It should be noted that the baffle is usually made of the same material as crucible. The disk will be heated by RF induction heater which will further modify the melt flow structure. Melt flow could be improved by controlling temperature in the submerged baffle [113, 114]. The effect of controlled baffle temperature on melt flow structure is simulated for the baffle location H/D_c=0.3. The streamlines corresponding to the dimensionless disk temperature, $\theta = (T - T_m)/(T_w - T_m)$, of 0.0, 0.2, 0.4, 0.6, 0.8, and 1.0 are shown in Figure 43(a) to (f), respectively. T_m is the melting point temperature, and T_w is the highest crucible temperature. One may expect to see the weakest natural convection when the non-dimensional temperature is 0.0, but the simulation results reveal that when the non-dimensional temperature is in the range between 0.4 and 0.6, the forced convection below the crystal is stronger than the natural convection. This phenomenon is explained with the assistance of Figure 44. For the given constant T_m and T_w, free surface temperature, T_f, will change with the disk temperature, T_d. The temperature difference between the melting point and disk, ΔT_1 ($=T_d - T_m$), increases with T_d, however, the temperature difference between the crucible wall and disk, ΔT_3 ($=T_w - T_d$), decreases as T_d increases. Both ΔT_1 and ΔT_3 are the predominant temperature differences for natural convection. It is expected the strongest natural convection is present either ΔT_1 or ΔT_3 is larger, equivalent to either $T_d = T_w$ or $T_d = T_m$. Natural convection will be relatively weaker when the disk temperature is set to between the melt temperature and the crucible temperature. One also can see in Figure 43(f) that when the dimensionless disk temperature is set to 1.0 that means the disk temperature the same as the crucible, although the vortex in the melt above the disk is large due to natural convection caused by the hot disk, the convection under the crystal is the weakest. Conclusively, in order to control the melt flow structure, it

is preferable to have the disk temperature set in between the melt and crucible temperature. The interface shape is related to the strength of the convection under crystal. When the dimensionless disk temperature is set between 0.4 and 0.6, the interface looks more concave. It will become flat when the disk temperature is set as the same as the crucible temperature. Note that this conclusion may be changed if the ratio of the crystal diameter to the crucible diameter increases. When crystal covers the most of the top surface, the disk temperature should be as close to the melt temperature as possible, this situation will be similar to the submerged heater used in the Bridgman growth system [113, 114].

The above analysis reveals that disk temperature is important for flow control. As shown in Figure 40, the disk temperature is possible to be set to a requested profile through controlling the heater. Figure 45 shows two kinds of sceneries with disk temperature linearly change in the radial direction. In Figure 45 (a), the centre of the disk (point A) is set to a high temperature θ=1, and the edge of the disk (point B) is set to a low temperature θ = 0; while in Figure 45 (b), the disk temperature distribution is set reversely. One can see that their flow structure is totally different. The interface shape in Figure 45(b) is more concave, which is favorable for melt inclusion control. This study concludes that the disk temperature distribution is another important control factor. It is possible to achieve an optimized disk temperature distribution to minimize or control melt inclusion more efficiently than the temperature setup in Figure 45(b). This could be achieved through iterative simulation and experiments.

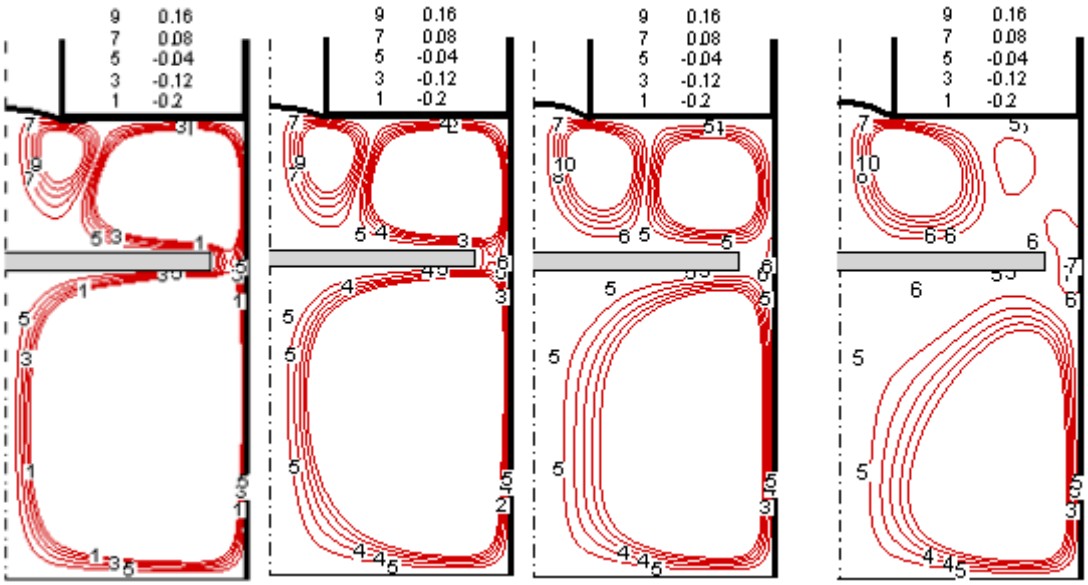

(a) **(b)** **(c)** **(d)**

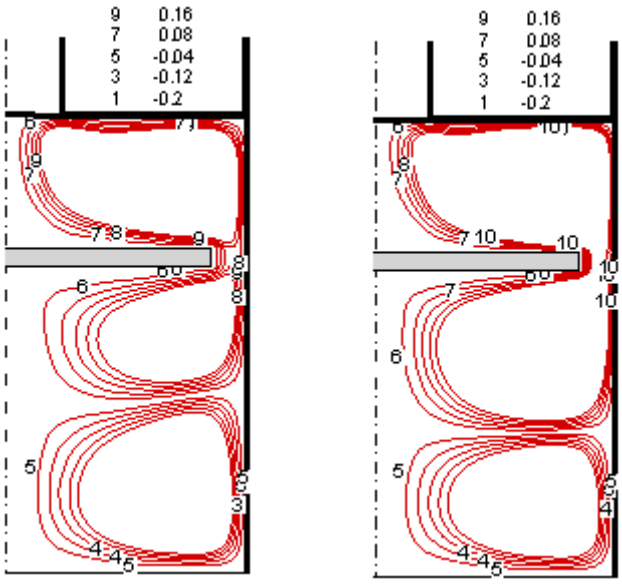

(e) **(f)**

Figure 43 Streamlines at the crystal rotation rate of 50rpm with different disk temperatures, (a) θ = 0.0, (b) θ = 0.2, (c) θ = 0.4, (d) θ = 0.6, (e) θ = 0.8, and (f) θ = 1.0, respectively.

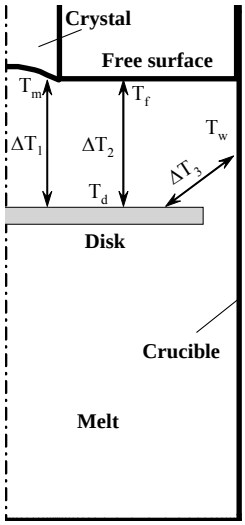

Figure 44 An explanatory schematic to the simulation results.

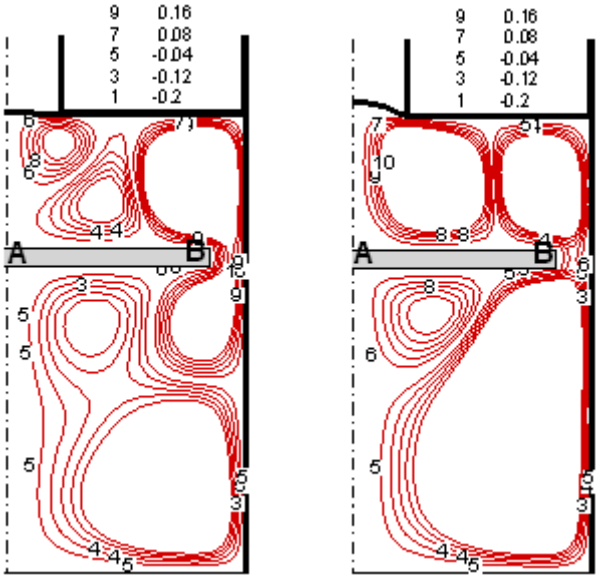

(a) **(b)**

Figure 45 Streamlines at the crystal rotation rate of 50rpm with a linear temperature distribution on the disk, (a) θ_A = 0.8, θ_B = 0.2, and (b) θ_A = 0.2, θ_B = 0.8.

3.5.2 The Technique of Curvature Submerged Heater

Curvature submerged heater is an improvement from flat submerged heater. Figure 46 shows the results when the submerged heater shape of $y = -0.5r^2$ is applied. The interface shape is closer to flat when the heater temperature is set to 0.0 (melt temperature). This phenomenon can be explained that in the present shape of submerged heater, ΔT_1 is more important than ΔT_2. When the heater temperature is set to 0.0, ΔT_1 is minimized so that the natural convection under the crystal is minimized. The relatively strong forced convection is benefit to achieve flat interface shape. Figure 47 shows results when forced convection of crystal rotation is relatively strongest when the submerged heater with the shape of $y = -r^2$ and temperature set to 0.4. So the interface shape looks flatter when heater temperature set to 0.4. Figure 48 shows another disk shape. The disk curve equation is $y = 0.15r^2$, and it is slightly convex compared to others. When the disk temperature varies from 0.0 to 0.4, the interface shape changes from concave to flat, and then to convex. So melt temperature of the disk is favorable for inclusion control.

From above analysis, we can know that the shape of submerged heater is very important. It affects the temperature set in the heater to achieve optimized condition

for melt inclusion minimization. It also shows the difficulty to get an optimized submerged heater design only by simulation. Combined with experimental practice and numerical simulation, the optimized submerged heater shape and temperature setup of the heater could be achieved.

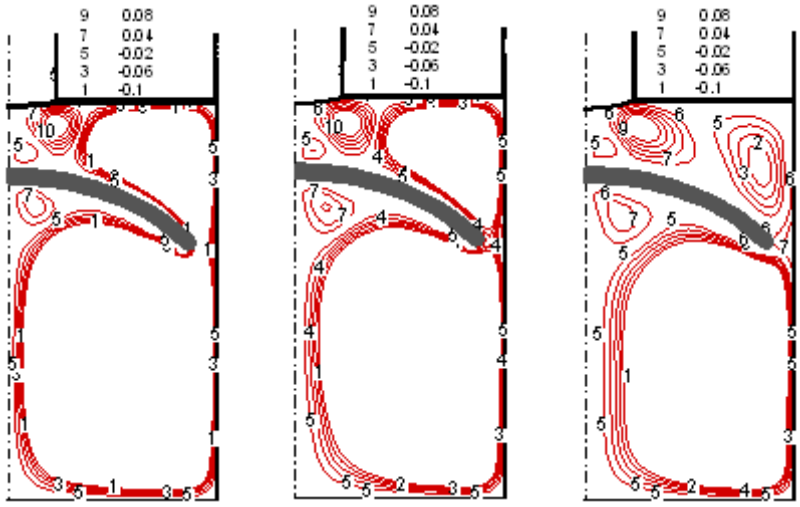

(a) **(b)** **(c)**

Figure 46 Stream function when y = - 0.5r^2 submerged heater is used with temperature set to (a) θ = 0.0, (b) θ = 0.2, and (c) θ = 0.4

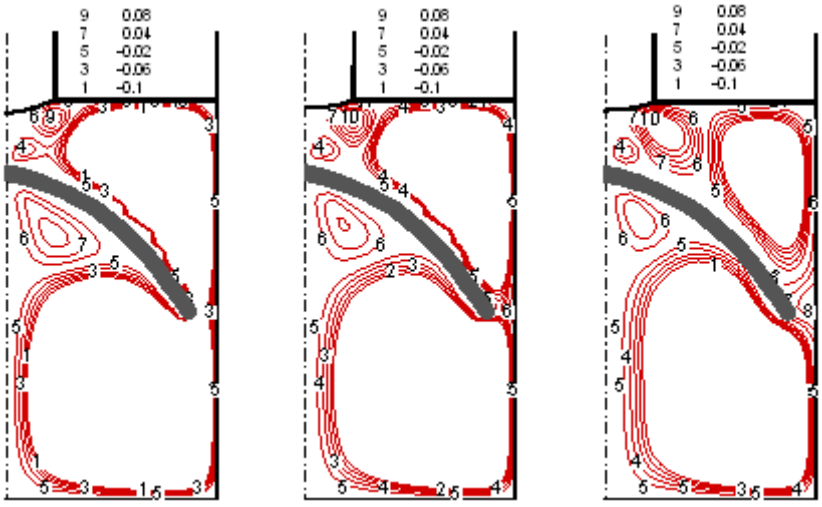

(a) **(b)** **(c)**

Figure 47 Stream function when y = - r^2 submerged heater is used with temperature set to (a) θ = 0.0, (b) θ = 0.2, and (c) θ = 0.4

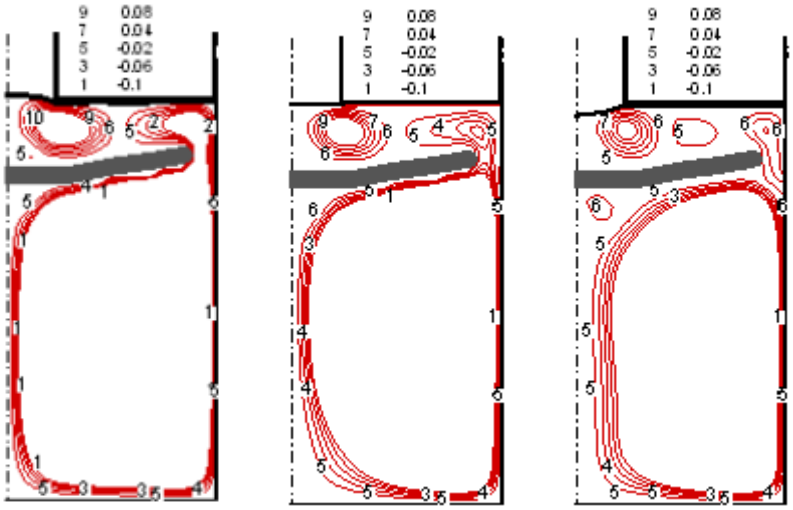

(a) **(b)** **(c)**

Figure 48 Stream function when y = 0.15r^2 submerged heater is used with temperature set to (a) θ = 0.0, (b) θ = 0.2, and (c) θ = 0.4

Chapter 4 Smoothed Particle Hydrodynamics Method

4.1 An Introduction to Smoothed Particle Hydrodynamics Method

4.1.1 Applications of SPH on free surface problems

Smoothed particle hydrodynamics (SPH) method is one of the meshless Lagrangian methods, and it has been widely used to simulate free surface problems [115-118]. In this method, continuum medium is represented by a discrete set of particles each with a given mass and velocity, and macroscopic field equations are represented by particle dynamics. The SPH method is suited for the problems involving free surface and large deformation system. Recently, the SPH method has been used in the solidification problems [119, 120].

Spreading and solidification of molten droplets are the key processes in thermal spray coating, soldering, inkjet, and many other materials processing. When it impacts a cold substrate, a molten droplet spreads in the radial direction and rapid solidification of the melt near the substrate occurs as the result of high cooling rate. An interface tracking scheme is usually required to obtain an accurate position and moving speed of the solidification interface. Most numerical simulations are performed based on the meshed methods, such as the front tracking [121, 122], deformable finite element method [123, 124], volume of fluid [125-128], level set method [129] or combined methods [130-133]. In the meshed methods, the Navier-Stokes equations are solved based on a fixed or adaptive grid system. Two methods have shown great potential to avoid the complication arising from large deformation and splashing: one is the particle level set method [130, 131, 134] and the other is the SPH method [119, 120]. SPH method was firstly employed to study droplet spreading and solidification by Zhang et al [119, 120]. However, some issues were not resolved such as compressibility of the droplet, numerical instability, and accuracy of the surface tension treatment. Traditional SPH method solves the equation of state for local pressure. The accumulation of SPH particles near the impact location

is one of the major issues in the SPH method since it will cause numerical instability. Further, the penetration of SPH particles into the solid phase can happen if a large time step is used. To avoid the time step restriction induced by acoustic waves in the equation of state, the moving-particle semi-implicit (MPS) method is introduced by solving the global Poisson pressure equation [135]. However, such method inherits high computational cost. It is, therefore, necessary for a compromised method that offers a fast calculation with a large time step, as well as stable numerical scheme.

In this Chapter, a new pressure-correction equation will be developed together with different smoothing functions to improve the solution to the equation of state. This method will improve the stability of numerical solution. Also, advanced surface tension and solidification models are proposed and incorporated into an in-house built code. Using the improved SPH method, droplet contraction problem will be solved first to show improvement of numerical instability. Droplet spreading and solidification with high impact Reynolds number are simulated using the improved SPH model. The results are compared with the analytical solution to demonstrate efficiency and accuracy of the current method in handling the problems with free surface and solidification.

4.1.2 SPH Governing Equations

The density of the particles is usually evaluated by using the summation density,

$$\rho_i\left(\vec{x}_i\right)=\sum_{j=1}^{N} m_j W_{ij}\ , \tag{4.1}$$

where $W_{ij}=W\left(\vec{x}_{ij},h\right)$ is the smoothing function, and $\vec{x}_{ij}=\vec{x}_i-\vec{x}_j$, m_j denotes the mass of particle j, h represents the smoothing length and $\vec{x}_i$ is the position of particle i. The summation density has the property of mass conservation. In CSPH, the density is further normalized,

$$\rho_i\left(\vec{x}\right)=\sum_{j=1}^{N} m_j W_{ij} \Big/ \sum_{j=1}^{N}\frac{m_j}{\rho_j} W_{ij}\ . \tag{4.2}$$

The term, $\sum_{j=1}^{N}\frac{m_j}{\rho_j}W_{ij}$, should be equal to unit, but in numerical simulation, it is usually not the case. This will cause unreasonable forces acting on free surface. Corrected SPH (CSPH) is applied to avoid physically un-reasonable results such as

lower density at free surface and solidification interface due to the insufficient SPH particles present in local.

By applying the SPH particle approximation to the Lagrangian form of the Navier-Stokes equations, a symmetric form of momentum equation can be written as follows

$$\frac{D\vec{v}_i}{Dt} = -\sum_{j=1}^{N} m_j \left(\frac{p_i}{\rho_i^2} + \frac{p_j}{\rho_j^2} \right) \nabla_i W_{ij} + \sum_{j=1}^{N} m_j \left(\frac{\tau_i}{\rho_i^2} + \frac{\tau_j}{\rho_j^2} \right) \cdot \nabla_i W_{ij} + \vec{g} + \vec{f}_s , \tag{4.3}$$

where $\vec{v}_i$ is the velocity of particle *i*, *p* is the pressure of particle, $\vec{g}$ is the gravity force, and $\vec{f}_s$ is surface tension force acting on free surface. The calculation of surface tension will be discussed in the later section. The particle approximation for the viscous stress tensor, τ, is

$$\tau_i = -\sum_{j=1}^{N} \frac{m_j}{\rho_j} \mu_i \vec{v}_{ij} \nabla_i W_{ij} - \sum_{j=1}^{N} \frac{m_j}{\rho_j} \mu_i \left(\nabla_i W_{ij} \right) \vec{v}_{ij} + \left(\frac{2}{3} \sum_{j=1}^{N} \frac{m_j}{\rho_j} \mu_i \vec{v}_{ij} \cdot \nabla_i W_{ij} \right) I . \tag{4.4}$$

To improve the particle distribution during the movement in SPH, XSPH is generally used and the particle velocity can be modified as

$$\frac{d\overrightarrow{x_i}}{dt} = \vec{v}_{ip} = \overrightarrow{v_i} - \varepsilon \sum_j \frac{m_j}{\rho_j} \overrightarrow{v_{ij}} W_{ij} \tag{4.5}$$

where ε is a constant and 0.3 is usually used. The XSPH makes the particle distribution more orderly by averaging its velocity with adjacent particles and stability of simulation is usually improved.

In order to describe the incompressible flow, it is necessary to use an artificial state equation to close the equation system. Based on the idea that a theoretically incompressible flow is practically compressible, Morris introduced the artificial compressibility equation:

$$p = c^2 \rho \tag{4.6}$$

where c is the sound speed. The sound speed is generally chosen according to the following rules:

$$c^2 \sim \frac{V_0^2}{\delta}, \frac{\nu V_0}{L_0 \delta}, \frac{F L_0}{\delta} \tag{4.7}$$

where $\delta = \Delta\rho / \rho_0$, V_0 and L_0 are the reference velocity and length, respectively. Since the pressure force is related to the gradient of the pressure, some researchers use the following form of the equation of state,

$$P = c^2 (\rho - \rho_0) . \tag{4.8}$$

where ρ_o represents the target density of the fluid. This equation of state allows us to

control the spatial density distribution. However, the equation of state based SPH method in general suffers the accumulation of pressure field locally and numerical instability may be resulted, especially for the problems with volume contraction.

4.1.3 Smoothing Kernels

Smoothing kernels are very important for numerical stability and accuracy. The Cubic Spline function [136] is, so far, the most widely used smoothing function. It takes the following form,

$$W(R,h) = a_d \begin{cases} \frac{2}{3} - q^2 + \frac{1}{2}q^3 & 0 \le q < 1 \\ \frac{2}{3} - q^2 + \frac{1}{2} & 1 \le q < 2 \end{cases}, \tag{4.9}$$

where q is the ratio of distance of two particles and smoothing length. The same kernel is usually used in all terms in the governing equations. However, when it is applied to the pressure force for high speed impact, it may cause the reduction of pressure force when two SPH particles move closer to each other. To avoid this problem, Johnson et al [137] developed a quadratic smoothing function as shown in Eq. (4.10) to simulate high speed impact problem,

$$W(R,h) = \alpha_d \left(\frac{3}{16}q^2 - \frac{3}{4}q + \frac{3}{4} \right) \quad 0 \le q \le 2 . \tag{4.10}$$

This kernel is useful for the pressure force calculation only since its derivative always increases as the particles move closer, the repulsive force will avoid particles to cluster under high pressure.

To further improve SPH method, different kernels can be employed for different terms. It is similar to employ different differential schemes for diffusion and convection terms in finite difference methods. Müller et al [138] designed the following kernels

$$W_{poly6}(\vec{r},h) = a_d \begin{cases} \left(1 - q^2\right)^3 & 0 \le q \le 1 \\ 0 & q > 1 \end{cases}. \tag{4.11}$$

They employ this kernel everywhere except in the calculation of pressure and viscosity forces. To calculate the pressure force, the spiky kernel of Desbrun is employed,

$$W_{spiky}(\vec{r},h) = a_d \begin{cases} (1-q)^3 & 0 \le q \le 1 \\ 0 & q > 1 \end{cases} . \tag{4.12}$$

The kernel in Eq. (4.12) has the same advantage as the kernel in Eq. (4.10). They designed the third kernel

$$W_{viscosity}(\vec{r},h) = \frac{15}{2\pi h^3} \begin{cases} -\frac{q^3}{2} + q^2 + \text{q-1} & 0 \le q \le 1 \\ 0 & q > 1 \end{cases} \tag{4.13}$$

with the positive Laplacian everywhere and with the following additional properties

$$\begin{aligned} &\nabla^2 W(\vec{r},h) = a_d (1-q) \\ &W(|r| = h, h) = 0 \\ &\nabla W(|r| = h, h) = 0 \end{aligned} . \tag{4.14}$$

This kernel avoids negative Laplacian when two particles move closer. Using this kernel to calculate viscosity terms will significantly increase the stability of simulation. Three kernels from Eq. (4.11) to (4.13) provide good results according to their papers [138].

4.2 Improvements of Traditional SPH Method

4.2.1 Pressure Correction Equation

The equation of state in Eq. (4.6) or (4.8) will lead to very stiff systems when it is used to solve incompressible flow. In general, a low speed of sound is employed and this implementation causes non-conservation of total volume and inaccuracy in the pressure prediction. Also, the deviation of particle density from the reference density will generate spatial distribution of pressure force in Eq. (4.3), resulting in numerical instability, especially in the case of contraction. To resolve the problems arising from the use of the equation of state, one can, instead, solve a global Poisson equation for the pressure field similar to the standard grid-based methods. Cummins and Rudman [139] and Shao and Lo [135] employed a strict incompressible SPH

formulation by solving a global pressure Poisson equation. Accurately solving global pressure Poisson equation requires relative small time step, in particular for the problem with large deformation, subsequently high computational cost. To reduce the computational costs while at the same time improve the efficiency of numerical scheme as well as numerical stability, a flexible pressure-correction equation is proposed here and detailed derivation is provided in the following.

Starting from the Lagrangian form of continuity equation,

$$\frac{D\rho}{Dt} = -\rho\nabla\cdot\vec{v}\,, \tag{4.15}$$

one can substitute Eq. (4.6) into Eq. (4.15) to obtain the pressure change with time as follows,

$$\frac{DP}{Dt} = -\rho c^2\nabla\cdot\vec{v}\,. \tag{4.16}$$

The expression of Eq. (4.16) in the SPH formulation becomes

$$\frac{P_i^{n+1}-P_i^n}{c^2\delta t} + \sum_{j=1}^{N} m_j\left(\vec{v}_j^{n+1}-\vec{v}_i^{n+1}\right)\nabla_i W_{ij}^n = 0\,, \tag{4.17}$$

where n denotes time step. The RHS of Eq. (4.17) should be zero if calculation is convergent. During iteration, however, it is not satisfied. Let us set

$$S = \frac{P_i^{n+1}-P_i^n}{c^2\delta t} + \sum_{j=1}^{N} m_j\left(\vec{v}_j^{n+1}-\vec{v}_i^{n+1}\right)\nabla_i W_{ij}^n\,. \tag{4.18}$$

From the Newton's method, a pressure-correction equation can be achieved,

$$\begin{aligned}\delta P_i^{n+1} &= -\frac{S}{\left(\partial S/\partial P\right)}\\ &= -\left(\frac{1}{c^2\delta t}\right)^{-1}\left[\frac{P_i^{n+1}-P_i^n}{c^2\delta t} + \sum_{j=1}^{N} m_j\left(\vec{v}_j^{n+1}-\vec{v}_i^{n+1}\right)\nabla_i W_{ij}^n\right]\,.\\ &= -\left[P_i^{n+1}-P_i^n + c^2\delta t\sum_{j=1}^{N} m_j\left(\vec{v}_j^{n+1}-\vec{v}_i^{n+1}\right)\nabla_i W_{ij}^n\right]\end{aligned} \tag{4.19}$$

Thus the pressure at the new time step is written as

$$P_i^{n+1} = P_i^n + \omega\delta P_i^{n+1}\,, \tag{4.20}$$

where ω is the relaxation factor for pressure correction which is in the range of 0.7 to 1.0. The velocity correction term can be achieved from the following momentum equation,

$$\frac{D\vec{u}}{Dt} = \nabla\cdot(\nu\nabla\vec{u}) - \frac{\nabla p}{\rho} + \vec{f} \tag{4.21}$$

where ν is the dynamic viscosity. The velocity correction is

$$\frac{\delta u_i^{n+1}}{\delta t} = -\frac{\delta p_i^{n+1}}{\rho_i}\,, \tag{4.22}$$

and the velocity is updated through

$$u_i^{n+1} = u_i^{n+1} - \Omega \frac{\delta t}{\rho_i} \frac{\delta P_i^{n+1}}{\delta x_i}. \tag{4.23}$$

Ω in Eq. (4.23) is the relaxation factor for velocity correction and its value is between 0.2 to 1.0.

Eqs. (4.20) and (4.23) are solved iteratively at each time step until Eq. (4.17) is satisfied. During each time step, the acoustic wave travels to the neighboring area with a constant speed so that the accumulation of SPH particles in the local high pressure area can be eased. Consequently, the pressure disturbance that causes numerical instability could be reduced. It is noted that the current method provides a combination of the equation of state method and the global pressure Poisson method. The weighting level for each method is given in terms of the value of the speed of sound chosen.

4.2.2 Surface Tension

Surface tension plays a significant role in bubble dynamics and droplet spreading. From the point of view of microscopic scale transport, molecules in a fluid are attracted by neighboring molecules. Inside the fluid, these attractive forces are canceled out and molecules are in a balanced state. On the free surface, however, there exists a net force in the direction of surface normal towards the fluid. Morris [140] firstly used the SPH method to simulate surface tension acting on an interface between two fluids and demonstrated the interface deformation with similar density and viscosity of two fluids. The method is, however, difficult to be extended to high density and viscosity ratios of two fluids, like water and air. Nugent [141] applied the SPH method to van der Waals fluid and studied the effects of surface tension on the oscillation of a droplet with an initial rectangular shape. Tartakovsky and Meakin [142] improved the stability by considering the effects of particle-particle interactions with the interaction forces given by

$$F_{ij} = \begin{cases} s_{ij} \cos\left(\dfrac{1.5\pi}{3h} \left| \vec{r}_i - \vec{r}_j \right| \right) \dfrac{\vec{r}_i - \vec{r}_j}{\left| \vec{r}_i - \vec{r}_j \right|} & \left| \vec{r}_i - \vec{r}_j \right| \le 3h \\ 0 & \left| \vec{r}_i - \vec{r}_j \right| > 3h \end{cases}, \tag{4.24}$$

where sij is the strength of the force acting between particles. Although surface tension given by this method agrees well with the analytical solution, there are nonphysical particles clustering in the simulation. Meleán [143] improved the method

proposed by Nugent and removed tensile instability by adding an artificial viscous force and an energy generation term to the standard SPH equations. Meleán [144] used the SPH method to simulate the coalescence of colliding van der Waals liquid drops and considered the effects of different impact velocities on the collision of two drops. Their simulations were performed for low energy collisions. Unfortunately, the new method by Meleán had to compromise between avoiding tensile instability and reproducing the van der Waals phase diagram.

In this paper, surface tension is modeled explicitly based on the ideas of Morris [140] and following the work of Müller et al [138]. A so-called color field is used to determine the surface location. The smoothed color field is defined as

$$c_s\left(\vec{x}_i\right) = \sum_j \frac{m_j}{\rho_j} W_{ij}\left(\vec{x}_{ij}, h\right). \tag{4.25}$$

Surface normal field is obtained by the gradient field of the color field,

$$\vec{n} = \nabla c_s . \tag{4.26}$$

The curvature of the surface is represented by the divergence of surface normal field, which can be written as

$$\kappa = \frac{-\nabla^2 c_s}{\left|\vec{n}\right|}. \tag{4.27}$$

The surface tension forces, therefore, can be written as

$$f_s = \sigma\kappa\vec{n} = \sigma\frac{-\nabla^2 c_s}{\left|\vec{n}\right|}\vec{n} . \tag{4.28}$$

4.2.3 Solidification

Fulk [145] proposed an artificial heat model to describe heat conduction problem. The artificial heat model has the following form

$$H_i = 2\sum_{j=1}^{N} \frac{q_i + q_j}{\rho_i + \rho_j} \frac{u_i - u_j}{\left|x_{ij}\right|^2 + \varphi^2} \vec{x}_{ij} \cdot \nabla_i W_{ij} \tag{4.29}$$

where

$$q_i = \alpha_\Pi h_i \rho_i c_i \left|\nabla \cdot \vec{v}_i\right| + \beta_\Pi h_i^2 \rho_i \left|\nabla \cdot \vec{v}_i\right|^2 . \tag{4.30}$$

Noted that the artificial heat model is based on the difference of internal energy. However, heat conduction/convection is related to temperature difference. Although

the artificial heat model can be applied to the heat conduction/convection problem due to the linear relationship between the internal energy and temperature, it is not suitable to the problem with phase transform due to the incorrect prediction of heat transfer based on the internal energy. We, therefore, modify the artificial heat model as follows,

$$H_i' = \sum_{j=1}^{N} \frac{(c_{pi} + c_{pj})(q_i + q_j)}{(\rho_i + \rho_j)} \frac{T_i - T_j}{\left|x_{ij}\right|^2 + \varphi^2} \vec{x}_{ij} \cdot \nabla_i W_{ij} \tag{4.31}$$

where c_p is the specific heat of the particle. The modified model is based on the temperature difference and it will be used to study the solidification problem.

Based on the modified artificial heat model, the energy equation can be rewritten as

$$\frac{Du_i}{Dt} = \frac{1}{2}\sum_{j=1}^{N} m_j \left(\frac{p_i}{\rho_i^2} + \frac{p_j}{\rho_j^2} \right) \vec{v}_{ij} \cdot \nabla_i W_{ij} - \frac{1}{2}\sum_{j=1}^{N} m_j \left(\frac{\tau_i}{\rho_i^2} + \frac{\tau_j}{\rho_j^2} \right) : \vec{v}_{ij} \nabla_i W_{ij} + H_i' . \tag{4.32}$$

In order to demonstrate the capability of the SPH method to solve fluid flow with solidification, a simplified solidification model is used. According to the internal energy calculated from Eq. (4.32), the temperature can be obtained from a linear relationship between temperature and internal energy. The status of the SPH particle can be specified by the following rule considering the latent heat

$$u \begin{cases} > c_p T_m + L & liquid \\ between & melting \\ < c_p T_m & solid \end{cases} \tag{4.33}$$

where T_m is the melting temperature and L is the latent heat. These equations can be used to solve the flow field and temperature distribution as well as solidification interface movement. It shall be mentioned that the proposed solidification model is similar to the enthalpy method used in the meshed methods [124].

4.3 Behaviors of Single Droplet

Five sets of results are presented in this section. The first set is to demonstrate the capability of the pressure correction equation and other treatments. The contraction of an initial droplet of compressible fluid is designed to test the droplet contraction. In general, the attraction case is difficult to simulate because the attractive forces between particles are the source that causes instability in SPH simulations. We use both the traditional equation of state method and new pressure correction method to solve the same cases to test the capability of pressure correction

equation. The second set is to test the surface tension model by studying the evolution of initial square particle distribution to a single droplet. This is a common testing case used by many papers [143, 146]. From tests, we will know the efficiency of the method in dealing the bubble/droplet dynamics. Third case is to test the droplet and substrate interaction. SPH particle penetrating into the substrate and pressure wave generation at the impacting location are the two serious problems in the traditional SPH method. The new pressure correction method and the choice of kernels can resolve both issues. The results will also be used to compare with experimentally validated analytical solution. The fourth and fifth cases are to study the impact of 2D and 3D droplet with fragmentation and solidification and the capability of the improved SPH method. Droplet with fragmentation and solidification is a challenging problem for meshed based methods, especially in 3D. However, it is straightforward using the improved SPH method.

4.3.1 Droplet Dynamics

Figure 49(a) shows the initial particle distribution of a liquid droplet. A surface tension force is suddenly added on the surface of initial uniformly distributed particles in a droplet and causes the contraction of droplet. Surface tension force in Eq. (4.24) is used and the density of the droplet will increase. The parameters used in the simulation are shown in Table 6. The kernels of Eqs. (4.9) and (4.10) are employed. Figure 49(b) shows the contracted droplet result without the pressure-correction equation. One can see that particles move inward due to the surface tension force. The SPH particles cluster mostly at six locations. This indicates that the density field does not contract uniformly. For this case, simulation cannot continue at a certain point, and the contracted droplet explodes. However, stable contracted single droplet can be obtained successfully by enabling the pressure correction equation (see Figure 49c). The orderly particle distribution is formed with minor clustering and the fast propagation of acoustic wave is due to the pressure-correction equation. On the other hand, the computational cost per iteration is about the same for two methods.

Table 6 Parameters used in the simulations

Parameters	Value
Reference density, ρ	1000 kg/m^3
Speed of sound, c	10.0 m/s, or greater than ten times of maximum droplet velocity

Initial distance between two particles, dx	0.25×10^{-3} m
Smoothing length, h	0.25×10^{-3} m
Initial radius of droplet, r	5.0×10^{-3} m
Strength of surface tension, s_{ij}	10.0

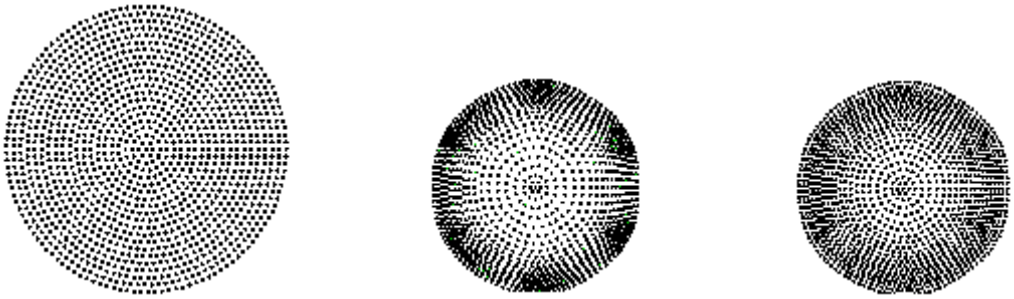

(a) **(b)** **(c)**

Figure 49 . Simulations of a droplet contraction: (a) initial distribution of SPH particles, (b) particle distribution after contraction using the equation of state, and (c) particle distribution after contraction with pressure correction

Figure 51 and Figure 51 show the evolution of initially particles distributed uniformly in a square geometry to a single droplet using different particle numbers. Surface tension of Eq. (4.28) has been applied with the kernels of Eqs. (4.9) and (4.10). The speed of sound is selected as such: it is greater than ten times of the maximum velocity so that the compressible of the fluid is limited within 2%. Figure 2 displays the results of a single droplet formation with 10×10 SPH particles. The evolution of particle distribution is similar to the formation of a stable Van der Waals liquid droplet obtained by Meleán [143]. Figure 51 shows the same physical problem with 20×20 SPH particles. The evolution of particle distribution shows from square to circle, to diamond, and then to square. The results in Figure 51 are similar to that in Blackbill et al [146]. Initially a square shaped of droplet results in strong surface forces at four corners, setting the droplet to oscillate. The periodicity of the oscillation may depend on droplet radius, strength of surface tension, and parameters used in the simulation. When particle number is smaller, numerical dissipation is stronger; oscillation will be damped quickly (see Figure 50). The accuracy of the simulation is improved by increased particle numbers, and a particular oscillation is able to last longer (see Figure 51).

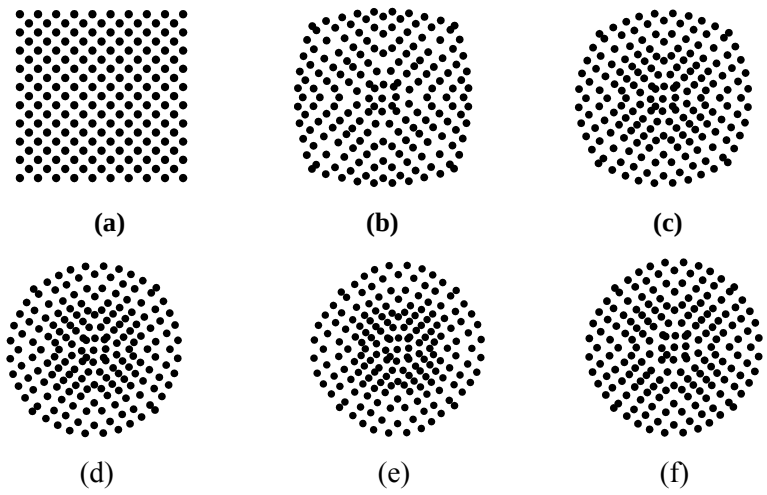

Figure 50 SPH particle distributions and surface geometries during oscillation of a liquid droplet from initial square distribution at (a) t = 0, (b) t = 0.015, (c) t = 0.03, (d) t = 0.045, (e) t = 0.06, and (f) t = 0.075s when the particle number of 10×10 is used.

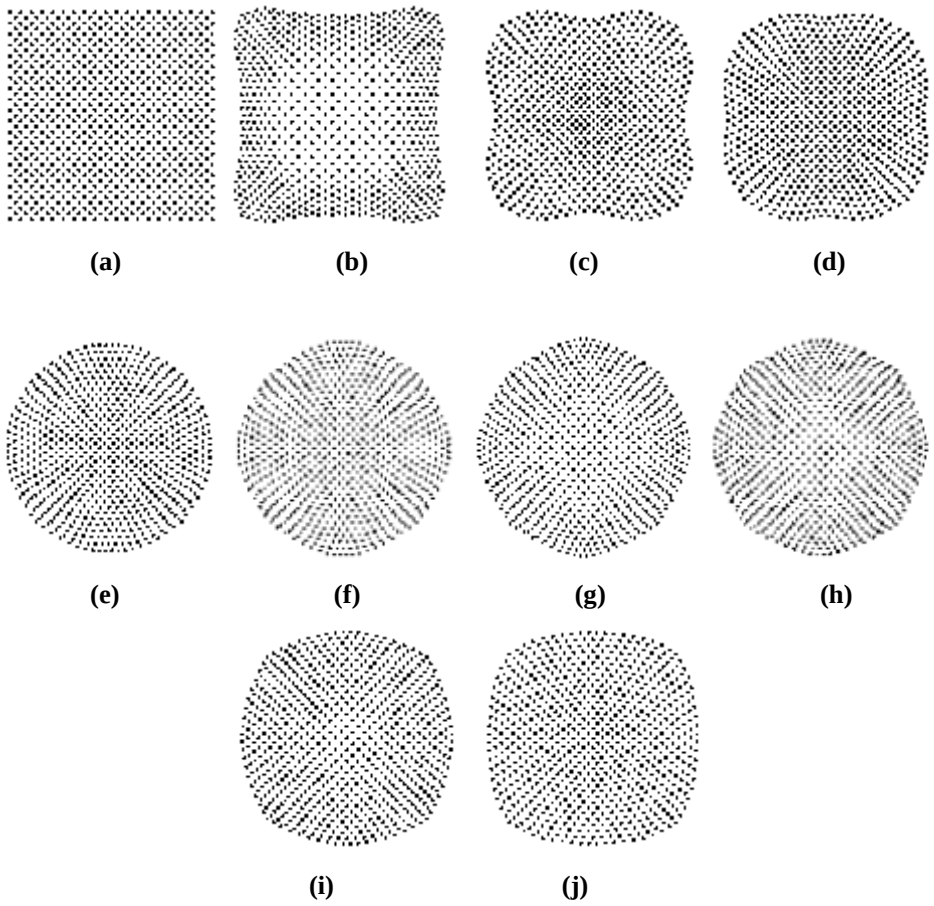

Figure 51 SPH particle distributions and surface geometries during oscillation of a liquid droplet from initial square distribution at (a) t = 0, (b) t = 0.01, (c) t = 0.03, (d) t = 0.05, (e) t = 0.1, (f) t = 0.4, (g) t = 0.8, (h) t = 1.2, (i) t = 1.4, and (j) t = 1.6 s when the particle number of 20×20 is used.

4.3.2 Droplet Impact on the Wall

This part presents the simulation of the impact of a single droplet using proposed models. Dynamic boundary conditions [147] are applied on the wall. The momentum dissipation of particle due to interactions with wall is modeled by the decrease of velocity. One of the important parameter in coating - flattening ratio, which is defined as the ratio between the final splat diameter and the initial droplet diameter, is calculated and compared with analytical solution. A simple relationship between the flattening ratio and Reynolds number is given as follows [148]

$$\xi_m = k\,\mathrm{Re}^{\alpha} \tag{4.34}$$

where k changes from 0.8 to 1.294 and α from 0.125 to 0.2 are used in the literature. If the Reynolds number is taken as 100, k is set to be 1.274, and α equals 0.2, the flattening ratio is calculated to be 3.2. The simulation results are shown in Figure 52. One can see that numerical result agrees well with theoretical prediction.

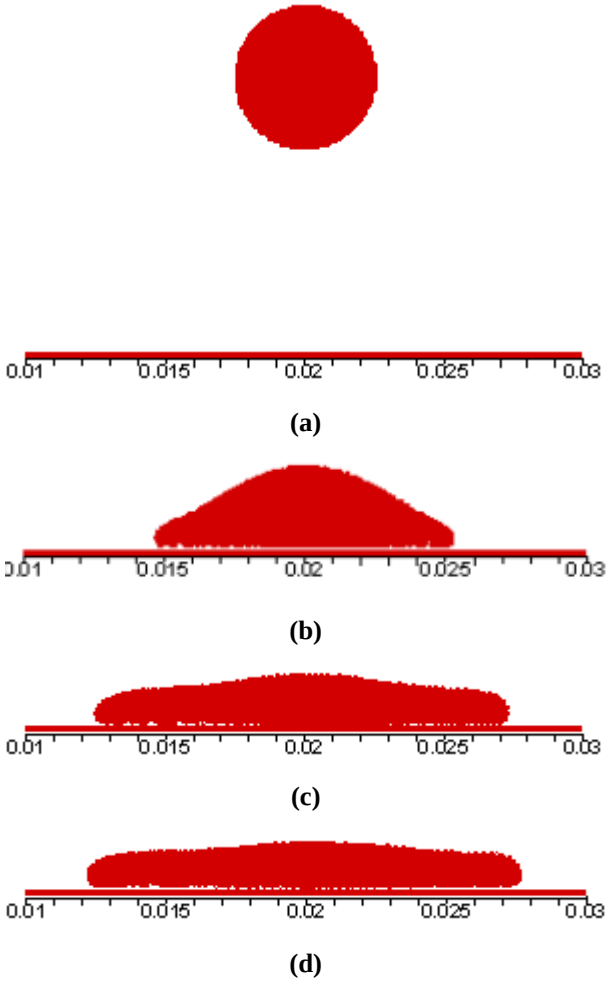

Figure 52 Single droplet impacts on a flat substrate with the Reynolds number of 100 at (a) t = 0, (b) t = 100, (c) t = 150, and (d) t = 200ms.

Figure 53 and Figure 54 display the time evolution of droplet spreading with the impact Reynolds of 10^4 and 10^5, respectively. When the droplet reaches the substrate, it begins to deform. Due to a high pressure formed at the center of impact location, droplet spreads on the substrate. A ring is formed on the edge of the droplet, whose shape is affected by surface tension. The interaction of liquid and wall particles around the ring behaves as a slip wall condition; no-slip wall conditions are satisfied at other locations. Increased Reynolds number results in a thinner thickness. Furthermore, the free surface changes from convex to concave due to increased Reynolds number. These phenomena agree well with the experimental observation [125].

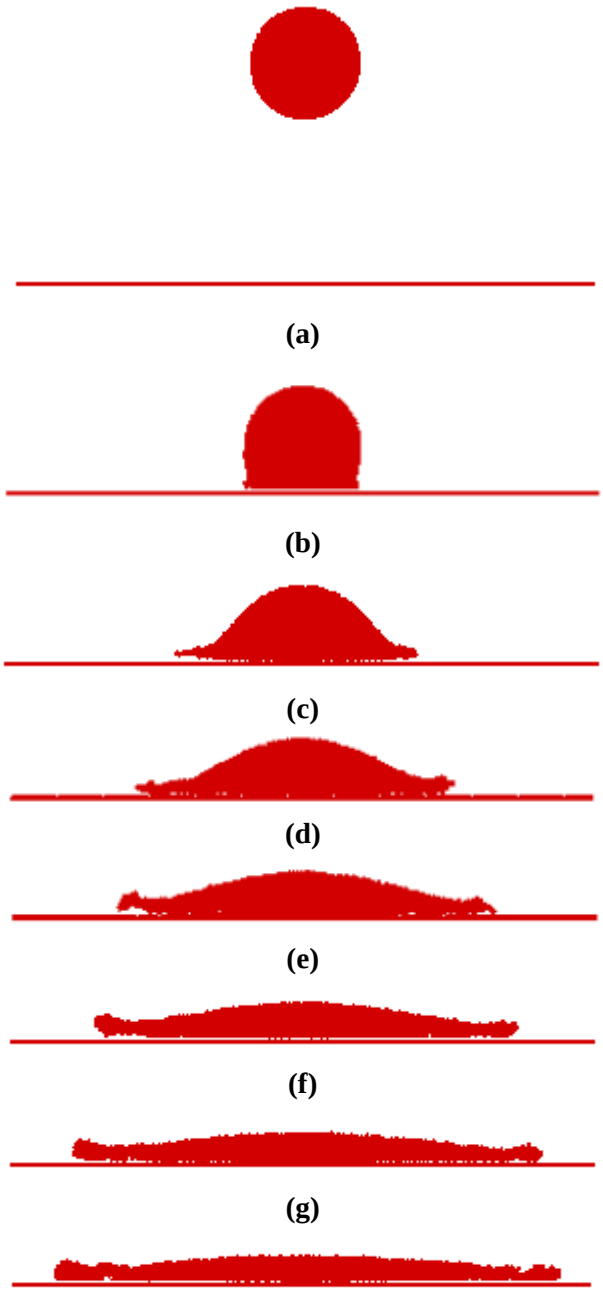

Figure 53 Droplet impact with the Reynolds number of 10^4 at (a) t=0, (b) t=312.5, (c) t=350, (d) t=387.5, (e) t=425, (f) t=462.5, (g) t=500, and (h) t=512.5ms

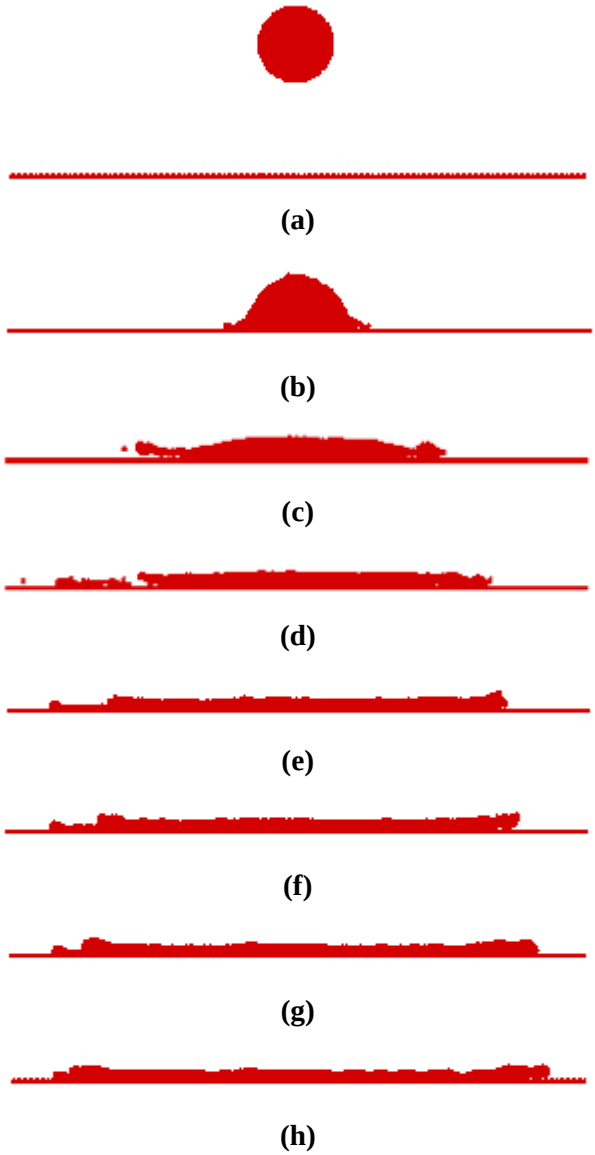

Figure 54 Droplet impact with the Reynolds number of 10^5 at (a) t=0, (b) t=87.5, (c) t=150, (d) t=212.5, (e) t=275, (f) t=337.5, (g) t=400, and (h) t=462.5ms

4.3.3 Droplet Impact and Solidification

In this simulation, the initial temperature of the droplet is assumed to be 300K uniformly. The substrate temperature is set to be 273K. Figure 55 and Figure 56 present the results of droplet impact and solidification. The simulation results revealed that once the droplet impacts the cold substrate, the solidification interface moves upwards and the droplet begins to solidify. Initially the solidification interface moves

upward quickly due to the rapid solidification and it captures many particles. Since spreading and solidification occurred at the same time, the following scenery can happen: the bottom solid particles were solidified while the upper liquid particles remain liquid. After the droplet completely spreads, two-layers of solidified particle distribution are observed, which agrees well with the silicon droplet impact and solidification experiments. When the Reynolds number is higher (see Figure 56), splashing and pinch-off are predicted.

The improved SPH model is here applied to simulate a three-dimensional droplet impact and solidification with the given kernels of Eqs. (4.11) to (4.14) are used. The results are shown in Figure 57. In this simulation, the surface meshes are generated using the techniques presented by Adams et al [149] and the images are rendered using ray tracing method with POVRAY. One can see that there are two-layers of solidified particle distribution due to spreading and solidification. The results are in good agreement with the experimental observation of the impact of silicon molten droplet.

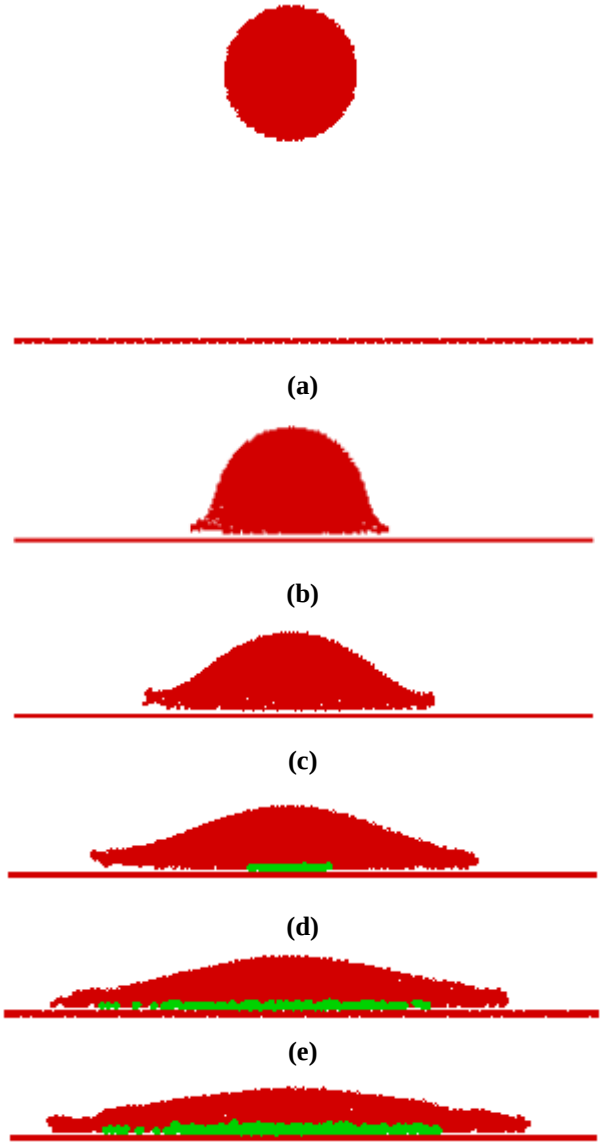

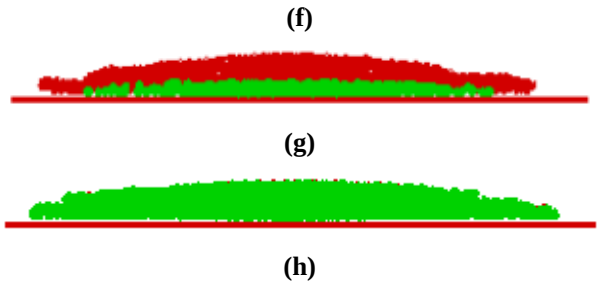

Figure 55 Droplet impact and solidification with the Reynolds number of 10^5 at (a) t=0, (b) t=325, (c) t=362.5, (d) t=400, (e) t=437.5, (f) t=475, (g) t=512.5, and (h) t=600ms.

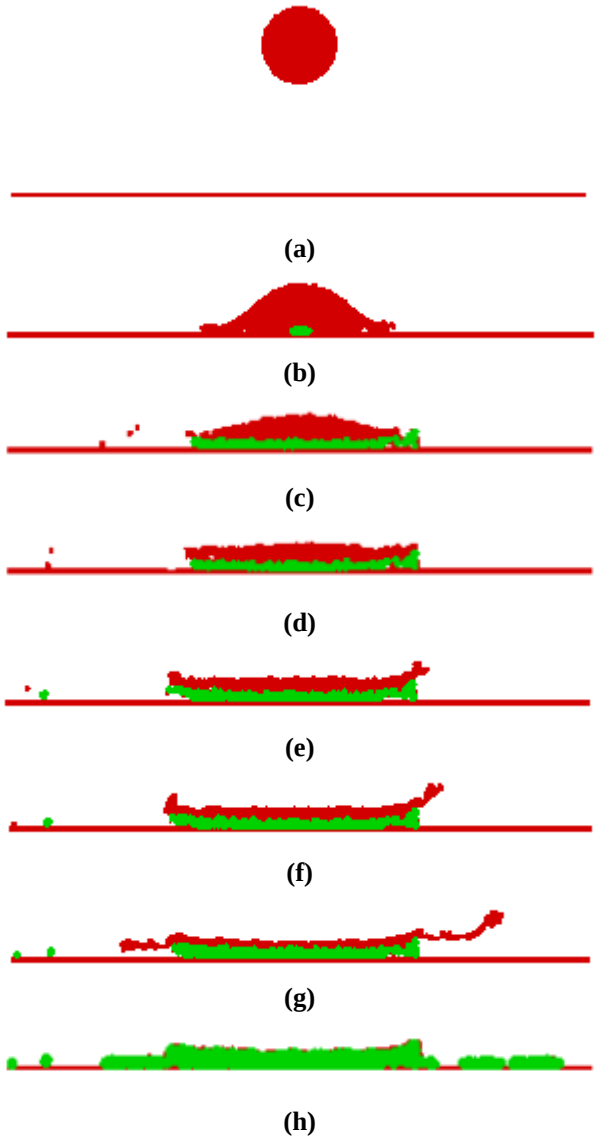

Figure 56 Droplet impact and solidification with the Reynolds number of 10^5, (a) t=0, (b) t=93.5, (c) t=125, (d) t=156.5, (e) t=187, (f) t=250, (g) t=375, and (h) t=500ms

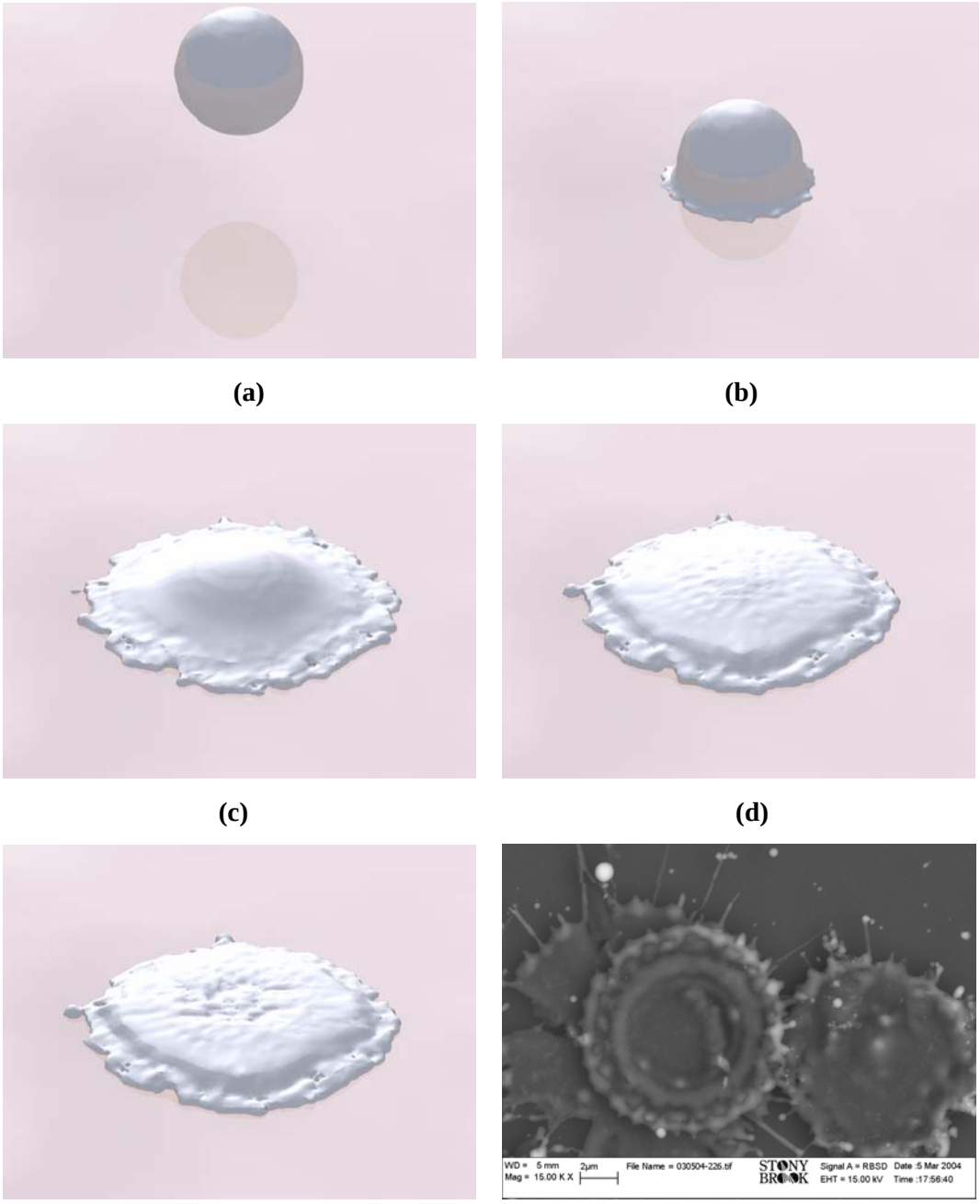

Figure 57 Droplet impact and solidification with the Reynolds number of 10^4 in 3D at (a) t=0, (b) t=80, (c) t=140, (d) t=200, (e) t=260ms, (f) experimental results of silicon droplet impact at the same condition.

Chapter 5 Conclusion and Future Work

5.1 Conclusions

5.1.1 Crystal Cracking

A numerical model has been developed to predict the temperature distributions in the Cz system for Yb:S-FAP crystal growth. Simulations have been benchmarked against experiment for both mono-linear and bi-linear ramp-down profiles. These results suggest that cracking occurs when radial temperature differences within the crystal exceed that of the critical value**,** which is defined as the temperature differences related to a critical thermal strain that caused the crystal cracking**.** Based on this result, an optimized three-stage power ramp-down profile was proposed and resulted in high-quality crack-free, 7.0 cm diameter Yb:S-FAP crystals. This success demonstrates the advantages of combining numerical simulation with experiment to improve crystal quality in Cz crystal growth systems and reduce process development time.

Furthermore, cracking patterns of grown crystals have been reviewed. It is found that the top, middle and bottom parts of the crystal are prone to cracking. New ring design has been proved effective to reduce the middle portion cracking. A new method has been presented to mitigate the cracking by pulling crystal out of hot zone to warm zone slowly during cooling process. Both experimental results and numerical prediction show it is feasible and proved to be a good idea to get crack-free crystals. Another benefit of the new cooling process is to mitigate the cracks without changes of furnace design so that it will not affect the current crystal growth conditions.

5.1.2 Melt Inclusion

Two melt inclusion mechanisms are reviewed. Both show the importance of solute pileup in front of the growth interface. Optical crystal growth by Czochralski method is simulated. Simulation results are conducted to examine the interface shape and flow pattern changes in the melt by different crystal rotation rates. A new design of submerged baffle is proposed to reduce natural convection in the melt and to improve the effect of crystal rotation on the flow pattern near the growth interface. Simulation results demonstrate the feasibility of the new design on enlarging the effect of forced convection so as to change the interface shape and flow pattern in the melt to control inclusion. In the experiments it is convenient to modify the height of disk to control melt inclusion in the crystal. Furthermore, the disk as a submerged heater is developed. Numerical simulation show the temperature distribution in the disk is very important. It is better to heat the disk to the temperature between melt temperature and the crucible temperature for increase forced convection under the crystal. Inclusion free or well-controlled crystals could be grown by the suggested techniques.

5.1.3 Single Droplet Behaviors

An improved SPH model has been developed and applied to free surface deformation without and with solidification based on a new pressure-correction equation together with different kernels for different terms. The surface tension and solidification models are also proposed. The improved SPH method has also been applied to study single droplet contraction without gravity, and droplet high speed impact without and with solidification, as well as three-dimensional droplet impact and solidification. It is concluded from the simulation results that the proposed pressure-correction equation is capable of improving numerical stability. The improved SPH method can handle free surface and solidification problems very well. It is also concluded that when solidification is present, two layers in solidification particle distribution are observed. When the Reynolds number is sufficiently high, splashing and pin-off happen. These phenomena agree well with experiments. It proves the SPH method a powerful tool to study droplet spreading and solidification.

5.2 Future Work

Based on the work performed in this dissertation, the following recommendations are made for the near-future research on the simulation of optical crystal growth:

(1) Further investigation of crystal cracking by considering three-dimensional effects, and calculating thermal stresses instead of temperature differences as the criterion for crystal cracking;

(2) Further study of effects of furnace geometries on crystal cracking, such as the length of insulation, furnace height, and coil position;

(3) Further investigation of melt inclusion by solving solute equation to predict solute pileup;

(4) Comparison of numerical simulation results of submerged heater with experimental observation, and further improvement of submerged heater to be applied in Cz growth system;

(5) Development of local model for melt inclusion by combining SPH meshless method and grid-based method;

(6) Study of treatment of fluid flow and heat transfer between particle method and grid-based method.

References

1. Maiman, T.H., *Simulated optical radiation in ruby.* Nature (London), 1960. **187**: p. 493-494.
2. Johnson, L.F., Boyd, G. D., Nassau, K., and Soden, R. R., *Continuous operation of a solid-state optical laser.* Phys. Rev., 1962. **126**: p. 1406-1409.
3. L.D. DeLoach, S.A.P., L.K. Smith, W.L. Kway, W.F. Krupke, J. Opt. Soc. Am., 1994. **B.11**: p. 269.
4. S.A. Payne, L.K.S., L.D. DeLoach, W.L. Kway, J.B. Tassano, W.F. Krupke, IEEE J. Quantum Electron, 1994. **30**: p. 170.
5. S.A. Payne, L.D.D., L.K. Smith, W.L. Kway, J.B. Tassano, W.F. Krupke, B.H.T. Chai, G. Loutts, J. Appl. Phys, 1994. **76**(1): p. 497.
6. DeLoach, L.D., S.A. Payne, W.L. Kway, J.B. Tassano, S.N. Dixit, and W.F. Krupke, *Vibrational structure in the emission spectra of Yb3+-doped apatite crystals.* Journal of Luminescence, 1994. **62**(2): p. 85-94.
7. Schaffers, K.I., *Yb:S-FAP lasers.* Opt. Mater. , 2004. **26**(4): p. 391-394.
8. B. Pati, Y.I., K. F. Wall, P. F. Moulton,, in: John J. Zayhowski (Ed.), OSA Trends in Optics and Photonics on Advanced Solid State Photonics, 2003: p. 197.
9. S. Yiou, F.B., K. I. Schaffers, P. Georges, in: John J. Zayhowski (Ed.), OSA Trends in Optics and Photonics on Advanced Solid State Photonics, 2003: p. 438.
10. S. Ito, H.I., T. Yanagida, A. Endo, F. Sakai, K. Torizuka, in: John J. Zayhowski (Ed.), OSA Trends in Optics and Photonics on Advanced Solid State Photonics, 2003: p. Post-deadline poster.
11. Ito, S., T. Nakajyo, T. Yanagida, F. Sakai, A. Endo, and K. Torizuka, *Diode-pumped, chirped-pulse Yb:S-FAP regenerative amplifier for laser-Compton X-ray generation.* Optics Communications, 2006. **259**(2): p. 812-815.
12. G.M. McManus, R.H.H., W.J. Takei, J. Appl. Phys., 1969. **40**(1): p. 180.
13. Schaffers, K.I., J.B. Tassano, A.B. Bayramian, and R.C. Morris, *Growth of Yb: S-FAP [Yb3+:Sr5(PO4)3F] crystals for the Mercury laser.* Journal of Crystal Growth, 2003. **253**(1-4): p. 297-306.
14. Schaffers, K.I., J.B. Tassano, P.A. Waide, S.A. Payne, and R.C. Morris, *Progress in the growth of Yb : S-FAP laser crystals.* J. Cryst. Growth, 2001. **225**(2-4): p. 449-453.
15. Czochralski, J., *Ein neues verfahren zue messung der kristallisation-geschwindigkeit der metalle.* Z. Phys. Chem., 1918. **92**: p. 219-221.

16. Shimura, F., *Semiconductor Silicon Crystal Technology.* Academic Press, Orlando, FL., 1989.
17. Hurle, D.T.J., Cockayne, B., *Czochralski growth* In Handbook of Crystal Growth (D.T.J. Hurle, ed.), North-Holland, NY., 1994. **2a**: p. 99-211.
18. Pressley, R.J., *Handbook of Lasers with selected data on optical technology.* Chem. Rubber Publ. Co., Cleveland, OH., 1971.
19. Cockayne, B., *The melt growth of oxide and related single crystals.* Journal of Crystal Growth, 1977. **42**: p. 413-426.
20. Yu, H., Y. Yu, H. Zhang, Z. Wang, J. Wang, X. Cheng, Z. Shao, and M. Jiang, *Growth and laser characterization of mixed Nd:LuxGd1-xVO4 laser crystals.* Journal of Crystal Growth, 2006. **293**(2): p. 394-397.
21. Lu, Y., J. Wang, Y. Yang, Y. Dai, A. Dong, and B. Sun, *Growth and optical properties of Tm:YAlO3 single crystals with different Tm concentrations.* Journal of Alloys and Compounds, 2007. **429**(1-2): p. 296-300.
22. Zhang, Y., Z. Lin, L. Zhang, and G. Wang, *Growth and optical properties of Yb3+-doped Sr3Gd2(BO3)4 crystal.* Optical Materials, 2007. **29**(5): p. 543-546.
23. Li, X., Z. Lin, L. Zhang, and G. Wang, *Growth and spectral properties of Yb3+-doped NaY(MoO4)2 crystal.* Optical Materials, 2007. **29**(6): p. 728-731.
24. Song, P., Z. Zhao, X. Xu, P. Deng, and J. Xu, *Growth and spectral properties of Yb:FAP single crystal.* Optical Materials, 2007. **29**(5): p. 471-474.
25. Bensalah, A., M. Ito, Y. Guyot, C. Goutaudier, A. Jouini, A. Brenier, H. Sato, T. Fukuda, and G. Boulon, *Spectroscopic properties and quenching processes of Yb3+ in Fluoride single crystals for laser applications.* Journal of Luminescence, 2007. **122-123**: p. 444-446.
26. Fei, Y., B.H.T. Chai, C.A. Ebbers, Z.M. Liao, K.I. Schaffers, and P. Thelin, *Large-aperture YCOB crystal growth for frequency conversion in the high average power laser system.* Journal of Crystal Growth, 2006. **290**(1): p. 301-306.
27. A.J. Nelson, T.v.B., C. Bostedt, K.I. Schaffers, L.J. Terminello, M. Engelhard, D.Baer, J. Appl. Phys., 2002. **91**(8): p. 5135.
28. L.D. DeLoach, S.A.P., L.L. Chase, L.K.Smith, W.L. Kway, W.F. Krupke, IEEE J. Quantum Electron, 1993. **29**: p. 1179.
29. Chalmers, B., *Principles of Solidification.* Wiley, New york, 1964: p. 150.
30. Brice, J.C., *The cracking of Czochralski-grown crystals.* Journal of Crystal Growth, 1977. **42**: p. 427-430.
31. Langlois, W.E., *Convection in Czochralski growth melts.* PCH, PhysicoChem. Hydrodyn., 1981. **2**(245-261).
32. Kobayashi, N., *Computational simulation of the melt flow during Czochralski growth.* Journal of Crystal Growth, 1978. **43**(3): p. 357-363.
33. Jones, A.D.W., *An experimental model of the flow in Czochralski growth.* Journal of Crystal Growth, 1983. **61**(2): p. 235-244.
34. Hurle, D.T.J., E. Jakeman, and E.R. Pike, *Striated solute distributions produced by temperature oscillations during crystal growth from the melt.*

Journal of Crystal Growth, 1968. **3-4**: p. 633-640.
35. Kobayashi, N., *Oxygen transport under an axial magnetic field in Czochralski silicon growth.* Journal of Crystal Growth, 1991. **108**(1-2): p. 240-246.
36. Yen, C.T. and W.A. Tiller, *Oxygen partitioning analysis during Czochralski silicon crystal growth via a dopant marker and a simple transfer function modeling technique II. Growth velocity and applied magnetic field transients.* Journal of Crystal Growth, 1992. **118**(1-2): p. 85-92.
37. Chan, Y.T., Gibeling, H.J., and Grubin, H.L., *Numerical simulation of the Czocharalski growth.* J. Appl. Phys, 1988. **64**: p. 1425-1439.
38. Brown, R.A., *Theory of transport in single crystal growth from the melt.* AIChE J., 1988. **43**(6): p. 881-911.
39. Müller, G., *Convection and inhomogeneities in crystal growth from melt.* In Crystals, (H. C. Freyhardt,ed.), Springer-Verlag, Berlin, 1988. **12**.
40. Prasad, V., and Zhang, H., *Challenging issued in bulk crystal growth modeling.* Cryst. Growth Novel Electron. Mater. Cer. Trans., 1995. **60**: p. 3-36.
41. Chang, C.J. and R.A. Brown, *Radial segregation induced by natural convection and melt/solid interface shape in vertical bridgman growth.* Journal of Crystal Growth, 1983. **63**(2): p. 343-364.
42. Derby, J.J. and R.A. Brown, *Thermal-capillary analysis of Czochralski and liquid encapsulated Czochralski crystal growth : II. Processing strategies.* Journal of Crystal Growth, 1986. **75**(2): p. 227-240.
43. Derby, J.J., L.J. Atherton, and P.M. Gresho, *An integrated process model for the growth of oxide crystals by the Czochralski method.* Journal of Crystal Growth, 1989. **97**(3-4): p. 792-826.
44. Brown, R.A., T.A. Kinney, P.A. Sackinger, and D.E. Bornside, *Toward an integrated analysis of czochralski growth.* Journal of Crystal Growth, 1989. **97**(1): p. 99-115.
45. Crowley, A.B., E.J. Stern, and D.T.J. Hurle, *Modelling of the growth of GaAs by the LEC technique : I. Thermal distribution in the crystal.* Journal of Crystal Growth, 1989. **97**(3-4): p. 697-708.
46. Koai, K., A. Seidl, H.J. Leister, G. Muller, and A. Kohler, *Modelling of thermal fluid flow in the liquid encapsulated Czochralski process and comparison with experiments.* Journal of Crystal Growth, 1994. **137**(1-2): p. 41-47.
47. Moallemi, M.K., and Zhang, H., *Surface tension effects on solidification of thin films via dip coating process.* J. Mater. Proc. Manuf. Sci., 1993. **2**: p. 233-243.
48. Zhang, H., and Moallemi, M. K., *A multizone adaptive grid genration technique for simulation of moving and free boundary problems.* Numer. Heat Transfer, 1995. **Part B 27**(255-276).
49. Zhang, H., Prasad, V., and Moallemi, M. K., *A numerical algorithm using multizone grid generation for multiphase transport processes with moving and free boundaries.* Numer. Heat Transfer, 1996. **Part B 29**: p. 399-421.
50. Zhang, H., and Prasad, V., *Multizone adaptive simulations for high pressure*

crystal growth. ASME/JSME Therm. Eng. J. Conf., Maui, Hawaii, 1995: p. 559-568.

51. Zhang, H., V. Prasad, and D.F. Bliss, *Modeling of high pressure, liquid-encapsulated Czochralski growth of InP crystals.* Journal of Crystal Growth, 1996. **169**(2): p. 250-260.
52. Ristorcelli, J.R. and J.L. Lumley, *Instabilities, transition and turbulence in the Czochralski crystal melt.* Journal of Crystal Growth, 1992. **116**(3-4): p. 447-460.
53. Ono, N., Kida, M., Arai, Y., and Sahira, K., *Thermal-analysis of the double-crucible method in continuous silicon Czochralski processing. 2. Numerical analysis.* J. Electrochem. Soc., 1993. **140**: p. 2106-2111.
54. Kinney, T.A., D.E. Bornside, R.A. Brown, and K.M. Kim, *Quantitative assessment of an integrated hydrodynamic thermal-capillary model for large-diameter Czochralski growth of silicon: comparison of predicted temperature field with experiment.* Journal of Crystal Growth, 1993. **126**(2-3): p. 413-434.
55. Kinney, T.A. and R.A. Brown, *Application of turbulence modeling to the integrated hydrodynamic thermal-capillary model of Czochralski crystal growth of silicon.* Journal of Crystal Growth, 1993. **132**(3-4): p. 551-574.
56. Zhang, T., Ladeinde, F., Zhang, H., and Prasad, V., *A comparison of turbulence models for natural convection in enclosures: Applications to crystal growth processes.* Proc. 31st Natl. Heat Transfer Conf., Houston, TX, ASME HTD, NY, 1996. **323**: p. 17-26.
57. Fang, H., D. Cai, H. Zhang, and L. Zheng, *Transport Phenomena in Growth and Annealing of Laser Crystals.* Proceedings of 2006 ASME International Mechanical Engineering Congress & Exposition, IMECE 2006-13831, Chicago, Illinois, USA, Nov.05-10, 2006.
58. Fang, H., D. Cai, H. Zhang, and L. Zheng, *A Novel Method for Melt Flow Control and Inclusion Suppression in Optical Crystal Growth.* Proceedings of 2007 ASME International Mechanical Engineering Congress & Exposition, IMECE 2007-41581, Seattle, Washington, USA, Nov. 11-15, 2007.
59. Fang, H., R. Qiu, K.I. Schaffers, J.B. Tassano, H. Zhang, and L. Zheng, *Induction Heated Czochralski Growth and Cooling of Yb:S-FAP Laser Crystals.* Poster on ACCGE/West-20 (American Conference on Crystal Growth and Epitaxy), Sierra Nevada Mountains near Lake Tahoe, Nevada, USA, June 4-7, 2006.
60. Fang, H., L. Zheng, and H. Zhang, *Control of Flow Pattern and Solidification Interface Shape in an Induction Heated Czochralski Crystal Growth System.* Proceedings of 2007 ASME-JSME Thermal Engineering Summer Heat Transfer Conference, HT2007-32288, Vancouver, British Columbia, CANADA, July 8-12, 2007.
61. Fang, H., L. Zheng, H. Zhang, Y. Hong, and Q. Deng, *To Reduce Melt Inclusion Using Submerged Heater or Baffle in Optical Crystal Growth* Crystal Growth & Design, 2008. **(Accepted)**.

62. Fang, H., L. Zheng, H. Zhang, R. Qiu, K.I. Schaffers, and J.B. Tassano, *Controlled Cooling to Mitigate Cracking in Large Diameter Crystals.* The 15th International Conference on Crystal Growth (ICCG-15), Slat Lake City, Utah, USA, August 12-17, 2007.
63. Fang, H.S., L.L. Zheng, S.R. Qiu, K.I. Schaffers, J.B. Tassano, and H. Zhang, *Optimization of the cooling profile to achieve crack-free Yb:S-FAP crystals.* Journal of Crystal Growth, 2008. **(Accepted)**.
64. Metzger, M. and R. Backofen, *Optimal temperature profiles for annealing of GaAs-crystals.* J. Cryst Growth, 2000. **220**(1-2): p. 6-15.
65. Eastwood, L.W., *Gas in Light Alloys.* John Wiley, New York, 1946. **Chapter 11**.
66. Wilcox, W.R. and V.H.S. Kuo, *Gas bubble nucleation during crystallization.* Journal of Crystal Growth, 1973. **19**(4): p. 221-228.
67. Vasconcellos, K.F. and J. Beech, *The development of blowholes in the ice/water/carbon dioxide system.* Journal of Crystal Growth, 1975. **28**(1): p. 85-92.
68. Boomgaard, J.V.D., *Gas bubble formation ahead of a solidification front.* Phillips journal of Research, 1978. **33**: p. 149-185.
69. Viskanta, M.V.A.B.a.R., *Gas segregation during solidification processes.* Int. J. Heat Mass Transfer, 1996. **40**(9): p. 2035-2043.
70. Jackson, K.A. and J.D. Hunt, *Transparent Compounds That Freeze Like Metals.* Journal of Metals, 1965. **17**(9): p. 1031-&.
71. Dorsey, N.E., *Properties of Ordinary Water-Substance.* Reinhold, New York, 1940: p. 414-415.
72. Chalmers, B., *How water freezes.* Scientific American, 1959. **200**: p. 114-122.
73. Wei, P.S., Y.K. Kuo, S.H. Chiu, and C.Y. Ho, *Shape of a pore trapped in solid during solidification.* International Journal of Heat and Mass Transfer, 2000. **43**(2): p. 263-280.
74. Nakajima, K.M.a.H., Mater. Trans., 2002. **43**: p. 2582.
75. Wei, P.S., C.C. Huang, Z.P. Wang, K.Y. Chen, and C.H. Lin, *Growths of bubble/pore sizes in solid during solidification--an in situ measurement and analysis.* Journal of Crystal Growth, 2004. **270**(3-4): p. 662-673.
76. Song, P., Z. Zhao, X. Xu, P. Deng, and J. Xu, *Crystal growth and properties of Yb:FAP laser crystal.* J. Cryst. Growth, 2005. **277**(1-4): p. 181-185.
77. Vasiliev, M.G., O.N. Budenkova, V.S. Yuferev, V.V. Kalaev, V.N. Shlegel, N.V. Ivannikova, Y.V. Vasiliev, and V.M. Mamedov, *Effect of heat shield on the shape of the solid-liquid interface and temperature field in the BGO-eulithine LTG Cz growth.* Journal of Crystal Growth, 2005. **275**(1-2): p. e745-e750.
78. Yu-long Zhang, l.T., *Man-made crystal-growth technique, functionality and application.* Chemical Industry Press, China, 2005.
79. Ma, R.H., H. Zhang, S. Ha, and M. Skowronski, *Integrated process modeling and experimental validation of silicon carbide sublimation growth.* J. Cryst. Growth, 2003. **252**(4): p. 523-537.
80. Ma, R.H., H. Zhang, V. Prasad, and M. Dudley, *Growth kinetics and thermal*

stress in the sublimation growth of silicon carbide. Cryst. Growth Des., 2002. **2**(3): p. 213-220.

81. Wu, B., R. Ma, H. Zhang, M. Dudley, R. Schlesser, and Z. Sitar, *Growth kinetics and thermal stress in AlN bulk crystal growth.* J. Cryst. Growth, 2003. **253**(1-4): p. 326-339.
82. Tavakkoli, M.H. and H. Wilke, *Numerical study of induction heating and heat transfer in a real Czochralski system.* J. Cryst. Growth, 2005. **275**(1-2): p. e85-e89.
83. Gevelber, M.A. and G. Stephanopoulos, *Dynamics and control of the Czochralski process : I. Modelling and dynamic characterization.* J. Cryst. Growth, 1987. **84**(4): p. 647-668.
84. Hurle, D.T.J., G.C. Joyce, M. Ghassempoory, A.B. Crowley, and E.J. Stern, *The dynamics of czochralski growth.* Journal of Crystal Growth, 1990. **100**(1-2): p. 11-25.
85. Irizarry-Rivera, R. and W.D. Seider, *Model-predictive control of the Czochralski crystallization process. Part I. Conduction-dominated melt.* Journal of Crystal Growth, 1997. **178**(4): p. 593-611.
86. Masi, M., S. Carra, M. Polli, M. Ratti, and G. Guadalupi, *Transient dynamics and control of indium phosphide LEC furnaces.* Mater. Chem. Phys. , 2000. **66**(2-3): p. 236-245.
87. Nunes, E.M., M.H.N. Naraghi, H. Zhang, and V. Prasad, *A volume radiation heat transfer model for Czochralski crystal growth processes.* Journal of Crystal Growth, 2002. **236**(4): p. 596-608.
88. Hossain, M.A. and H.S. Takhar, *Radiation effect on mixed convection along a vertical plate with uniform surface temperature.* Heat Mass Transfer., 1996. **31**(4): p. 243-248.
89. Ozisik, M.N., *Heat Conduction*. 1980: Wiley, New york.
90. Nassau, K. and A.M. Broyer, *Calcium Tungstate - Czochralski Growth, Perfection, and Substitution.* Journal of Applied Physics, 1962. **33**(10): p. 3064-&.
91. Cockayne, B., M. Chesswas, J.G. Plant, and A.W. Vere, *Ferroelectric Domains and Growth Striae in Barium Sodium Niobate Single Crystals.* Journal of Materials Science, 1969. **4**(7): p. 565-&.
92. Cockayne, B., *in: Current Topics in Materials Sciences.* North-Holland, Amsterdam, 1977. **2, Ed. E. Kaldis**.
93. Miyazawa, S., *Fluid-flow effect on gas-bubble entrapment in Czochralski-grown oxide crystals.* Journal of Crystal Growth, 1980. **49**(3): p. 515-521.
94. Nicoara, I., O.M. Bunoiu, and D. Vizman, *Voids engulfment in shaped sapphire crystals.* Journal of Crystal Growth, 2006. **287**(2): p. 291-295.
95. Xu, Y.N., W.Y. Ching, and B.K. Brickeen, *Electronic structure and bonding in garnet crystals Gd3Sc2Ga3O12, Gd3Sc2Al3O12, and Gd3Ga3O12 compared to Y3Al3O12.* Physical Review B, 2000. **61**(3): p. 1817-1824.
96. Jia, Z., X. Tao, C. Dong, X. Cheng, W. Zhang, F. Xu, and M. Jiang, *Study on*

crystal growth of large size Nd3+: Gd3Ga5O12 (Nd3+: GGG) by Czochralski method. Journal of Crystal Growth, 2006. **292**(2): p. 386-390.
97. Rudolph, P., A. Engel, I. Schentke, and A. Grochocki, *Distribution and genesis of inclusions in CdTe and (Cd,Zn)Te single crystals grown by the Bridgman method and by the travelling heater method.* Journal of Crystal Growth, 1995. **147**(3-4): p. 297-304.
98. Schieber, M., T.E. Schlesinger, R.B. James, H. Hermon, H. Yoon, and M. Goorsky, *Study of impurity segregation, crystallinity, and detector performance of melt-grown cadmium zinc telluride crystals.* Journal of Crystal Growth, 2002. **237-239**(Part 3): p. 2082-2090.
99. Rudolph, P. and M. Muhlberg, *Basic Problems of Vertical Bridgman Growth of Cdte.* Materials Science and Engineering B-Solid State Materials for Advanced Technology, 1993. **16**(1-3): p. 8-16.
100. Rudolph, P., M. Neubert, and M. Muhlberg, *Defects in Cdte Bridgman Monocrystals Caused by Nonstoichiometric Growth-Conditions.* Journal of Crystal Growth, 1993. **128**(1-4): p. 582-587.
101. Burton, J.A., R.C. Prim, and W.P. Slichter, *The Distribution of Solute in Crystals Grown from the Melt .1. Theoretical.* Journal of Chemical Physics, 1953. **21**(11): p. 1987-1991.
102. Wagner, C., *Theoretical Analysis of Diffusion of Solutes During the Solidification of Alloys.* Journal of Metals, 1954. **6**(2): p. 154-160.
103. Papapetrou, A., *Investigations on the dendrite growth of crystals.* Zeitschrift Fur Kristallographie, 1935. **92**(1/2): p. 89-129.
104. Tiller, W.A., K.A. Jackson, J.W. Rutter, and B. Chalmers, *The Redistribution of Solute Atoms During the Solidification of Metals.* Acta Metallurgica, 1953. **1**(4): p. 428-437.
105. Mullins, W.W. and R.F. Sekerka, *Stability of Planar Interface During Solidification of Dilute Binary Alloy.* Journal of Applied Physics, 1964. **35**(2): p. 444-&.
106. Flemings, M.C., *Solidification Processing.* McGraw-Hill, New York, 1974.
107. Hucke, E., Adams, C., Flemings, M.C., and Taylor, H. F., *in "Physical Chemistry of Process Metallurgy".* Interscience Publishers, Inc., New York, 1961. **pt. II, p. 815**.
108. Hurle, D.T.J., *Constitutional Supercooling During Crystal Growth from Stirred Melts .1. Theoretical.* Solid-State Electronics, 1961. **3**(1): p. 37-44.
109. Rigopoulos, S. and A.G. Jones, *Dynamic modelling of a bubble column for particle formation via a gas-liquid reaction.* Chemical Engineering Science, 2001. **56**(21-22): p. 6177-6184.
110. Jackson, J., *Classical Electrodynamics.* Wiley, New York, 1975.
111. Xiong, H.B., Y. Ma, and L.L. Zheng, *A modified HEM system for optical crystal growth with high melting temperature.* Journal of Crystal Growth, 2007. **299**(2): p. 404-412.
112. Prasad, V., Zhang, H., and Anselmo, A.P., *Transport Phenomena in Czochralski Crystal Growth Process.* Advances In Heat Transfer, 1997. **30**: p.

313-435.
113. Ostrogorsky, A.G., *Numerical simulation of single crystal growth by submerged heater method.* Journal of Crystal Growth, 1990. **104**(2): p. 233-238.
114. Ostrogorsky, A.G., H.J. Sell, S. Scharl, and G. Muller, *Convection and segregation during growth of Ge and InSb crystals by the submerged heater method.* Journal of Crystal Growth, 1993. **128**(1-4): p. 201-206.
115. Monaghan, J.J., *Particle Methods for Hydrodynamics.* Computer Physics Reports, 1985. **3**(2): p. 71-124.
116. Monaghan, J.J., *Smoothed Particle Hydrodynamics.* Annual Review of Astronomy and Astrophysics, 1992. **30**: p. 543-574.
117. Liu, G.R. and M.B. Liu, *Smoothed Particle Hydrodynamics--A Meshfree Particle Method.* World Scientific, 2003.
118. Monaghan, J.J., H.E. Huppert, and M.G. Worster, *Solidification using smoothed particle hydrodynamics.* Journal of Computational Physics, 2005. **206**(2): p. 684-705.
119. Zhang, M.Y., H. Zhang, and L.L. Zheng, *Application of smoothed particle hydrodynamics method to free surface and solidification problems.* Numerical Heat Transfer Part a-Applications, 2007. **52**(4): p. 299-314.
120. Zhang, M.Y., H. Zhang, and L.L. Zheng, *Simulation of Droplet Spreading, Splashing and Solidification Using Smoothed Particle Hydrodynamics Method.* International Journal for Numerical Methods in Fluids, 2007. **(submitted)**.
121. Muradoglu, M. and G. Tryggvason, *A Front-Tracking Method for Computation of Interfacial Flows with Soluble Surfactants.* Journal of Computational Physics. **In Press, Accepted Manuscript**.
122. Unverdi, S.O. and G. Tryggvason, *A front-tracking method for viscous, incompressible, multi-fluid flows.* Journal of Computational Physics, 1992. **99**(1): p. 180.
123. Butty, V., D. Poulikakos, and J. Giannakouros, *Three-dimensional presolidification heat transfer and fluid dynamics in molten microdroplet deposition.* International Journal of Heat and Fluid Flow, 2002. **23**(3): p. 232-241.
124. Zhao, Z., D. Poulikakos, and J. Fukai, *Heat transfer and fluid dynamics during the collision of a liquid droplet on a substrate--I. Modeling.* International Journal of Heat and Mass Transfer, 1996. **39**(13): p. 2771-2789.
125. Ghafouri-Azar, R., S. Shakeri, S. Chandra, and J. Mostaghimi, *Interactions between molten metal droplets impinging on a solid surface.* International Journal of Heat and Mass Transfer, 2003. **46**(8): p. 1395-1407.
126. Pasandideh-Fard, M., S. Chandra, and J. Mostaghimi, *A three-dimensional model of droplet impact and solidification.* International Journal of Heat and Mass Transfer, 2002. **45**(11): p. 2229-2242.
127. Raessi, M. and J. Mostaghimi, *Three-dimensional modeling of density variation due to phase change in complex free surface flows.* Numerical Heat Transfer Part B-Fundamentals, 2005. **47**(6): p. 507-531.

128. Zhang, H., *Theoretical analysis of spreading and solidification of molten droplet during thermal spray deposition.* International Journal of Heat and Mass Transfer, 1999. **42**(14): p. 2499-2508.
129. Zhang, H., L.L. Zheng, Y. Prasad, and T.Y. Hou, *A curvilinear level set formulation for highly deformable free surface problems with application to solidification.* Numerical Heat Transfer Part B-Fundamentals, 1998. **34**(1): p. 1-20.
130. Enright, D., F. Losasso, and R. Fedkiw, *A fast and accurate semi-Lagrangian particle level set method.* Computers & Structures, 2005. **83**(6-7): p. 479-490.
131. Hieber, S.E. and P. Koumoutsakos, *A Lagrangian particle level set method.* Journal of Computational Physics, 2005. **210**(1): p. 342-367.
132. Liu, J., S. Koshizuka, and Y. Oka, *A hybrid particle-mesh method for viscous, incompressible, multiphase flows.* Journal of Computational Physics, 2005. **202**(1): p. 65-93.
133. Zheng, L.L. and H. Zhang, *An adaptive level set method for moving-boundary problems: Application to droplet spreading and solidification.* Numerical Heat Transfer Part B-Fundamentals, 2000. **37**(4): p. 437-454.
134. Gaudlitz, D. and N.A. Adams, *On improving mass-conservation properties of the hybrid particle-level-set method.* Computers & Fluids. **In Press, Accepted Manuscript**.
135. Shao, S. and E.Y.M. Lo, *Incompressible SPH method for simulating Newtonian and non-Newtonian flows with a free surface.* Advances in Water Resources, 2003. **26**(7): p. 787-800.
136. Lattanzio, J.C., J.J. Monaghan, H. Pongracic, and M.P. Schwarz, *Interstellar Cloud Collisions.* Monthly Notices of the Royal Astronomical Society, 1985. **215**(1): p. 125-147.
137. Johnson, G.R., R.A. Stryk, and S.R. Beissel, *SPH for high velocity impact computations.* Computer Methods in Applied Mechanics and Engineering, 1996. **139**(1-4): p. 347-373.
138. Muller, M., D. Charypar, and M. Gross, *Particle-Based Fluid Simulation for Interactive Applications.* Eurographics/SIGGRAPH Symposium on Computer Animation, 2003: p. 154-159.
139. Cummins, S.J. and M. Rudman, *An SPH Projection Method.* Journal of Computational Physics, 1999. **152**(2): p. 584-607.
140. Morris, J.P., *Simulating surface tension with smoothed particle hydrodynamics.* International Journal for Numerical Methods in Fluids, 2000. **33**(3): p. 333-353.
141. Nugent, S. and H.A. Posch, *Liquid drops and surface tension with smoothed particle applied mechanics.* Physical Review E, 2000. **62**(4): p. 4968-4975.
142. Tartakovsky, A.M. and P. Meakin, *Simulation of free-surface flow and injection of fluids into fracture apertures using smoothed particle hydrodynamics.* Vadose Zone Journal, 2005. **4**(3): p. 848-855.
143. Melean, Y., L.D. Sigalotti, and A. Hasmy, *On the SPH tensile instability in forming viscous liquid drops.* Computer Physics Communications, 2004.

157(3): p. 191-200.
144. Melean, Y. and L.D. Sigalotti, *Coalescence of colliding van der Waals liquid drops.* International Journal of Heat and Mass Transfer, 2005. **48**(19-20): p. 4041-4061.
145. Fulk, D.A., *A numerical analysis of smoothed particle hydrodynamics.* Air Force Institute of Technology, 1994.
146. Brackbill, J.U., D.B. Kothe, and C. Zemach, *A continuum method for modeling surface tension.* Journal of Computational Physics, 1992. **100**(2): p. 335-354.
147. Crespo, A.J.C., M. Gomez-Gesteira, and R.A. Dalrymple, *Boundary conditions generated by dynamic particles in SPH methods.* Cmc-Computers Materials & Continua, 2007. **5**(3): p. 173-184.
148. Fauchais, P., A. Vardelle, and B. Dussoubs, *Quo vadis thermal spraying?* Journal of Thermal Spray Technology, 2001. **10**(1): p. 44-66.
149. Adams, B., M. Pauly, R. Keiser, and L.J. Guibas, *Adaptively sampled particle fluids*. Acm Transactions on Graphics, 2007. **26**(3).